

Preface

This dissertation is submitted for the degree of Doctor of Philosophy at Pohang University of Science and Technology. The research described herein was conducted under the supervision of Professor H. K. D. H. Bhadeshia, Professor of Computational Metallurgy in the Graduated Institute of Ferrous Technology and Professor of Physical Metallurgy, University of Cambridge, between March 2008 and December 2011.

This work is to the best of my knowledge original, except where acknowledgements and references are made to previous work. Neither this, nor any substantially similar dissertation has been or is being submitted for any other degree, diploma or other qualification at any other university. This dissertation does not exceed 60,000 words in length.

Part of this work has been submitted to appear in the following publications:

Pak, Junhak and Bhadeshia, H. K. D. H. (2008). Coalesced bainite by isothermal transformation of reheated weld metal. *Science and Technology of Welding and Joining*, 13:593-597

Pak, Junhak, Suh, Dong-Woo and Bhadeshia, H. K. D. H. (2011). Bainite:

Fragmentation of Crystallographically Homogeneous Domains, Accepted
by International Journal of MATERIAL RESEARCH

Pak, Junhak and H. K. D. H. (2011). Mechanism of Misorientation De-
velopment within Coalesced Martensite, Submitted

Pak, Junhak, Suh, Dong-Woo and Bhadeshia, H. K. D. H. (2011). Dis-
placive Phase Transformation and Surface Effects associated with Confo-
cal Laser Scanning Microscopy, Submitted

2011 December, Pak, Jun Hak

DFT Pak, Jun Hak
20080959 Coalesced structure in bainite and martensite
for low-carbon steels, Department of Ferrous Technology
(Computational Metallurgy), 2011, 200p
Advisor: Bhadeshia, H. K. D. H. and Suh, Dong-Woo
Text in English

Abstract

This work aims to illuminate the formation principle of coalesced structure in bainite and martensite of low-carbon steels. It was also tried to suggest a solution to avoid the phenomenon efficiently. There were four kinds of specific work included in the thesis.

Firstly, coalescence in martensitic structure for investigated four alloys was identified by its bimodal distribution of grain size, which is never explained by simple geometrical sectioning effect. Considering martensite transformation proceeds as temperature decreases, the related free energy change between austenite and ferrite increases, which led to the coalescence in martensitic structure due to the resultant large driving force. Coalescence in bainite occurred at low-transformation temperatures, where carbon partitions laggingly and consequently the formation of austenite film becomes retarded. These enhance the adjacent martensitic ferrites to meet. The critical driving force for coalescence was estimated for a spe-

cific alloy by tracing the transformation temperature where no coalescence occurred.

Secondly, misorientation within coalesced martensite was examined using transmission electron microscopy. Considering that austenite accommodates the associated shape deformation plastically, the bending of corresponding slip planes relates to the rotation of austenite crystal. This affected the orientation of martensitic ferrites which formed successively. Two active slip systems were specified using well established Taylor theory combined with literature data on the growth of bainitic ferrite.

Thirdly, effect of external force on coalescence was studied using confocal laser scanning microscopy and thermo-mechanical simulation. Martensite transformation was promoted near to free surface, which is consistent with theoretical calculation to predict large strain energy relaxation there. Interestingly, coalesced martensite tended to form near to free surface as a same manner. Direct tensile stress during isothermal bainite transformation induced the coalescence in bainitic ferrites, however, it occurred selectively in terms of crystal orientation of bainitic ferrites.

Finally, it was attempted to block the coalescence by fragmenting the crystallographically homogeneous domains. Intercritical annealing after martensite transformation was designed to construct substitutional elements-enriched area using a program *DICTRA* version 25. Energy dispersive spectrometry showed that nickel and manganese-enriched areas were survived from full austenitisation and it was confirmed that the intended

fragmentation was successfully conducted.

Contents

Preface	i
Abstract	iii
Contents	vi
Nomenclature	x
1 Basics of martensite and bainite	1
1.1 Bainitic and martensitic transformation	2
1.1.1 Shape deformation	4
1.1.2 Crystallography	6
1.1.3 Diffusionless growth	11
1.1.4 Interface	13
1.2 The bainite transformation	15
1.2.1 Diffusional nucleation	16
1.2.2 Fully supersaturated growth	18

1.2.3	Plastic relaxation	21
1.2.4	Controversy	24
1.3	Coalesced bainite	26
1.3.1	Early observations	26
1.3.2	Microstructure of coalesced bainite	32
1.3.3	Formation condition	32
2	Identification of coalesced structure	36
2.1	Introduction	36
2.2	Experimental method	37
2.3	Results	39
2.3.1	Dilatometry	39
2.3.2	Thermodynamics	42
2.3.3	Microscopy	43
2.3.4	TEM on bainite of Alloy A and B	52
2.4	Discussion	55
2.4.1	Coalescence in martensite	55
2.4.2	Coalescence in bainite	60
2.4.3	Coalescence of bainite in various temperatures	64
2.5	Conclusions	69
3	Misorientation within coalesced structure	70
3.1	Introduction	70
3.2	Experimental method	71

3.3	Results and discussion	72
3.3.1	Dilatometry	72
3.3.2	Microscopy	76
3.3.3	TEM microscopy and diffraction	76
3.4	Mechanism for misorientation	81
3.5	Conclusions	87
4	Effect of external force on coalescence	89
4.1	Introduction	89
4.2	Experimental method	90
4.3	Results	92
4.3.1	Martensite near to free surface	92
4.3.2	Bainite formed under the effect of uniaxial tension	93
4.4	Discussion	101
4.4.1	Effect of free surface	101
4.4.2	Effects of stress	105
4.5	Conclusions	110
5	Prevention of coalescence	111
5.1	Introduction	111
5.2	Experimental method	112
5.3	Results and discussion	113
5.3.1	Method	113
5.3.2	Design of Heat Treatment	114

5.3.3	Dilatometry	119
5.3.4	Characterisation	125
5.3.5	Crystallography	131
5.3.6	Effect on coalescence	131
5.4	Conclusions	133
6	Summary	134
A	Estimation of the bainite–start temperature	136
B	Identification of activated slip systems	140
C	Calculation of rotation matrices	149
C.1	$R_b R_a$ at $\phi = 0.25$	151
C.2	$\frac{1}{2} R_b \frac{1}{2} R_a \frac{1}{2} R_b \frac{1}{2} R_a$ at $\phi = 0.25$	153
	Bibliography	155
	Acknowledgement	167
	Curriculum Vitae	170

Nomenclature

α	Ferrite
α'	Martensitic ferrite
α_b^h	Bainite formed from austenite with heterogeneous composition
α_b	Bainitic ferrite
ΔG	General term representing driving force
$\Delta G^{\gamma \rightarrow \alpha}$	Free energy change for transformation without composition change
ΔG_{MECH}	Mechanical driving force
ΔG_m	Maximum molar Gibbs free energy change accompanying nucleation
δ	Uniaxial dilatation normal to the habit plane
γ	Austenite
μ	Shear modulus

ν	Poisson's ratio
\bar{D}	Weight average diffusivity of carbon in austenite
ρ_D	Dislocation density
σ	Stress component
τ_c	Critical resolved shear stress
B_C	Coalesced bainite
M_S	Martensite start temperature
ε_{ij}	Strain component
ε_{ij}^c	Strain component based on crystal axis
a_γ	Lattice parameter of austenite
a_{ij}	Direction cosine value
$Ae3''$	As $Ae3'$, but with accounting strain energy of product phase
$Ae3'$	Temperature separating the $\alpha+\gamma/\gamma$ para-equilibrium phase field for specific alloy
E	Young's modulus
G_N	Function specifying the free energy change needed in order to obtain a detectable rate of nucleation for Widmanstätten and bainite

G_S	Strain energy per mole
T	Temperature
T_0	Temperature at which γ and α of the same composition have the same free energy
T'_0	As T_0 , but accounting for the stored energy of ferrite
t_d	Time required to decarburise a plate of bainite
T_h	The temperature below which the nucleation of displacive transformations first becomes possible at a detectable rate
V_m	Molar volume
w	Thickness of a bainite sub-unit
$x^{\alpha\gamma}$	Mole fraction of carbon in ferrite which is in equilibrium or paraequilibrium with austenite
$x^{\gamma\alpha}$	Mole fraction of carbon in austenite which is in equilibrium or paraequilibrium with ferrite
x_α	Carbon concentration in α at interface
x_γ	Carbon concentration in austenite
x_m^α	Maximum carbon supersaturation permitted in ferrite, on thermodynamic grounds

$x_{T'_0}$	Carbon concentration given by the T'_0 curve
s	Shear component of the IPS shape deformation
B_S	Bainite start temperature
BCC	Body-centered cubic
BCT	Body-centered tetragonal
CLSM	Confocal laser scanning microscopy
EBSD	Electron backscattered diffraction
FCC	Face-centered cubic
FEGSEM	Field emission gun scanning electron microscopy
FIB	Focused-ion beam
IPS	Invariant-Plane Strain shape change
IQ	Image Quality mapping
PTMC	Phenomenological Theory of Martensite Crystallography
SDLE	Solute-Drag like Effect
TEM	Transmission electron microscopy
TTT	Time-temperature-transformation

Chapter 1

Basics of martensite and bainite

In the modern research on steels, bainitic and martensitic transformations have attracted not only industrial but also academic interest due to the properties of the transformation products and because of the interesting accompanying phenomena. In particular, the mechanism of the bainite transformation is still controversial, as will be discussed later. On the other hand, the desire to produce steel with advanced properties has led to the various commercial alloys based on those phases (Bhadeshia, 2001). In addition, independent work by Tomita and Okabayashi (1983); Yin et al. (1990); Saxena et al. (1993); Li and Wang (1993) reported that the mechanical properties of bainite-martensite mixed microstructure can

be superior to that of the individual phase (Barbacki, 1995). In this context, the huge reduction of impact toughness in weld metal reported by Keehan et al. (2006b,d) must be significant since the metal was designed originally for a mixed structure with two phases. They related the deterioration in toughness with the occurrence of the so-called coalesced bainite as the coarse phase generated when fine plates combine. It will be shown later that the coalescence might be a more general phenomenon associated with both the martensite and bainite transformation. This work aimed to examine the coalescence in various steels and to discover the controlling parameters. A good process was to propose effective methods to prevent coalescence and hence to retain a microstructure containing of fine plates.

1.1 Bainitic and martensitic transformation

Basically both bainite and martensite are the products of non-equilibrium transformation. Therefore they are not represented on equilibrium diagrams. In other words, these transformations fail to achieve the minimum of Gibbs-free energy and given sufficient thermal activation, should tend towards equilibrium (Bhadeshia, 2001). Bainite & martensite can of course be represented on time-temperature-transformation diagrams (Fig. 1.1), as ‘meta-stable’ phases with clearly defined domains.

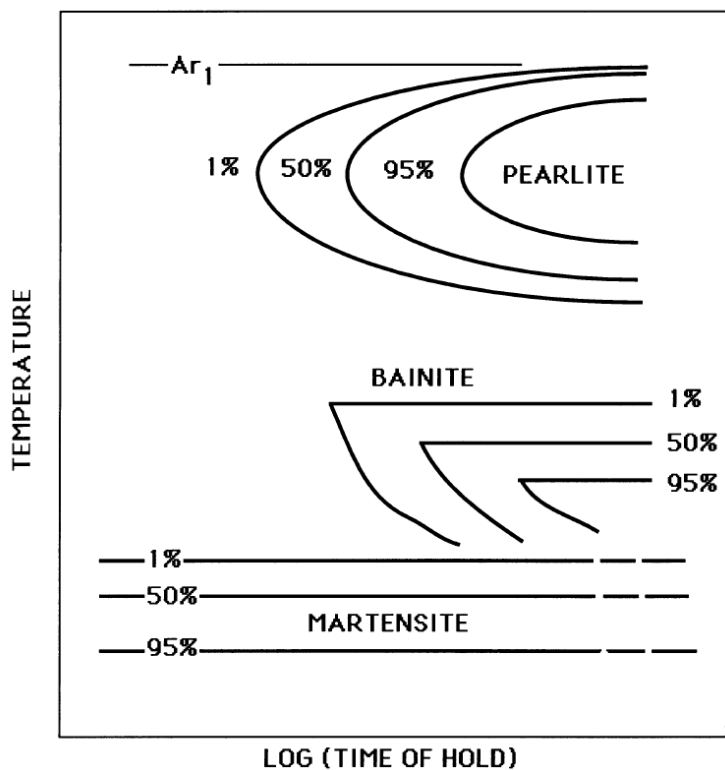


Figure 1.1: The schematic time-temperature-transformation (TTT) diagram showing the distinctive transformation region of the bainite and martensite transformations. Reprinted from (Bhadeshia, 2001) with permission from Maney Publishing.

1.1.1 Shape deformation

The formation of bainite or martensite causes the displacement of a scratch which existed while the sample was in its austenitic state (Fig. 1.2). Notice that the continuity of scratch is maintained across the boundary between the parent and product phases. This is so at least at the indicated resolution and suggests that the displacement is induced by a homogeneous deformation, which fulfills some degree of coherency across the interface. According to Christian (1990), the shape change can be described as an invariant-plane strain (IPS) with a large shear component (Bowles and Mackenzie, 1954a; Mackenzie and Bowles, 1954; Bowles and Mackenzie, 1954b). As expected from the name, the IPS leaves a plane unrotated and undistorted, referred to as an invariant-plane. Fig. 1.3 illustrates how the IPS with the given invariant-plane normal (\mathbf{p}) and the displacement (\mathbf{d}) causes the surface relief effect. The X-Y line corresponds to the original scratch prior to transformation and X-Z line following transformation (Fig. 1.2). The deformation can be divided into shear strain (s) of 0.22-0.24 and dilatation strain (δ) of 0.03 (Sandvik, 1982; Swallow and Bhadeshia, 1996; Dunne and Wayman, 1971). It must be accommodated by the surrounding matrix due to coherency across the interface (Christian, 1990). If this is elastic, then Christian (1958) proved that the

resulting molar strain energy G_S is given by:

$$G_S = \frac{c}{a} \frac{\pi(2-\nu)}{8(1-\nu)} \mu s^2 + \frac{\pi}{4} \mu \delta^2 \simeq \frac{c}{a} \mu (s^2 + \delta^2) \quad (1.1)$$

where c is the thickness of the product phase, here representing martensite or bainite plate, a is the plate length, ν is the Poisson's ratio, μ is the shear modulus of the austenite and V_m is the molar volume of the austenite. The consequent strain energy amounts to 600 J mol^{-1} and 400 J mol^{-1} for martensite and bainite, respectively (Bhadeshia, 2001). The IPS is quite different from the isotropic volume change accompanying diffusional transformation.

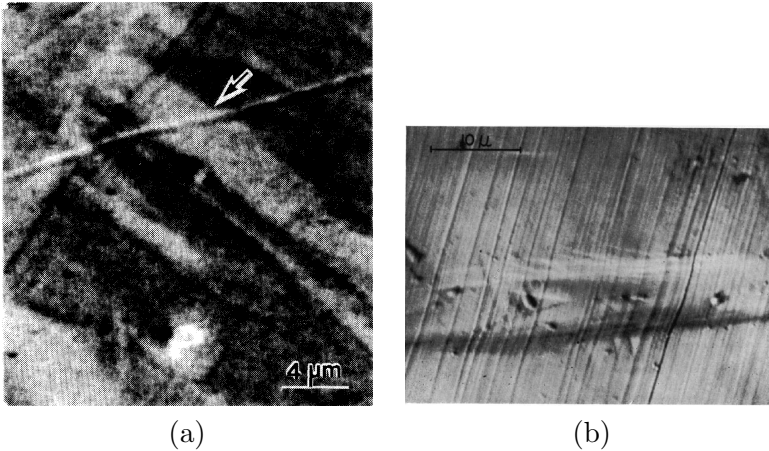


Figure 1.2: Scratch displacement resulting from the formation. (a) Martensite. Reprinted figure with permission from (Yang et al., 1995). Copyright (1995) by the American Physical Society. (b) Bainite. Reprinted from (Srinivasan and Wayman, 1968) with permission from Elsevier.

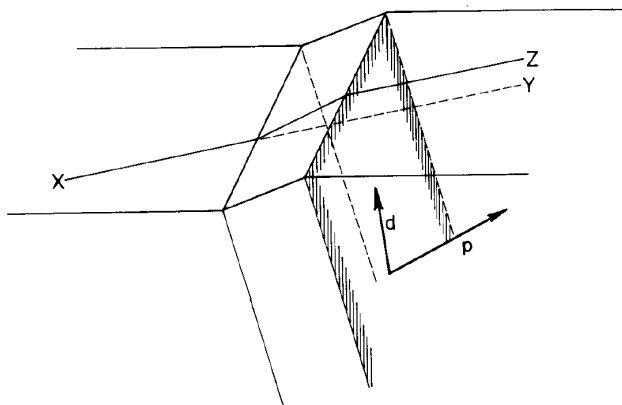


Figure 1.3: The schematic representation of an invariant-plane strain (IPS) and the surface relief. Reprinted from (Wayman, 1975) with permission from Elsevier.

1.1.2 Crystallography

A specific orientation relationship between face-centered cubic (FCC) austenite and body-centered cubic (BCC) ferrite is likely when the latter is transformed by a homogeneous deformation. The Bain strain (\mathbf{B}) (Fig. 1.4), which permits the lattice change in a displacive transformation, is a pure deformation comprising two simple extensions (along b_1 and b_2 axes) and an extraction (along b_3 axis) of principal axes. When combined with a rigid body rotation (\mathbf{R}), it is possible to explain experimentally observed austenite (γ) /martensite (α') or γ /bainite (α_b) orientation relationships (Bhadeshia, 2001).

The combination of the Bain strain and rigid body rotation can only

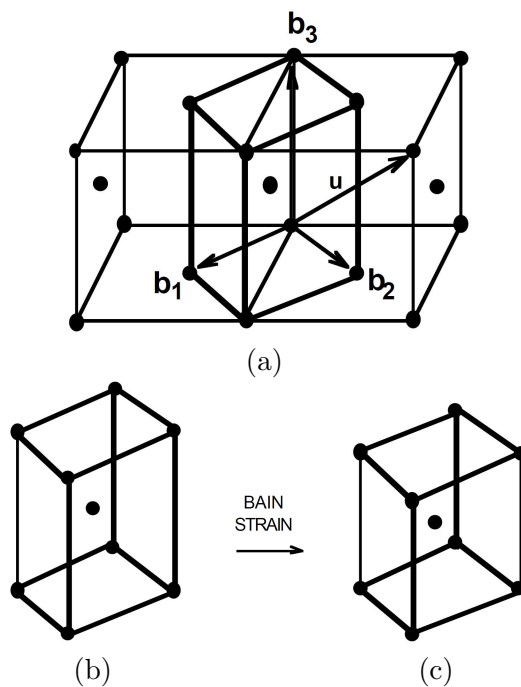


Figure 1.4: Schematic diagram describing Bain strain; (a) relationship between FCC and body-centered tetragonal (BCT) cells of austenite; (b) BCT cell of austenite; (c) BCC ferrite lattice produced from BCT austenite lattice by Bain strain. Reprinted from (Bhadeshia, 1987) with permission from Maney Publishing.

produce an invariant–line strain (Fig. 1.5), not an invariant–plane strain, which represents the macroscopically observed shape deformation (Bowles and Barrett, 1952).

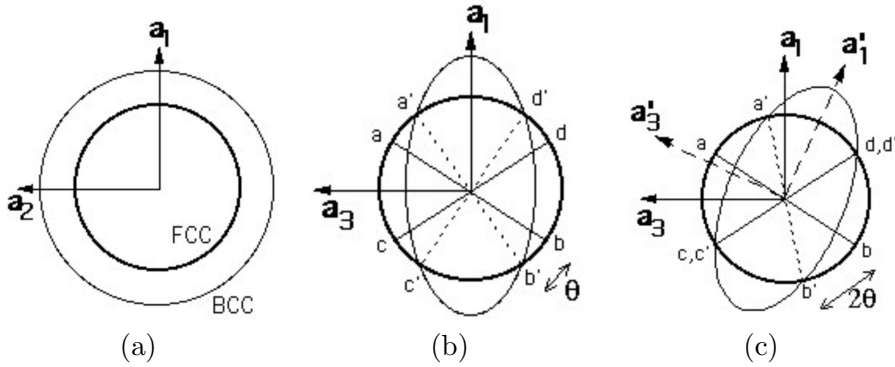


Figure 1.5: Schematic diagram illustrating an invariant–line strain due to Bain strain and rigid body rotation, where original austenite lattice was described by a sphere; (a) and (b) explain the effect of the Bain strain on austenite, which deforms the diameter ab and cd into $a'b'$ and $c'd'$; (c) the rigid body rotation caused $c'd'$ corresponding to cd , which becomes invariant–line. Reprinted from (Bhadeshia, 1987) with permission from Maney Publishing.

The complete theory which reconciles this difference appeared in work by Bowles and Mackenzie (1954a); Mackenzie and Bowles (1954); Bowles and Mackenzie (1954b). They explained that the total deformation occurs by a combination of homogeneous and inhomogeneous strains and expressed the concepts mathematically using matrix methods; the former was represented by combining two successive invariant–plane strains (**QP**) equals the combination of the Bain strain with the rotation (**RB**), here

bold capital characters represent matrix forms of a corresponding operation:

$$\mathbf{QP} = \mathbf{RB}. \quad (1.2)$$

The heterogeneous deformation (\mathbf{Q}^{-1}), which cancels the shape change by \mathbf{Q} , is realized by slip or twinning and is known as the lattice-invariant deformation since it does not alter the crystal structure. The whole procedure is explained in Fig. 1.6, called as ‘Phenomenological Theory of Martensite Crystallography’ (PTMC) (Bhadeshia, 1987).

In terms of energetics, the lattice-invariant deformation reduces the strain energy to the value described in Eq. 1.1. Christian (1990) insisted that some plastic flow may occur in the matrix due to large shape deformation, and consequently may modify the detailed crystallography.

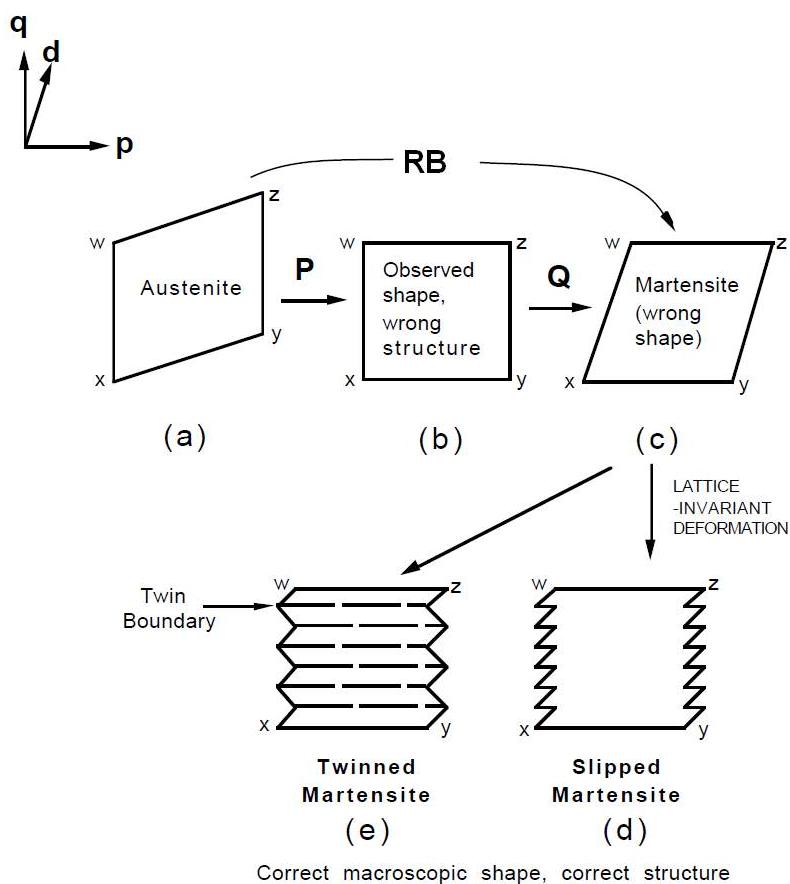


Figure 1.6: Schematic diagram illustrating PTMC; (a) original austenite lattice; (b), (c) the effects of invariant-plane strains of \mathbf{P} and \mathbf{Q} , where the invariant-plane normals are \mathbf{p} and \mathbf{q} direction, respectively; (e), (f) lattice-invariant deformation occurred on the plane with the plane normal of \mathbf{q} . Reprinted from (Bhadeshia, 1987) with permission from Maney Publishing.

1.1.3 Diffusionless growth

There is considerable evidence for the diffusionless growth of bainite of martensite. As shown in Fig. 1.1, displacive transformation takes place at low temperatures. For highly alloyed steels, martensitic transformation can occur even at sub-zero temperatures (Wakasa and Wayman, 1979; Kaufman et al., 1960), where diffusion is implausible (Hirano et al., 1961). Reported growth rates of martensite can be as high as 1 km s^{-1} , i.e. about one-third of the velocity of sound in iron (Bunshah and Mehl, 1953). Ali and Bhadeshia (1989) showed that the measured lengthening rate of bainite ($75 \mu\text{m s}^{-1}$) exceeds that calculated ($0.083 \mu\text{m s}^{-1}$) based on the paraequilibrium, where the maximum diffusion-controlled rate can be expected by allowing only interstitial elements to diffuse. Experiments where chemical and spatial analysis is available on an atomic scale prove that there is no composition change with respect to substitutional solutes during displacive transformation. In the case of bainite, it is possible to show that carbon too is not partitioned during growth (Bhadeshia and Waugh, 1982; Stark et al., 1990; Josefsson and Andr en, 1991). Therefore, bainite and martensite are not governed by atomic diffusion. Growth is diffusionless, driven by the difference in free energy between austenite (γ) and ferrite (α) of identical composition (Fig. 1.7). Consequently, any reaction above the T_0 temperature where the both phases with same composition have identical free energy is thermodynamically impossible. If strain energy

due to the shape deformation is accounted for, a T'_0 temperature must be used instead (Bhadeshia and Edmonds, 1980).

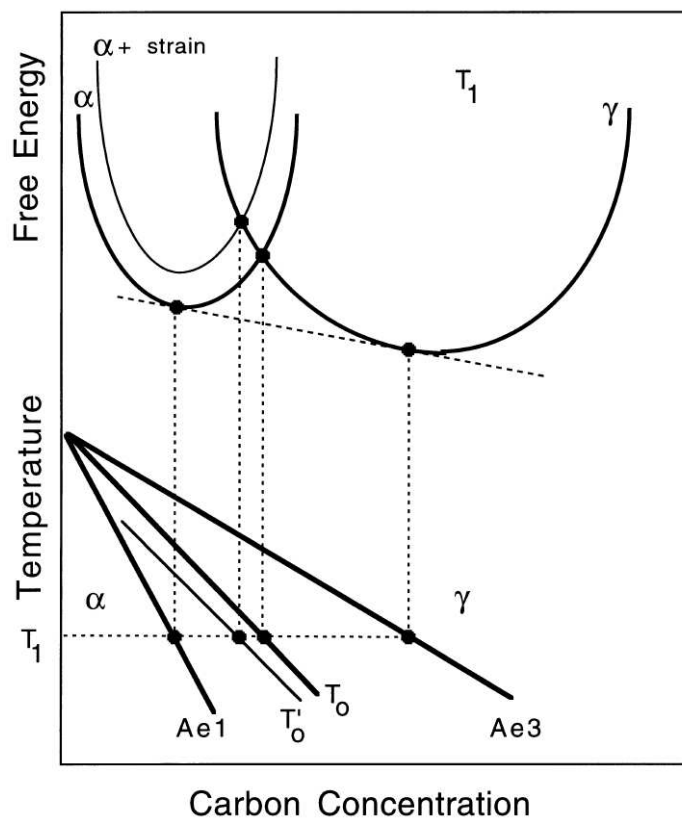


Figure 1.7: The schematic illustration showing the driving force in diffusionless transformation and the concept of T_0 temperature. Reprinted from (Bhadeshia, 2001) with permission from Maney Publishing.

1.1.4 Interface

The interface according to Olson and Cohen (1979) consists of arrays of two kinds of dislocations with different properties, the coherency and anticoherency dislocations (Fig. 1.8). The former never destroy the continuity of corresponding planes and vectors across the interface, so that their motion proceeds in a conservative way, which keeps the number of atoms in the transformed region. The Burgers vectors of coherency dislocations are partial so that their motion results in phase transformation. The coherency dislocations have Burgers vectors with both glide and climb components, which is why the vector is inclined to the corresponding plane (Fig. 1.8a). As explained before, the total homogeneous deformation is performed by the subsequent operation of coherency dislocations on the different planes, which equals to the combination of Bain strain (\mathbf{B}) and rotation (\mathbf{R}) (Fig. 1.8a, b). The coherency dislocations on discrete lattice planes appears as steps of atomic scale (Olson, 1981). On the other hand, a periodic array of anticoherency dislocations reduce the strain energy by cancelling a portion of the stress field due to the coherency dislocations and consequently offsets some parts of homogeneous deformation (Fig. 1.8c). They implement the lattice-invariant deformation and their line vectors are parallel to the invariant-lines. Notice the anticoherency dislocations normally have lattice Burgers vectors and behave as conventional lattice dislocations except for the twinning dislocations. Therefore, the

conservative motion is guaranteed only in glide.

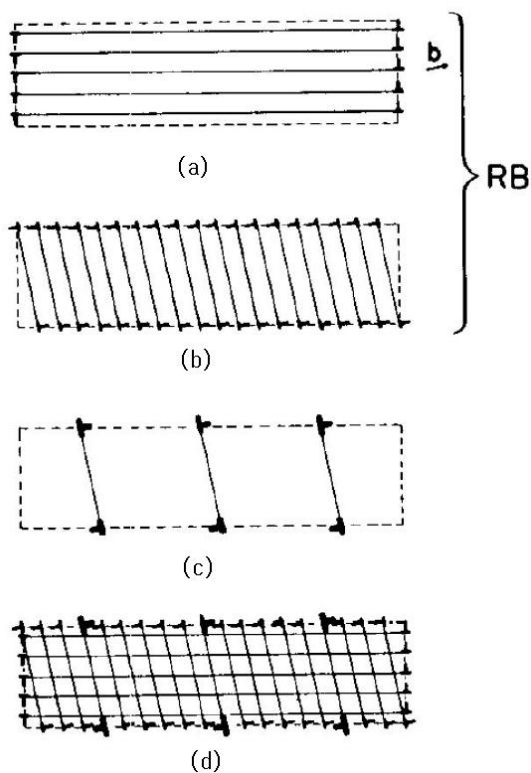


Figure 1.8: Schematic diagrams for the interface consisting of discrete dislocations. (a),(b) Coherency dislocations producing homogeneous deformation. (c) Anticoherency dislocations producing lattice-invariant deformation. (d) Total interfacial structure (Olson and Cohen, 1981).

1.2 The bainite transformation

According to Christian (1990), a ‘displacive transformation’ describes that produced by a coherent interface albeit allowing local inhomogeneities. It usually encompasses the term ‘martensitic transformation’, where the diffusion of atoms does not occur. In this context, both martensite and bainite are products of displacive transformation. Nevertheless, bainite is definitely distinguished from martensite; the two structures can appear quite different during optical microscopy (Fig. 1.9) and in their kinetic behavior (Fig. 1.1). Bainite occurs at higher temperatures than martensite. Interstitial atoms may then be mobile during transformation. The strength of the austenite decreases at high temperatures and this can lead to plastic relaxation during the bainite transformation.

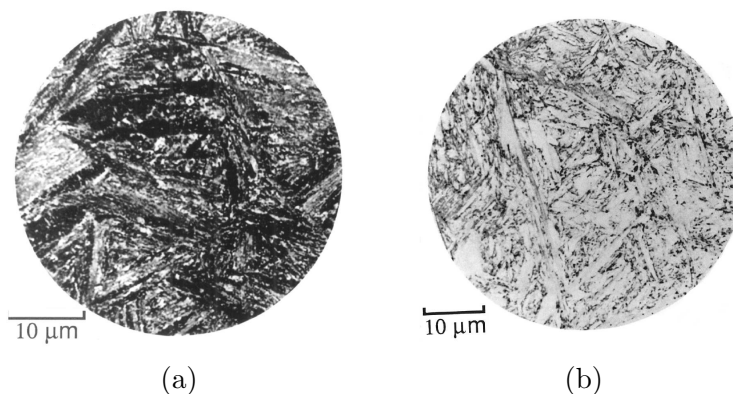


Figure 1.9: The different morphologies for (a) bainite and (b) martensite. Bainite etches much darker than martensite due to a larger number of interfaces due to the presence of cementite (Bain and Paxton, 1966).

1.2.1 Diffusional nucleation

The degree of bainite transformation increases with time at a fixed temperature (Fig. 1.1). In general, the isothermal characteristics are understood as the result of a thermally assisted nucleation processes *i.e.* atomic diffusion (Christian, 1965). The classical nucleation theory treats the incubation period (Russell, 1969), which also exists in the bainite transformation. The necessity of atomic diffusion in the nucleation stage of bainite transformation is demonstrated paradoxically in Fig. 1.10 where the exclusion of diffusion lead to an impossible positive change of free energy (Bhadeshia, 1981).

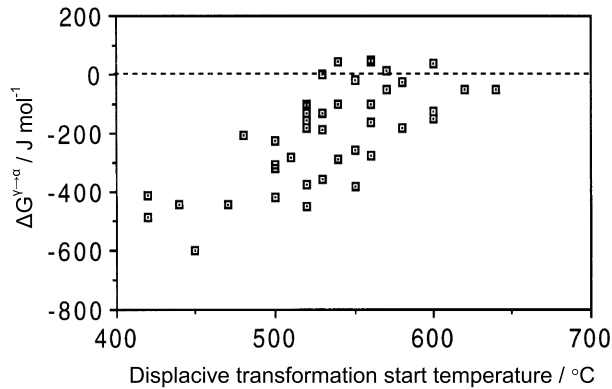


Figure 1.10: The free energy change at the displacive transformation start temperatures. Individual points refer different steels. Reprinted from (Bhadeshia, 2001) with permission from Maney Publishing.

The driving force for nucleation is the free energy corresponding to the gap between the tangent line AB and the curve for the product phase (α) (Fig. 1.11). It depends therefore on the composition of the nucleus, for example, the nucleus with the composition x_α will be formed with the driving force ΔG . The maximum driving force (ΔG_m) is for a nucleus with composition x_m^α .

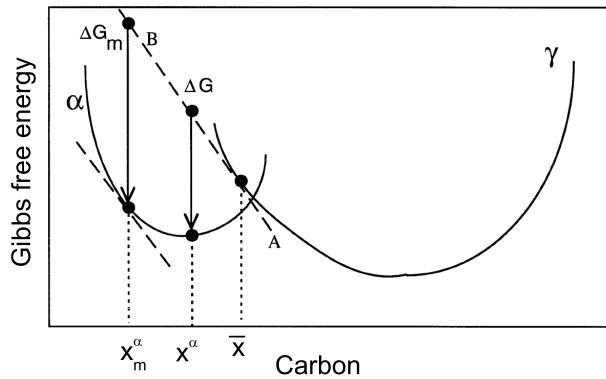


Figure 1.11: The driving force for nucleation. Reprinted from (Bhadeshia, 2001) with permission from Maney Publishing.

Ali and Bhadeshia (1990) collected the highest temperature (T_h) where ferrite can form by displacive transformation for various alloys and calculated the values for ΔG_m at the temperatures. These temperatures correspond to those of the characteristic flat top for Widmanstätten ferrite or bainite transformation domain in Fig. 1.1. They created an empirical

equation which correlates T_h and ΔG_m :

$$G_N = C_1(T - 273.18) - C_2 \text{ J mol}^{-1} \quad (1.3)$$

where the fitting constants are found to be $C_1 = 3.637 \pm 0.2 \text{ J mol}^{-1} \text{ K}^{-1}$ and $C_2 = 2540 \pm 120 \text{ J mol}^{-1} \text{ K}^{-1}$ available for the temperature range 670-920 K. The physical meaning of G_N is the critical driving force for the nucleation and referred to as a *universal nucleation function*. The function can also be applied to the bainite transformation since both transformations are identical in terms of nucleation mechanism (Bhadeshia, 2001). However, the transformation begins when not only the nucleation but also the growth are guaranteed. The free energy change must be sufficient to surmount the strain energy G_S of Eq. 1.1. In the end, the bainite transformation can be expected below T'_0 when the following conditions are satisfied:

$$\Delta G^{\gamma \rightarrow \alpha} < -G_S, \quad \Delta G_m < G_N$$

1.2.2 Fully supersaturated growth

The bainite transformation normally involves the formation of cementite either inside the bainitic ferrite or on the retained austenite (Fig. 1.12); at relatively high temperatures, carbon partitions easily into the surrounding austenite and precipitates there, which forms an upper bainite; at low temperatures, carbon precipitates inside the ferrite, which forms a lower

bainite (Takahashi and Bhadeshia, 1990).

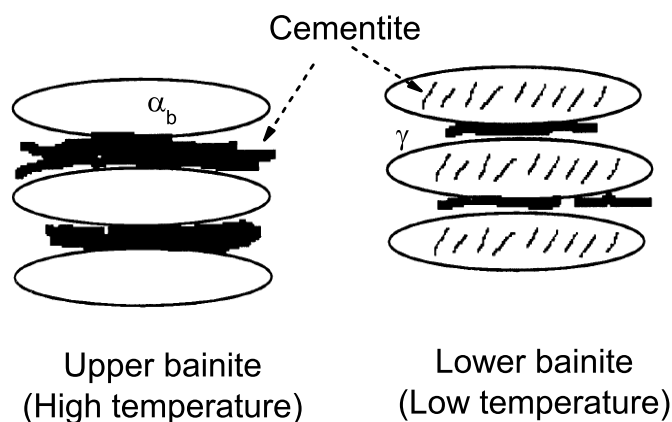


Figure 1.12: Schematic diagrams explaining the formation of cementite in the bainite transformation at relatively high and low temperatures. Reprinted from (Takahashi and Bhadeshia, 1990) with permission from Maney Publishing.

The way to establish the role of carbon during the bainite transformation is to compare the composition of γ (x_γ) at the point where reaction ceases. The reaction in fact stops before equilibrium is reached, leading to the so-called ‘incomplete-reaction phenomenon’ (Stark et al., 1990). There are cases where the x_γ exceeds the value (x_{T_0}) determined by T_0 line (Fig. 1.13) and similar observations were also reported (Self et al., 1981; Chang and Bhadeshia, 1995a). Bhadeshia and Waugh (1982) explained this as following; a small region of austenite surrounded by supersaturated fer-

rites can accumulate excess carbon but never transform into bainite since $x_\gamma > x_{T_0}$. Based on this, Rees and Bhadeshia (1992b) suggested the quantitative model accounting the kinetics of the bainite transformation. Considering that the growth with partially supersaturated ferrite ultimately reaches equilibrium state during transformation, only the growth with fully supersaturated ferrite can be compatible with the results shown in Fig. 1.13 (Bhadeshia and Waugh, 1982).

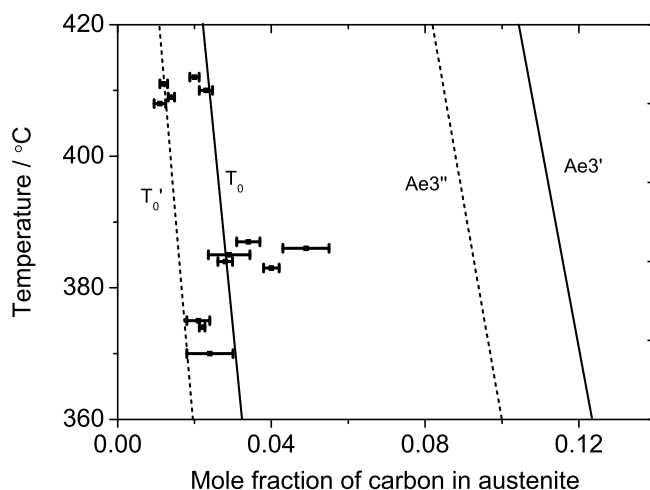


Figure 1.13: The measured carbon content in the austenite and the calculated phase boundaries. $Ae3'$ and $Ae3''$ correspond to the $(\alpha+\gamma)/\gamma$ boundary based on the paraequilibrium and that considering the stored energy, respectively. Notice that the cementite formation was suppressed in this alloy by adding silicon, therefore, this result reflects the pure accumulation of carbon. Reprinted with kind permission from Springer Science+Business Media: (Stark et al., 1990).

1.2.3 Plastic relaxation

If the matrix is not strong enough at the transformation temperature to accommodate the shape deformation elastically, then it relaxes through plastic deformation, which can occur *via* slip, twinning or faulting. Swallow and Bhadeshia (1996) examined the surface relief associated with a sub-unit of bainitic ferrite and the adjacent austenite region (Fig. 1.14). They interpreted the initial steep topographical line as evidence of plastic relaxation. In addition, the topographical line was much more regular in the bainite than the adjacent austenite, which means that the plastic relaxation was confined to the austenite.

The plastic relaxation is more favoured in the bainite transformation where the strength of matrix is relatively low due to a higher transformation temperature compared to that of martensite (Bhadeshia, 2001). It leads to the accumulation of dislocations in front of the advancing interface and finally blocks its further movement. This explains why the growth of a bainite sub-unit stops before the plate meets other physical obstacles such as grain boundaries (Chang and Bhadeshia, 1995b). Transformation then proceeds with the repeated nucleation of sub-units to form a sheaf (Bhadeshia, 2001) (Fig. 1.15).

Dislocations swept by the interface during growth must be inherited by the product since the transformation is conservative (Bhadeshia, 2001). Therefore, Takahashi and Bhadeshia (1990) developed an empirical equa-

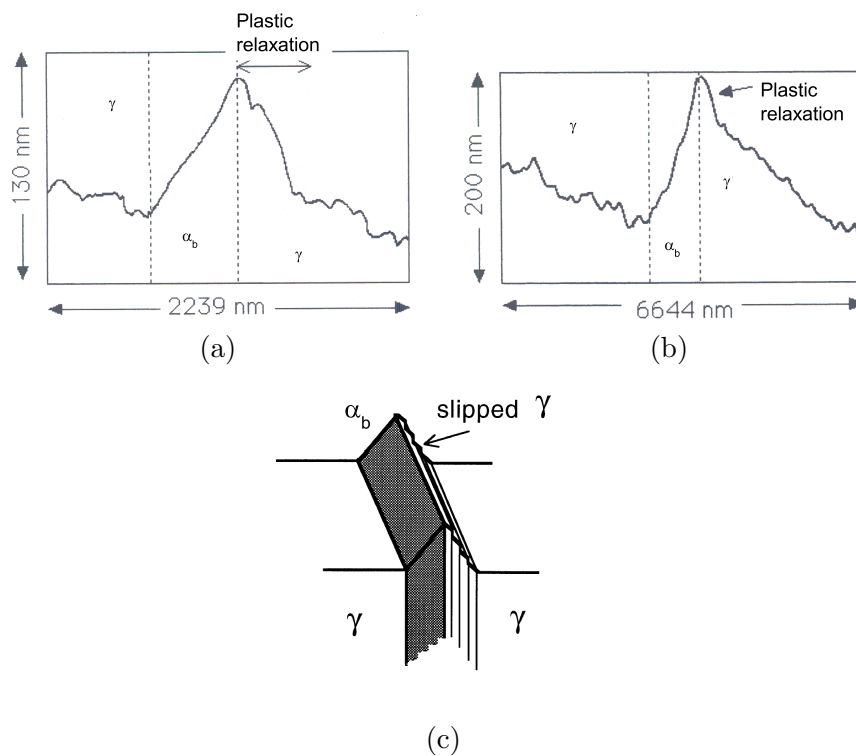


Figure 1.14: (a),(b) An actual topography across the surface relief due to a bainite sub-unit. Reprinted from (Swallow and Bhadeshia, 1996) with permission from Maney Publishing. (c) Illustration of the plastic relaxation in the austenite adjacent to the sub-unit. Reprinted from (Bhadeshia, 2001)with permission from Maney Publishing.

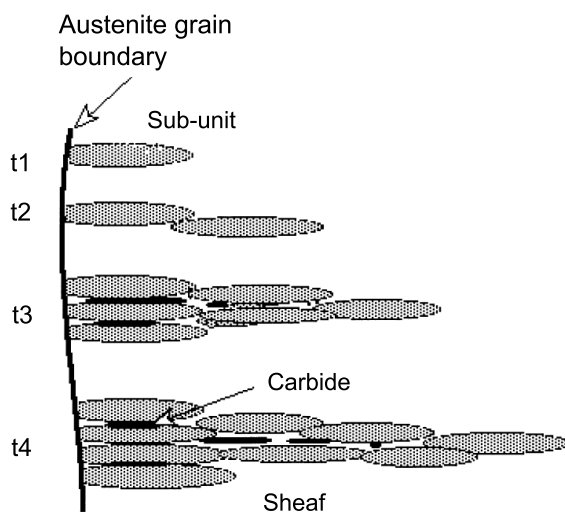


Figure 1.15: The schematic diagrams describing the repetition of nucleation of bainite sub-units. Time sequence is t_1 to t_4 . Reprinted from (Rees and Bhadeshia, 1992a) with permission from Maney Publishing.

tion to predict the total dislocation density resulted from displacive transformation:

$$\log \rho_D = 9.28480 + \frac{6880}{T} - \frac{1780360}{T^2} \quad (1.4)$$

where ρ_D is the dislocation density in m^{-2} and T is the reaction temperature in Kelvin over 570-920 K. The equation predicts greater dislocation density in martensite due to its lower transformation temperature. This might sound unreasonable since martensitic transformation is believed to have less plastic accommodation. Considering that the recovery effects also decrease at lower temperatures (Morito et al., 2003), however, the tendency indicated by Eq. 1.4 could be reasonable.

1.2.4 Controversy

The correct understanding of the transformation mechanism is important from the engineering view, perhaps more so that in the academic field. The mechanism is directly related to the mechanical properties of the product. In this context, Bhadeshia (2004) emphasized that the shape deformation due to bainite effectively refines the grain size, which is the only method to improve both the strength and toughness of a material. Notice that the shape deformation is the main characteristic of the displacive transformation.

However, there is an alternative interpretation in which the bainite forms by a diffusional process (Aaronson and Lee, 1987). In fact, the

arguments surrounding the mechanism of the bainite transformation have continued up to recently with the individual evidences (Ohmori and Maki, 1991; Reynolds Jr. et al., 1991; Yang and Fang, 2005). All of them cannot be discussed here, however, it will be interesting to address the solute-drag like effect (SDLE), which was used to explain the incomplete-reaction and the consequent refinement of the grain in the ‘diffusional’ view. The SDLE occurs as follows; when the substitutional elements are absorbed by the moving interface, it reduces the carbon activity in austenite in contact with the growing interface. Then the resulting growth of the sub-unit as well as the overall transformation rate is retarded (Bradley and Aaronson, 1981), which can lead to the incomplete-reaction and the grain refinement (Reynolds Jr. et al., 1991). The weakness of the model is that the necessary segregation of substitutional solutes is not observed (Bhadeshia and Waugh, 1982; Bach et al., 1980; Stark et al., 1990). In particular, it was pointed that some segregation can happen during the isothermal holding, however, which is a separate reaction toward equilibrium and unrelated to the bainite transformation (Stark et al., 1990; Ohmori and Maki, 1991). In addition, Jung et al. (1998) showed that the plain carbon steels with no solutes to cause the SDLE exhibit the delayed reaction which can be explained by the bay of bainite region in the TTT diagram. This demonstrates again the absence of the SDLE in the bainite transformation.

1.3 Coalesced bainite

Similar to the cases of other microstructures, coalesced bainite became a big concern since it was known to affect the mechanical properties of the material, however, unfortunately with its harmful aspect (Keehan et al., 2006b,d). The formation mechanism has been explained *via* the only qualitative model (Fig. 1.16) (Keehan et al., 2005). The mechanism explains that the coalescence happens during the growth of individual subunits in advance of carbon partitioning or carbide precipitation. This implies that the coalescence also can be the problem in the martensite transformation in which the growth mechanism is identical to that of the bainite sub-unit.

1.3.1 Early observations

It is interesting that Tsuzaki et al. (1994) reported the coalescence between individual sub-units as a natural phenomenon in formation of bainite sheaf. He referred the work of (Oblak and Hehemann, 1967) as evidence, where there was the following statement instead of the direct mention about the coalescence:

Individual laths have nucleated at the side of the others and have propagated well in advance of the main group before their growth has been terminated.

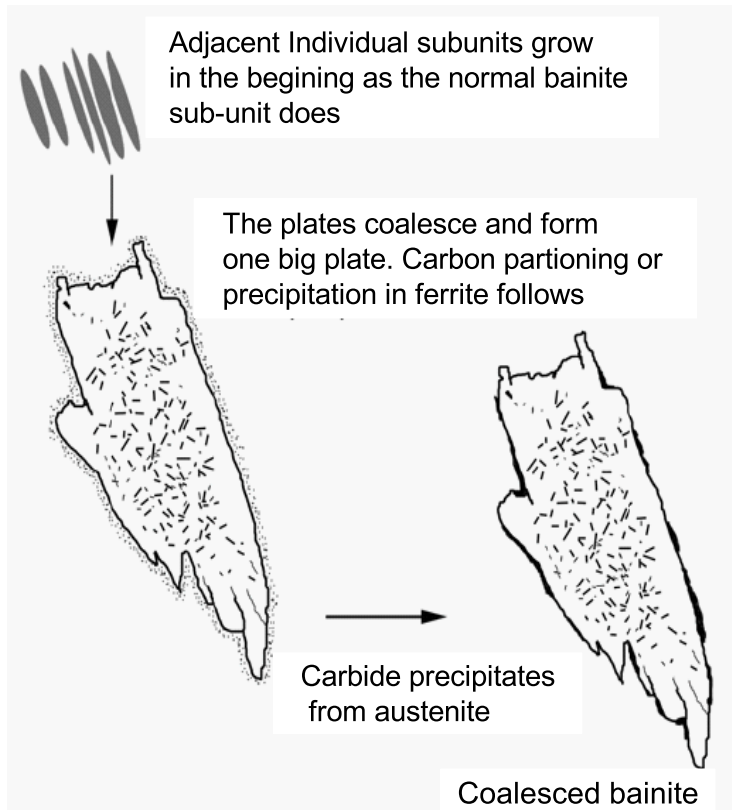
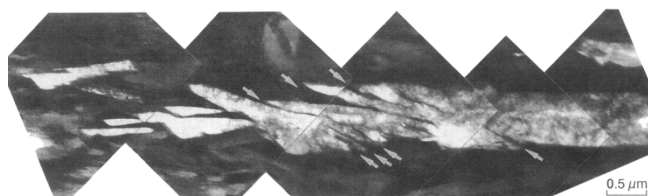
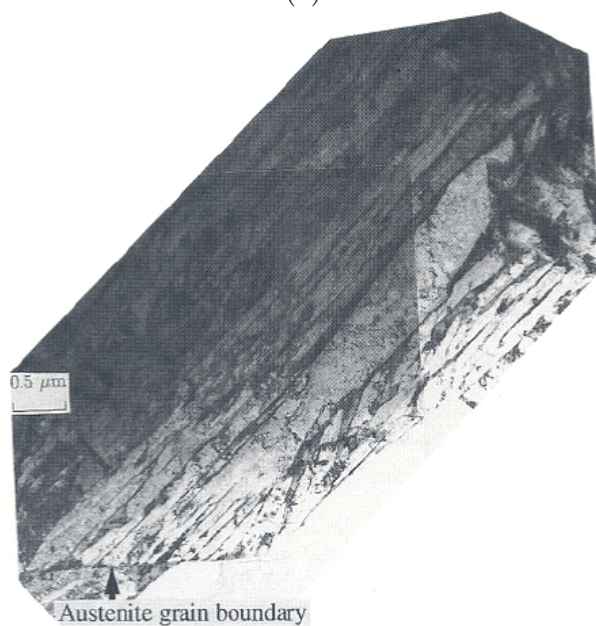


Figure 1.16: The schematic diagrams illustrating the formation mechanism of the coalesced bainite (Keehan et al., 2005).

which might be the description about the possibility of the coalescence. Nevertheless, it should be noticed that the observation of Tsuzaki et al. (1994) through transmission electron microscopy (TEM) is close to that of Chang and Bhadeshia (1996), where the latter is accepted as the stereotype of coalesced bainite (Fig. 1.17). The mention about the coalescence can be found in the works of Jung et al. (1998) and Ohmori and Maki (1991), although, they seemed to envisage a diffusional process for the mechanism. On the contrary, Bhadeshia and Edmonds (1979) and Padmanabhan and Wood (1984) found cases where the bainite formed in apparent allotriomorphic arrays of individual sub-units and called them as ‘grain boundary lower bainite’ (Fig. 1.18). Especially, Bhadeshia and Edmonds (1979) explained that the morphology can be developed at a low transformation temperature due to the lesser degree of carbon partitioning and larger nucleation rate. Chang and Bhadeshia (1996) focused on the bimodal size distribution of the bainitic microstructure where the coalescence mechanism was significantly introduced. Later, Bhadeshia et al. (2006) listed the alloy composition where the coalescence was observed (Table 1.1).

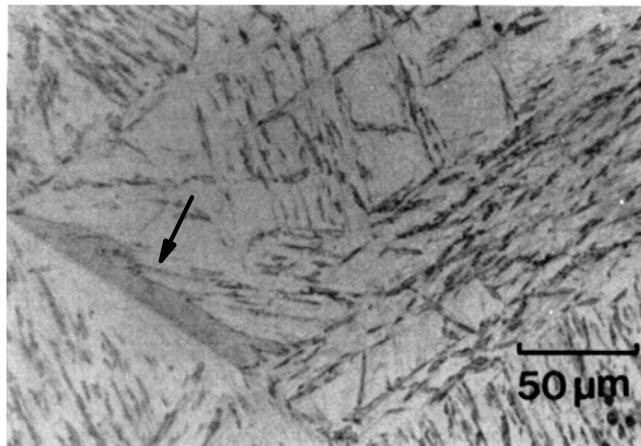


(a)

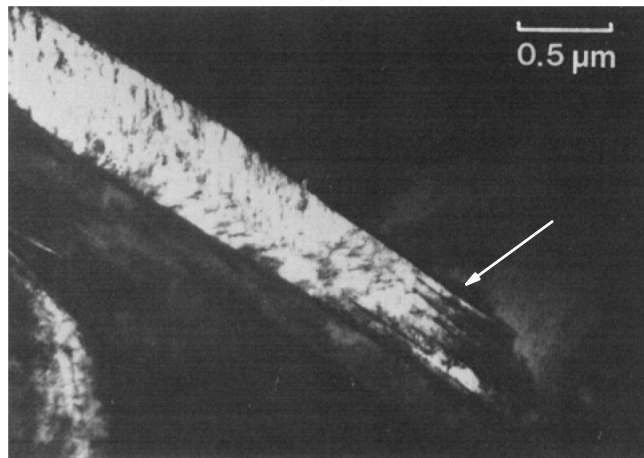


(b)

Figure 1.17: The TEM micrographs showing the coalescence. The arrows in (a) represent the non-coalesced region. (a) Reprinted with kind permission from Springer Science+Business Media: (Tsuzaki et al., 1994) and (b) Reprinted from (Chang and Bhadeshia, 1996) with permission from Maney Publishing.



(a)



(b)

Figure 1.18: The morphology of grain boundary lower bainite; (a) the arrow indicates the corresponding structure in optical micrography; (b) the tip of plate of bainite formed at the different temperature with the same alloy with (a) by TEM. Notice the separation of sub-units at the arrow. Reprinted with kind permission from Springer Science+Business Media: (Bhadeshia and Edmonds, 1979).

Table 1.1: Chemical compositions in % of steels and weld metals in which coalesced bainite has been observed (Bhadeshia et al., 2006).

C	Si	Mn	Ni	Cr	Mo	V	Reference
0.43	2.12	3.0					(Bhadeshia, 1979; Bhadeshia and Edmonds, 1979)
0.42	1.64	0.79	1.84	0.79	0.36	0.08	(Padmanabhan and Wood, 1984)
0.095	1.63	1.99		1.97			
0.1	1.77	2.12	2.0				
0.27	1.98	2.18		1.9			
0.27	2.01	2.16	2.07				(Chang and Bhadeshia, 1996)
0.26	1.85	2.10					
0.26	1.93	2.04		1.02			
0.46	2.10	2.15					
0.44	2.13	2.14		0.5			
0.032	0.25	2.02	7.23	0.47	0.63		(Keehan et al., 2006b,d)
0.031	0.27	2.11	9.23	0.48	0.64		
0.08	0.23	0.56	10.51	1.13	0.29		(Keehan et al., 2005)
0.061	0.22	1.21	8.6	0.46	0.41		
0.030	0.4	0.61	6.11	0.16	0.38	0.018	
0.061	0.34	0.56	6.84	0.15	0.35	0.014	(Keehan et al., 2006c)
0.011	0.38	0.53	7.04	0.14	0.40	0.016	

1.3.2 Microstructure of coalesced bainite

Davenport (1974) mentioned that when the morphology in two dimensions is the shape of needle or parallelogram, the structure arose from lath rather than plate-shaped crystals. He does not seem to have intended the coalescence, however, the analysis was consistent with the recent work about the coalesced bainite (Keehan et al., 2008b). They reconstructed the coalesced bainite in three dimensions using focused-ion beam (FIB) technique and revealed that the coalesced bainite has the lath type with a long dimension and two short dimensions; 20, 6 and 4 μm , respectively (Fig. 1.19).

Keehan et al. (2008a) found that there is a orientation gradient $3^\circ/10 \mu\text{m}$ both along and across the coalesced region (Fig. 1.20). They explained that the shape deformation associated with the coalescence is difficult to accommodate entirely elastically within the austenite; therefore the dislocations generated during plastic relaxation induced the misorientation.

1.3.3 Formation condition

According to Eq. 1.1, the strain energy due to the shape deformation increases with the aspect ratio, c/a , which determines the degree of coalescence. In this context, Chang and Bhadeshia (1996) insisted that the large undercooling below bainite start temperature can cause the co-

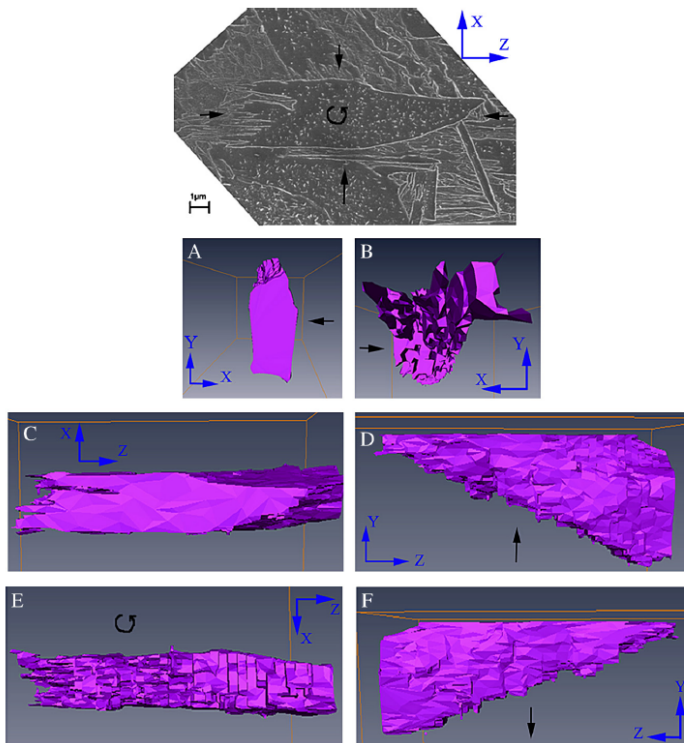


Figure 1.19: Six snapshots of coalesced bainite reconstructed in the three dimensions. Each view direction was represented by the orientation of the given axes. Reprinted from (Keehan et al., 2008b) with permission from Elsevier.

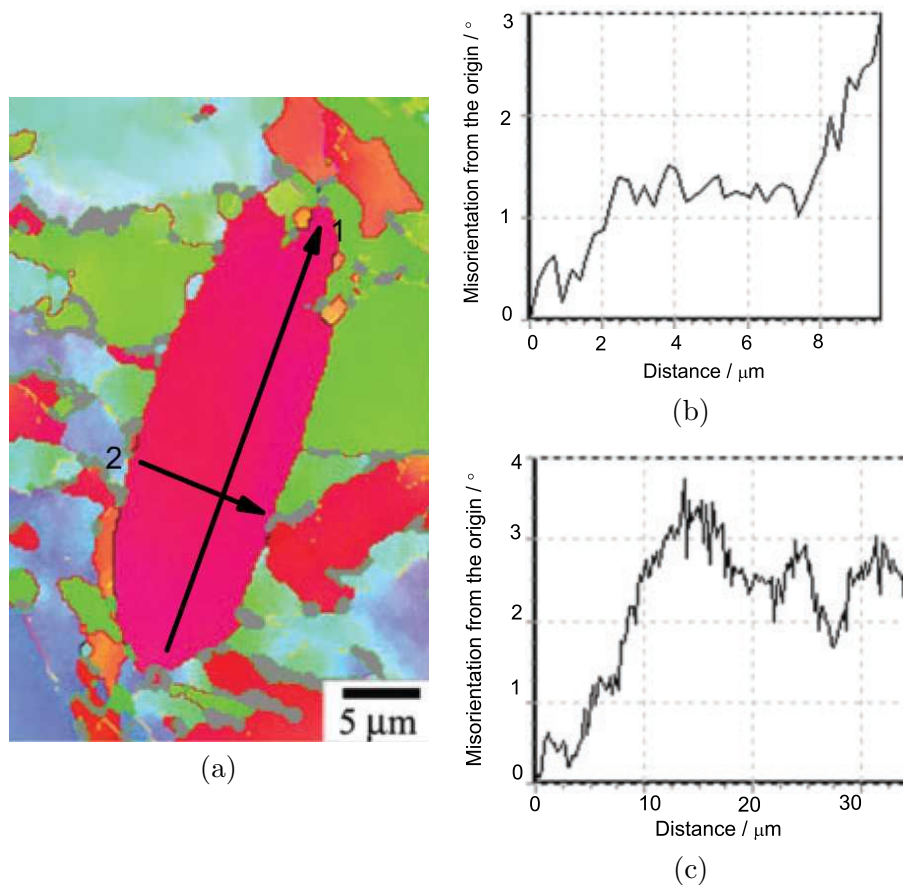


Figure 1.20: (a) Internal crystallography of coalesced bainite region measured by electron backscattering diffraction; (b),(c) the misorientation from the origin measured along the arrows of 1 and 2, respectively. Reprinted from (Keehan et al., 2008a) with permission from Maney Publishing.

alescence since the driving force becomes compatible with the strain energy associated the coalesced structure with the observed aspect ratio. They also pointed that the absence of any obstacles to block the lengthening of sub-units can provide more opportunity for them to meet, which leads to the coalescence. Therefore it was suggested that coalescence will be favoured in the early stages of transformation where the chances of impingement with other sub-units are reduced. Bhadeshia et al. (2006) demonstrated that coalescence will be preferred in large grains of austenite. Keehan et al. (2006b) reported that the coalescence was promoted in the alloy where the gap between bainite and martensite start temperature is small. It should be noticed that the sub-units in touch with each other can emerge into the coalesced structure if they are identically orientated (Bhadeshia et al., 2006). This implies that coalescence can occur not only in the bainite transformation but also in the martensite transformation even though the latter does not progress as described in Fig. 1.15. In fact, the martensitic transformation is more appropriate for the coalescence in terms of the driving force. Yang et al. (2009) interpreted that the coalescence results from the competition between carbon partitioning and interface movement; therefore it happens at low temperature, where the latter covers the distance between sub-units before carbon partitioning completes. However, the growth of bainite occurs independently with the carbon partitioning and the model cannot explain the coalescence of martensite where the carbon partitioning is excluded.

Chapter 2

Identification of coalesced structure

2.1 Introduction

It is very recent that there has been an interest in the coalesced plates during the bainite or martensite transformation (Keehan et al., 2005). So far, several intuitive theories have been suggested (Chang and Bhadeshia, 1996; Bhadeshia et al., 2006), one of these is that the coalescence requires a high driving force to endure large strain energy associated with the existence of fat plates. However, it remains the case that experimental verification of the ideas is minimal. The aim therefore was to investigate the general behaviour of coalescence during the bainite and martensite transformations. The work started from the basic characterization of the

structure, which is especially difficult for low-carbon steels such as those used for welding alloys.

2.2 Experimental method

The four alloys investigated are listed in Table 2.1, referred to as Alloy A to D. The first three were provided from ESAB AB (Sweden) and the last by POSCO (Korea). Notice that ‘A’ is known to lead to coalesced microstructures relatively easily compared to ‘B’ (Keehan et al., 2006b). Alloy C was designed to have a martensite-start (M_S) temperature comparable to that of Alloy A. Alloy D was manufactured originally in the context of dual-phase steels.

The heat treatments which cause martensitic and bainitic transformations were conducted using dilatometry. The M_S temperature following a full austenitization at 1250 °C for 3 minutes was measured using the offset method of (Yang and Bhadeshia, 2007), which was consistently applied throughout this work for measuring all transformation temperatures. The bainitic transformation was studied at a variety of isothermal temperatures above the measured M_S temperature.

Martensitic and bainitic structures were characterized by optical and electron microscopy, on samples etched using 2% nital. Transmission electron microscopy (TEM) was also applied to examine fine substructures, especially, retained austenite for Alloy A and B. A solution containing 5%

Table 2.1: Whole composition of investigated alloys (wt%).

	C	Si	Mn	P	S	Cr	Ni	Mo	W	Co	V	Nb	Cu	Al	Ti	B	O	N
A	0.030	0.23	2.05	0.010	0.008	0.43	7.1	0.63	0.004	0.008	0.021	0.004	0.02	0.001	0.011	0.0012	0.031	0.011
B	0.025	0.39	0.58	0.010	0.009	0.15	6.5	0.39	0.001	0.009	0.018	0.002	0.02	0.001	0.015	0.0012	0.033	0.009
C	0.13	0.37	3.60	0.008	0.005	1.03	0.04	0.49	0.005	0.008	0.032	0.005	0.01	0.003	0.016	0.0006	0.020	0.013
D	0.084	1.53	1.97			0.71						0.031						0.23

perchloric acid mixed with 95 % acetic acid was used for electropolishing the thin foils for transmission microscopy.

The electron backscattered diffraction (EBSD) technique was applied to identifying crystallographic boundaries in the martensitic structure and the distribution of individual unit sizes was obtained by a linear intercept method using OIM Analysis 5.31, which is a specialized software for EBSD data analysis.

2.3 Results

2.3.1 Dilatometry

Fig. 2.1 shows the behaviour of the measured transformation temperature as a function of an increasing cooling rate. Since the martensitic transformation is expected to be athermal, the transformation-start temperature should be independent of cooling rate. The M_S temperature was therefore estimated as the averaged value of transformation temperatures corresponding to the cooling rates higher than that indicated by the arrows on Fig. 2.1. Notice that the hardenability of Alloy B was too low to detect a series of constant transformation temperature under given cooling rates. Since the higher cooling rate than those in Fig. 2.1 normally produced irregular curves for all alloys, the values corresponding to the two highest cooling rate were averaged for Alloy B.

The bainitic transformation just above the M_S temperature was inten-

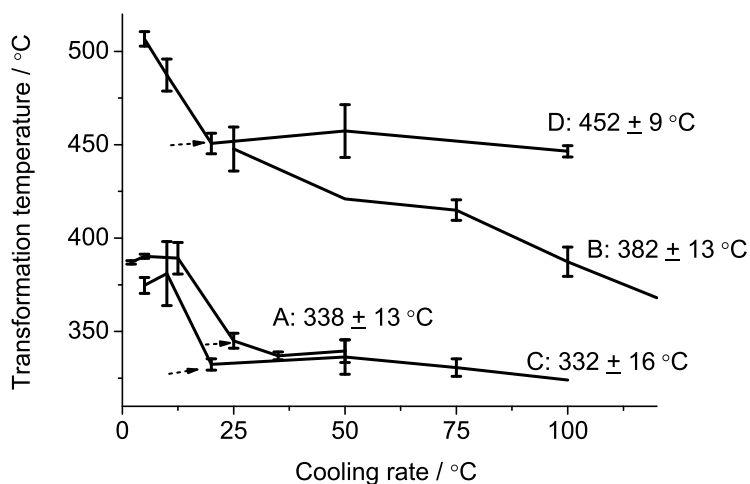


Figure 2.1: Variation of transformation temperature on increasing cooling rate.

tionally examined in Fig. 2.2 since the coalescence is highly likely to occur at low temperatures. Comparatively large amount of bainite is formed in Alloys B, C and D and relatively small in A. It also indicates that the overall transformation rates of A and C are slow compared to those of Alloys B and D, where the reaction temperature in the former cases was lower.

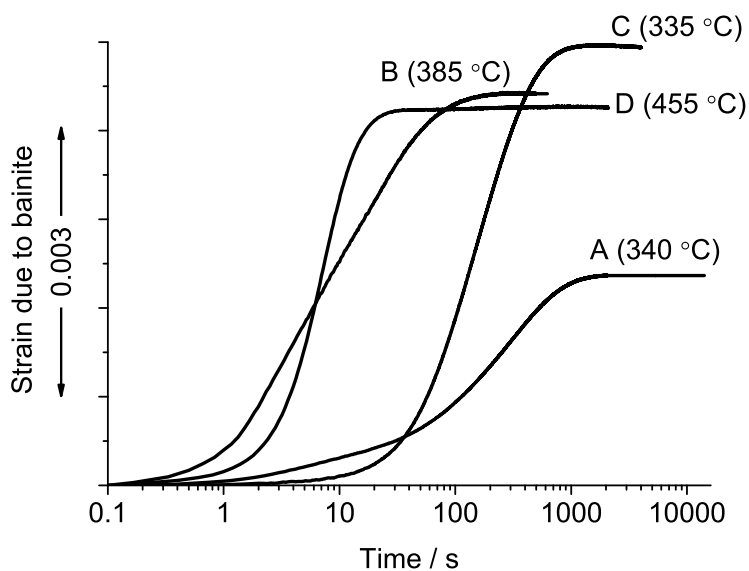


Figure 2.2: Strain due to the bainite transformation at 340, 385, 335 and 455 °C for Alloys A, B, C and D, respectively. Notice that the isothermal temperatures are just above the M_S temperature for each alloy.

2.3.2 Thermodynamics

The free energy changes corresponding to the diffusionless transformation of austenite (γ) to ferrite (α) for given alloys were obtained using the thermodynamic program which accesses MTDATA (Okumura and Sourmail, 2004) with the results illustrated in Fig. 2.3, where the values corresponding to the measured M_S temperature for each alloy are indicated by the horizontal lines on each curve. Only that for Alloy C were high with -1837 J mol^{-1} and the others lie between -1373 to -1405 J mol^{-1} . This implies that the critical driving forces for the nucleation of martensite for Alloys A,B and D are comparable and that for Alloy D is large. However, the net driving force corresponding to the undercooling from the M_S temperature varies equally for all alloys.

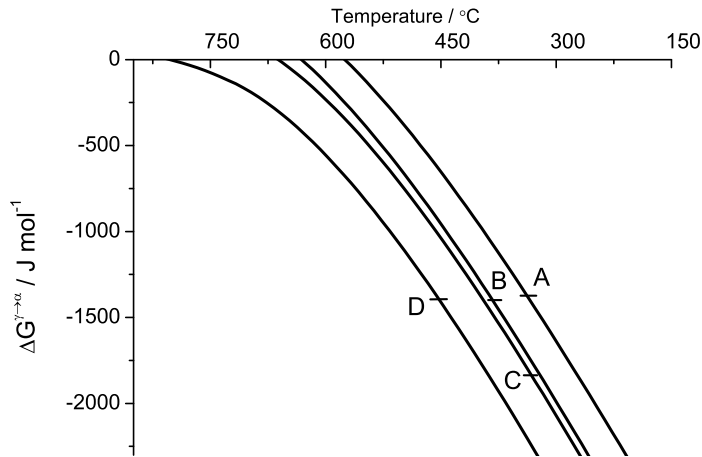


Figure 2.3: The free energy change corresponding to the diffusionless transformation of austenite (γ) to ferrite (α) for Alloys A, B, C and D.

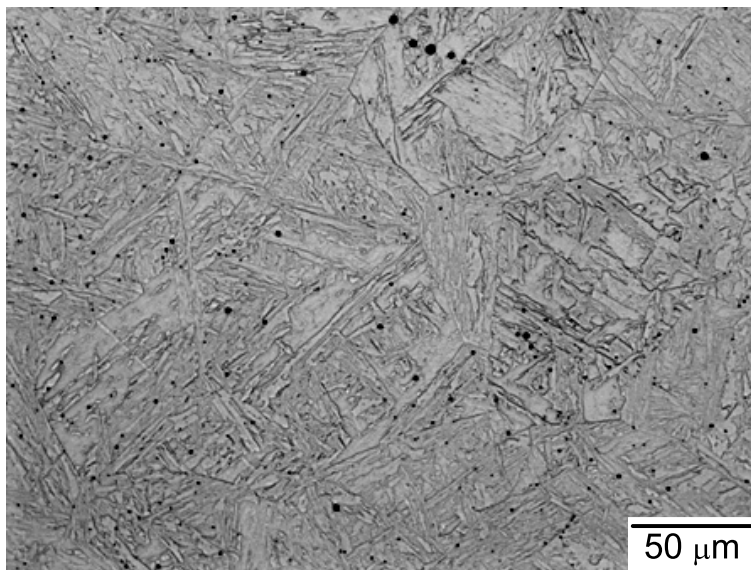
2.3.3 Microscopy

Fig. 2.4-2.7 show fully martensitic and bainitic structures. In general, the visible boundaries in the martensitic structure are straight, whereas those in bainitic structure are relatively irregular.

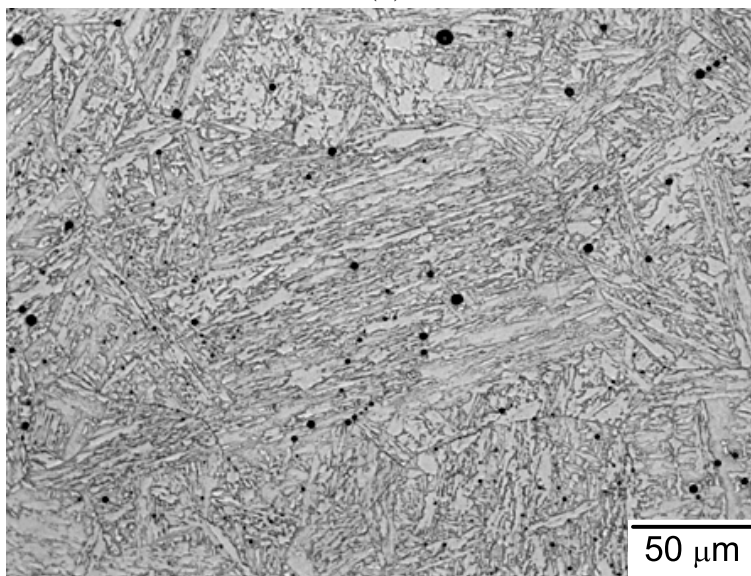
The difference in martensitic and bainitic structure becomes more apparent using scanning electron microscopy (Fig. 2.8-2.11). Substructures in martensite were definitely finer than those in bainite and the boundaries between the substructures for the former are much sharper than those for bainite. Considering the formation mechanism of martensite and bainite, in low carbon steels such as the ones considered here, the former hardly retains austenite in the absence of partitioning.

Consequently the boundaries in the low carbon martensite are mainly between martensite plates whereas those in predominantly bainitic structure are like to be with thin retained austenite films. The two boundary structures react differently to the etchant, which leads to the observed difference in optical and electron microscopy.

The arrows in the individual micrographs indicate regions where structures have coalesced, which are abnormally large compared to the surrounding regions, one exception is illustrated in Fig. 2.9b, where there is a cluster of the large structures. This apparent clustering might be the sectioning effect and hence has been excluded from the discussion that follows.

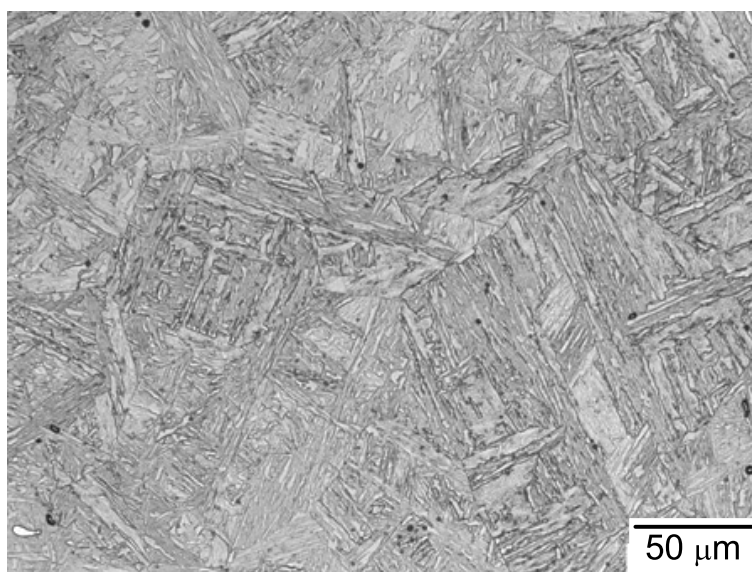


(a)

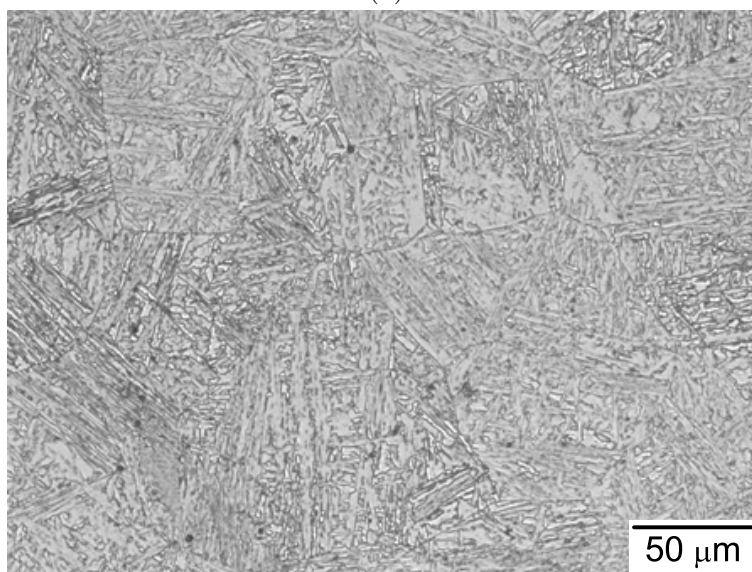


(b)

Figure 2.4: Optical micrographs showing (a) martensitic and (b) bainitic structure for Alloy A formed at 340 °C.

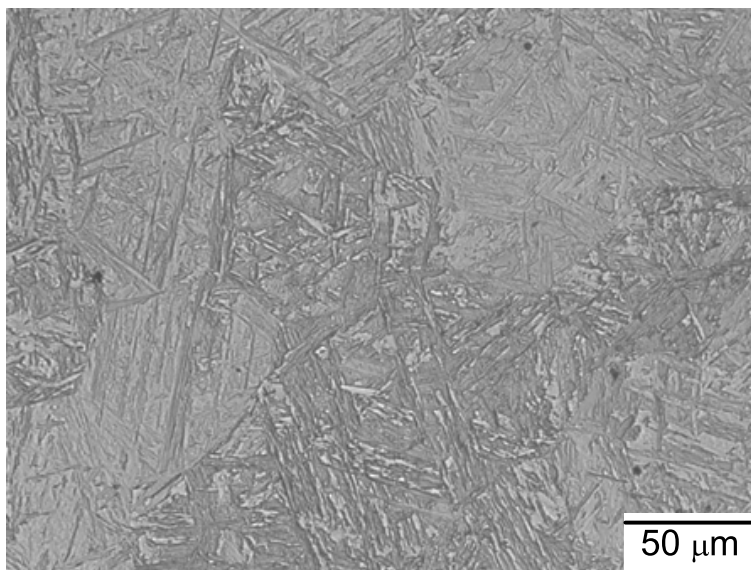


(a)

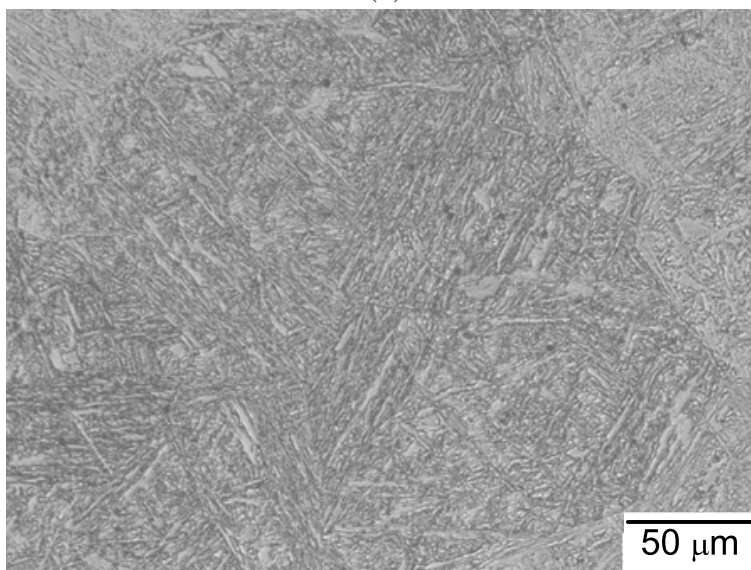


(b)

Figure 2.5: Optical micrographs showing (a) martensitic and (b) bainitic structure for Alloy B formed at 385 °C.

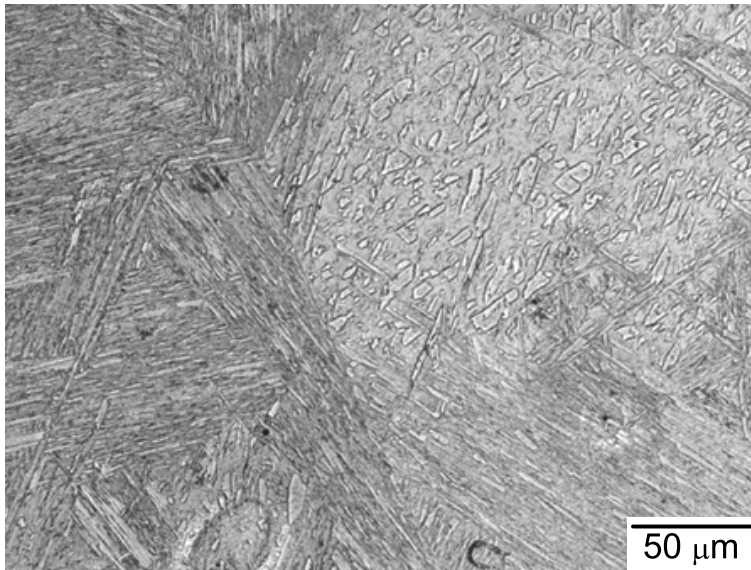


(a)

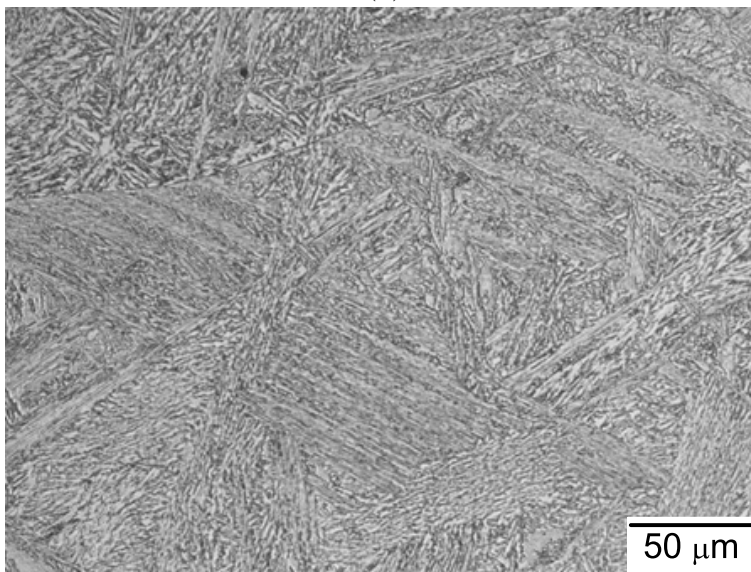


(b)

Figure 2.6: Optical micrographs showing (a) martensitic and (b) bainitic structure for Alloy C formed at 335 °C.

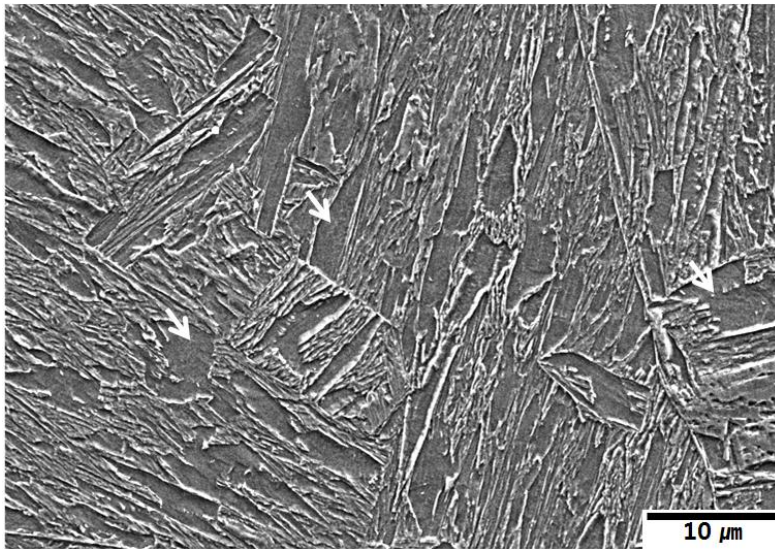


(a)

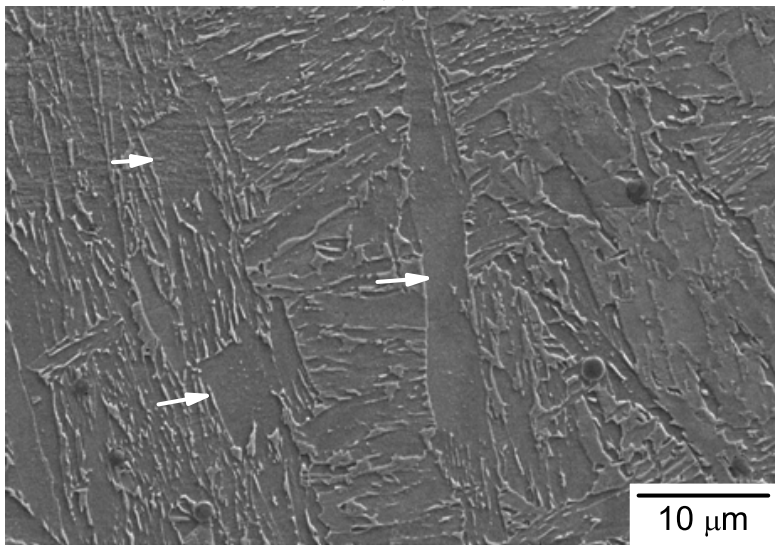


(b)

Figure 2.7: Optical micrographs showing (a) martensitic and (b) bainitic structure for Alloy D at 455 °C.

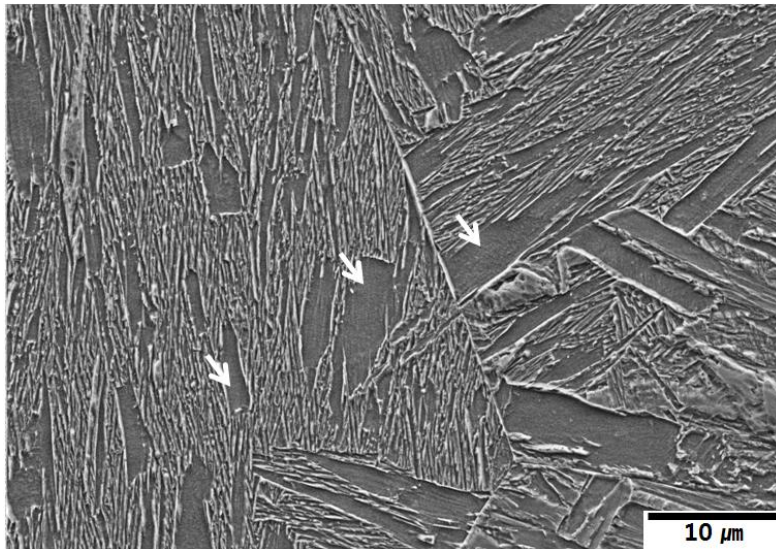


(a)

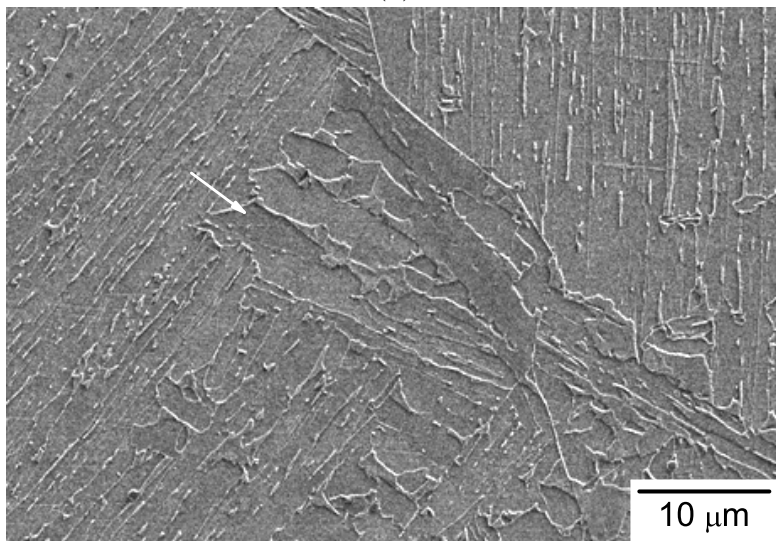


(b)

Figure 2.8: Scanning electron micrographs showing (a) martensitic and (b) bainitic structure for Alloy A formed at 340 °C.

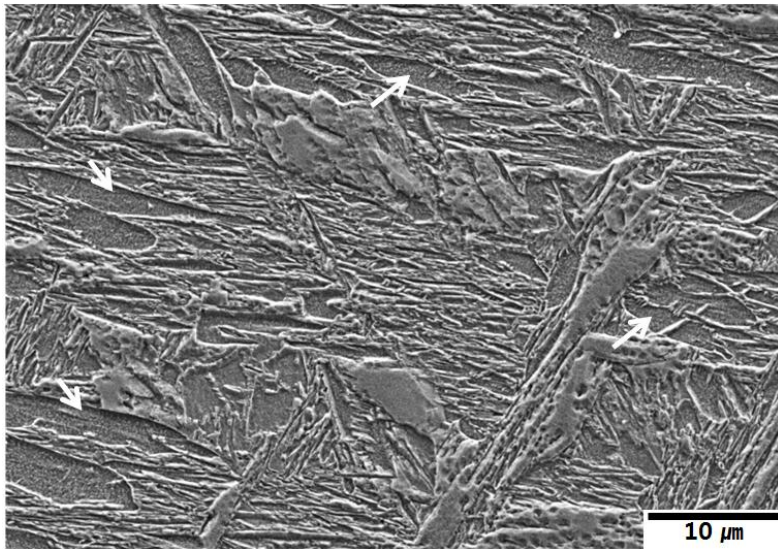


(a)

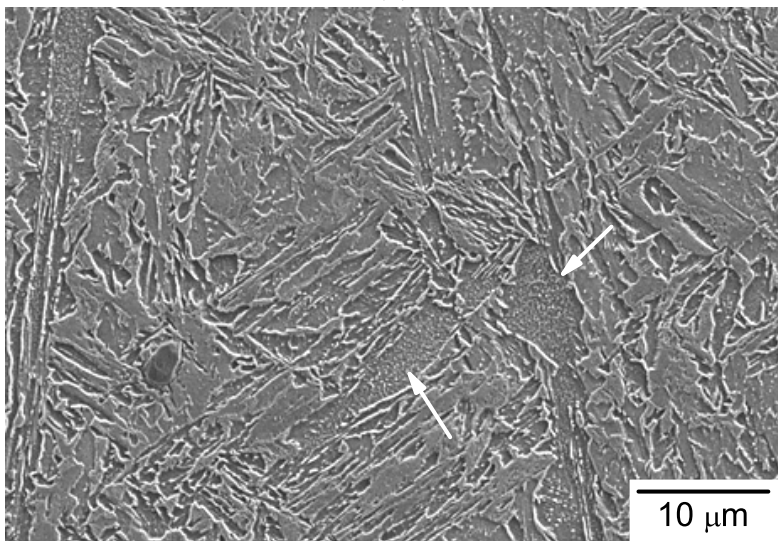


(b)

Figure 2.9: Scanning electron micrographs showing (a) martensitic and (b) bainitic structure for Alloy B formed at 385 °C.

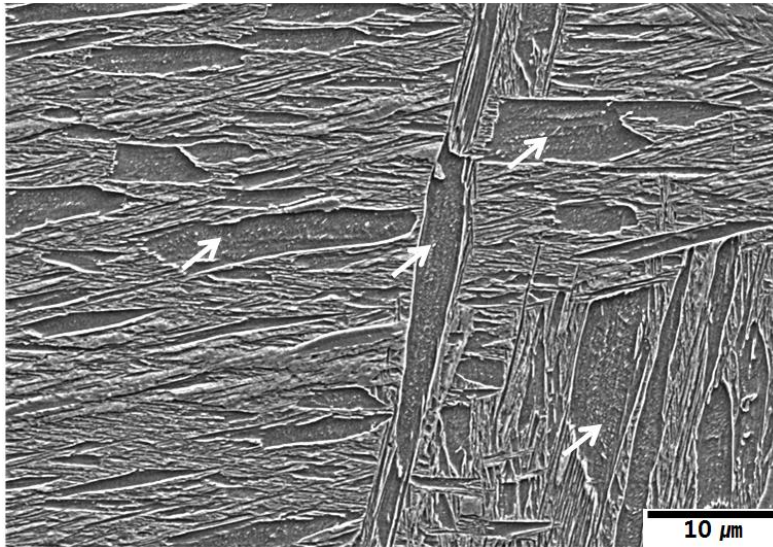


(a)

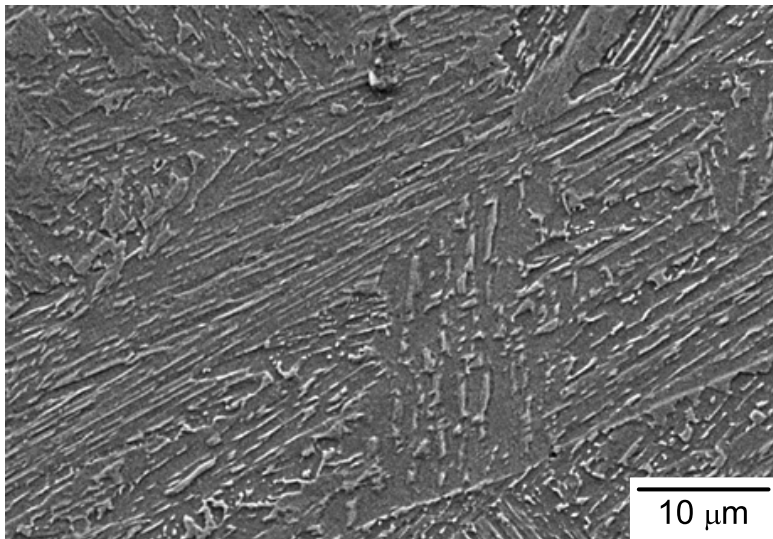


(b)

Figure 2.10: Scanning electron micrographs showing (a) martensitic and (b) bainitic structure for Alloy C formed at 335 °C.



(a)

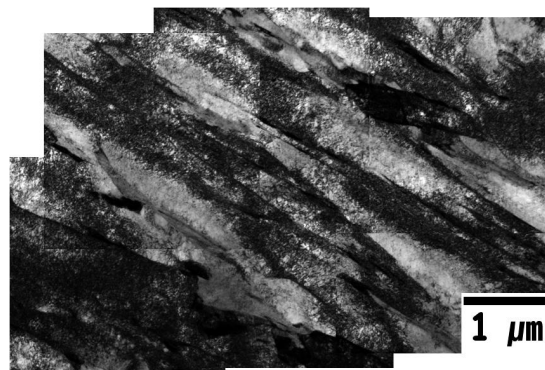


(b)

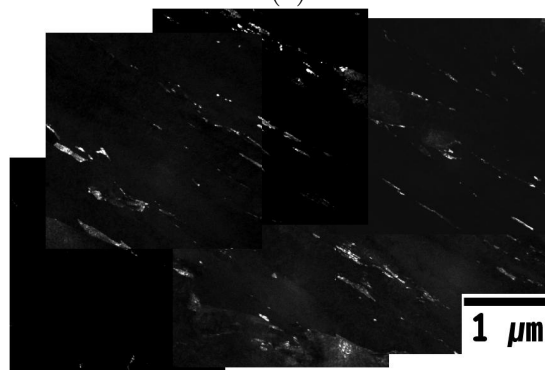
Figure 2.11: Scanning electron micrographs showing (a) martensitic and (b) bainitic structure for Alloy D formed at 455 °C.

2.3.4 TEM on bainite of Alloy A and B

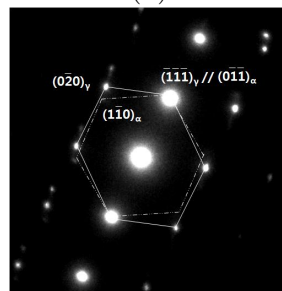
Transmission electron microscopy (TEM) was conducted on bainite in Alloys A and B (Fig. 2.12 and 2.13), which are formed at 340 and 385 °C, respectively. The bainitic structure of both alloys consisted of sets of parallel ferrite laths. Coarse plates of bainitic ferrite were also found in Alloy B, consistent with the observation reported in Fig. 2.9b. Retained austenite in Alloy A was in the type of film, however, it hardly extended longer than 1 μm . On the other hand, that in Alloy B was not only present as films but also islands.



(a)



(b)



(c)

Figure 2.12: TEM micrographs for bainite of Alloy A formed at 340 °C; (a) bright field image; (b) dark field image using $(0\bar{2}0)$ austenite reflection; (c) diffraction pattern at the interface between austenite (solid line) and bainitic ferrite (dashed line).

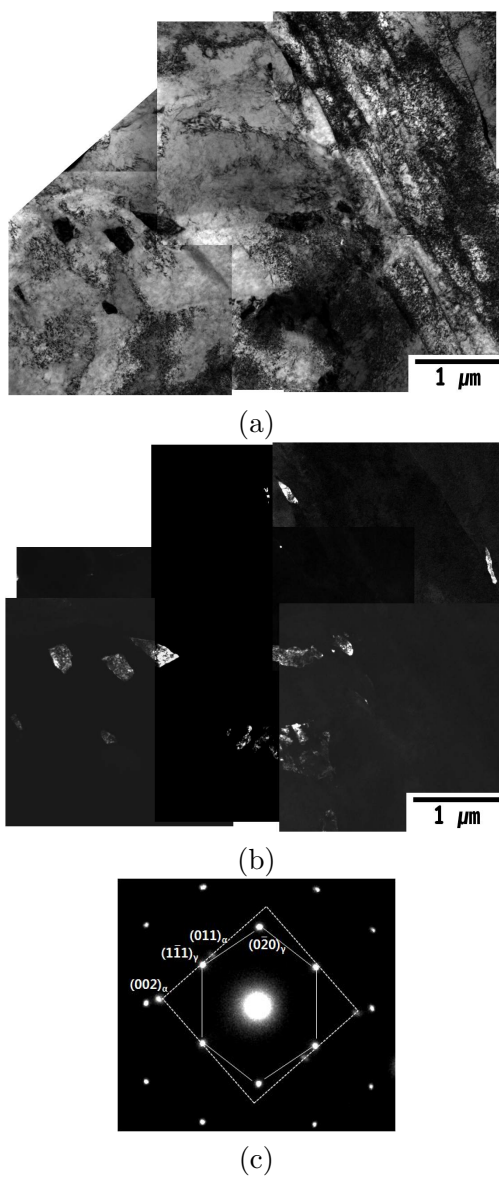


Figure 2.13: TEM micrographs for bainite of Alloy B formed at 385 °C; (a) bright field image; (b) dark field image using $(0\bar{2}0)$ austenite reflection; (c) diffraction pattern at the interface between austenite (solid line) and bainitic ferrite (dashed line).

2.4 Discussion

2.4.1 Coalescence in martensite

For the alloys investigated, martensite has been found to be more prone to be coalescence relative to bainite. Therefore, the distribution of grain size for the former was measured to find an evidence for the coalescence using EBSD technology. The distribution might be expected to be bimodal, representing a mixture of coarse and fine plates. Here, the statistics of crystallographically homogeneous regions with a misorientation less than 1° were analysed. Fig. 2.14-2.17 show the distribution of the scale of the martensitic structure, where the dash lines are fitted assuming log-normal distribution, which will reflect sectioning effect, and dash-dot lines assuming bimodal distribution. The practical distribution matches the latter definitely better, which demonstrate the coalescence. The coalescence in martensitic growth has been hardly reported than compared to that in bainite, however, once the restriction for the strain energy disappears at a certain temperature, it is expected to be accelerated due to the increasing driving force by continuous cooling.

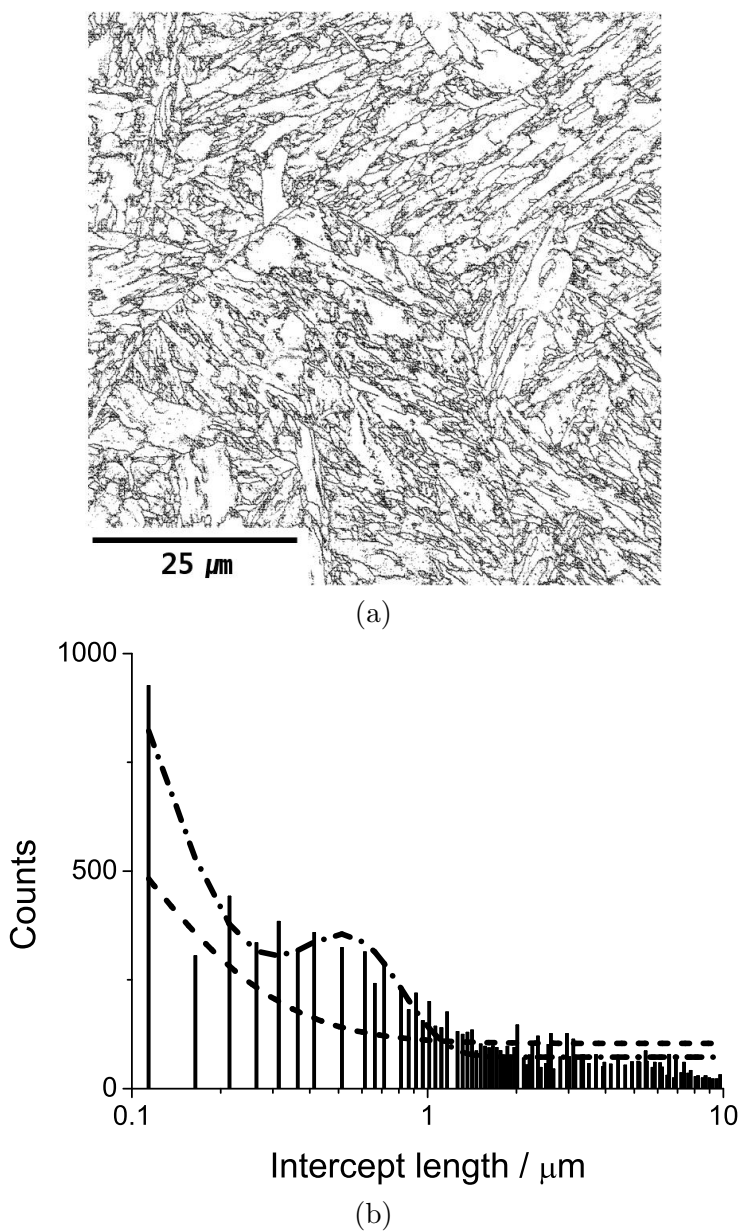


Figure 2.14: The distribution of grain size for martensite of Alloy A; (a) grain boundaries detected by EBSD; (b) intercept length distribution.

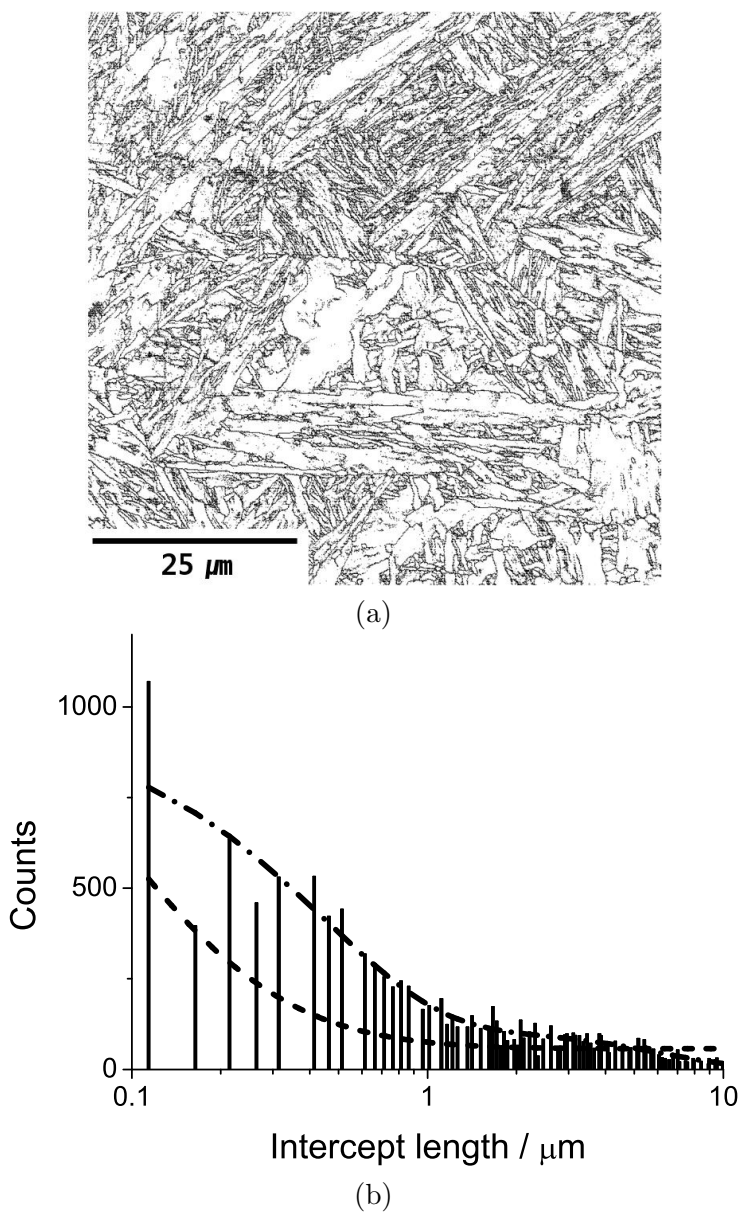


Figure 2.15: The distribution of grain size for martensite of Alloy B; (a) grain boundaries detected by EBSD; (b) intercept length distribution.

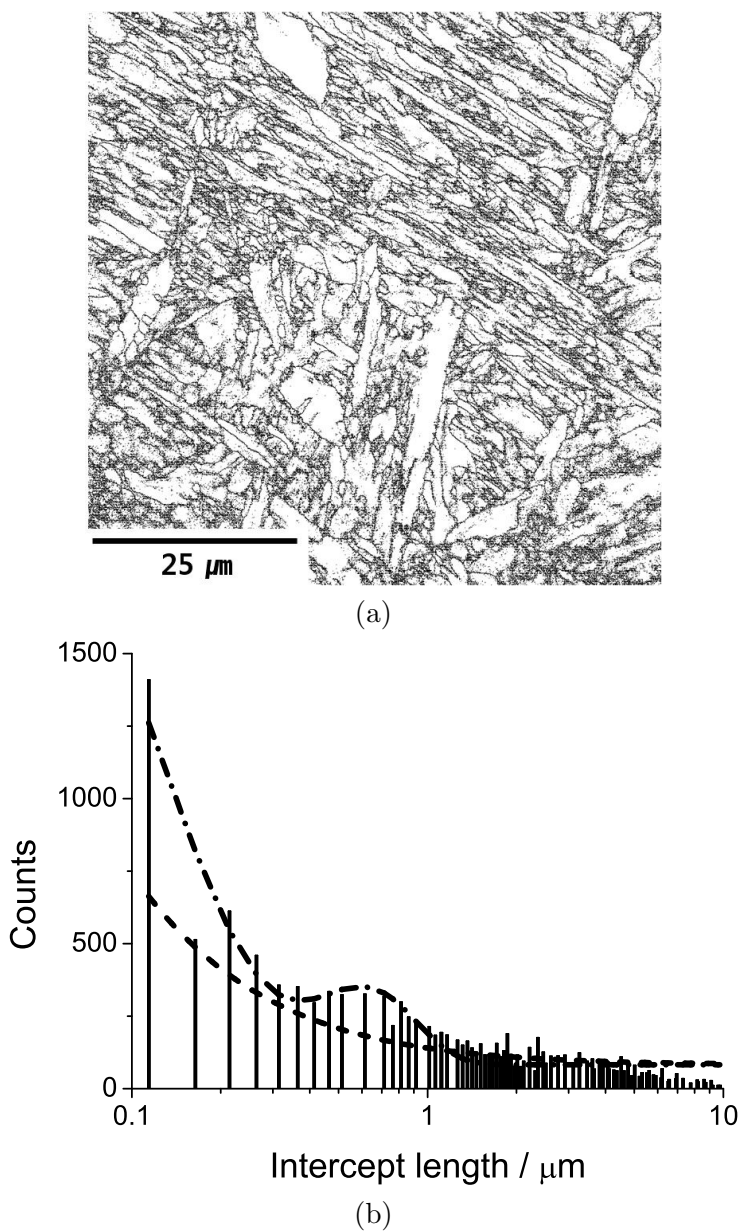


Figure 2.16: The distribution of grain size for martensite of Alloy C; (a) grain boundaries detected by EBSD; (b) intercept length distribution.

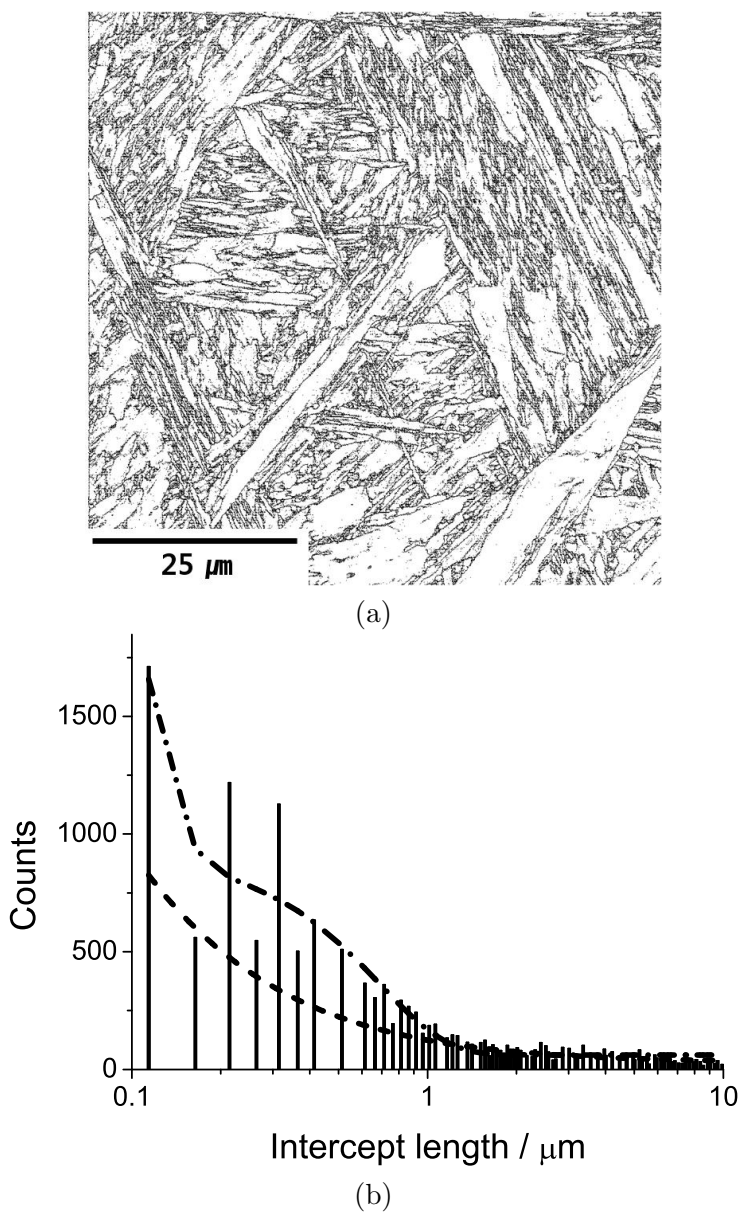


Figure 2.17: The distribution of grain size for martensite of Alloy D; (a) grain boundaries detected by EBSD; (b) intercept length distribution.

2.4.2 Coalescence in bainite

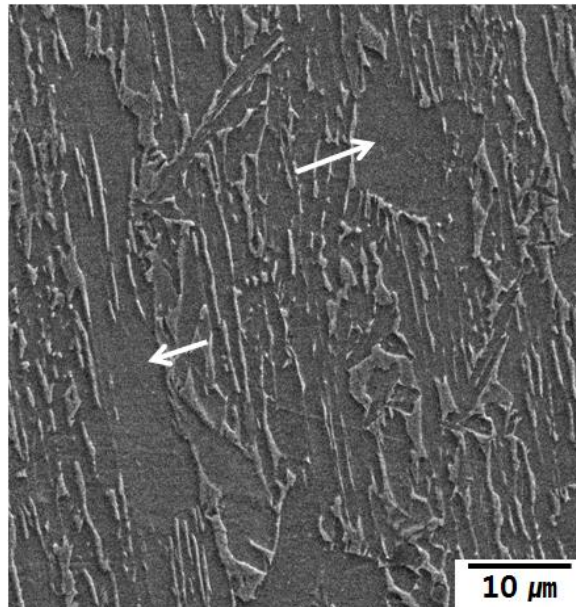
Only the bainitic structure in Alloys A and C showed coalescence (Fig 2.8b, 2.10b) and their typical structures were presented in Figs. 2.18 and 2.19.

It is interesting that the temperatures at which the coalescence of bainite in Alloys A and C occurred during the bainite transformation were lower than those in B and D which did not exhibit coalescence (Fig. 2.1). Notice that the lower temperature in this case did not aid the coalescence with respect to the driving force (Fig. 2.3). Instead, the lower temperature can retard the partitioning of carbon. An analytical equation was used for estimation of carbon partitioning time (t_d) for each bainite isothermal transformation temperature:

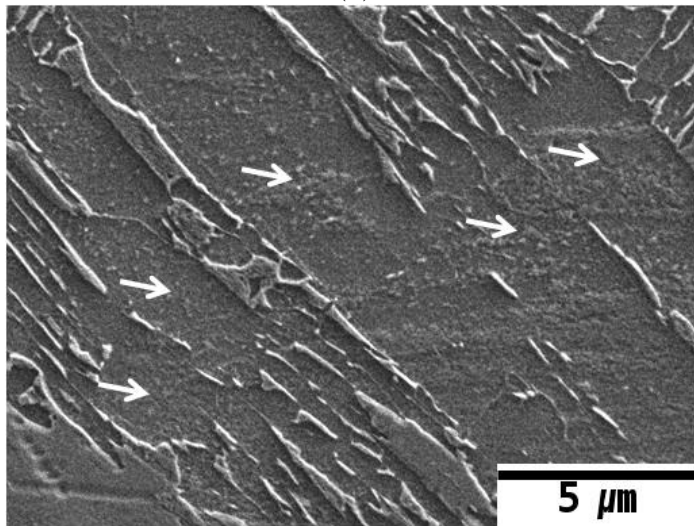
$$t_d^{\frac{1}{2}} = \frac{w(\bar{x} - x^{\alpha\gamma})\pi^{\frac{1}{2}}}{4\bar{D}^{\frac{1}{2}}(x^{\gamma\alpha} - \bar{x})} \quad (2.1)$$

where \bar{D} is an averaged carbon diffusivity in austenite; w is the thickness of the bainitic ferrite; $x^{\alpha\gamma}$ and $x^{\gamma\alpha}$ are paraequilibrium carbon mole fractions in ferrite and austenite, respectively; \bar{x} is mean carbon mole fraction. The diffusivity and mole fraction of carbon were obtained from (Bhadeshia and Mateo, 2001). The whole information and results for the calculation are listed in Table 2.2.

As expected, the lower temperature leads to a longer partitioning period. It is noticeable that there are three orders of magnitude difference

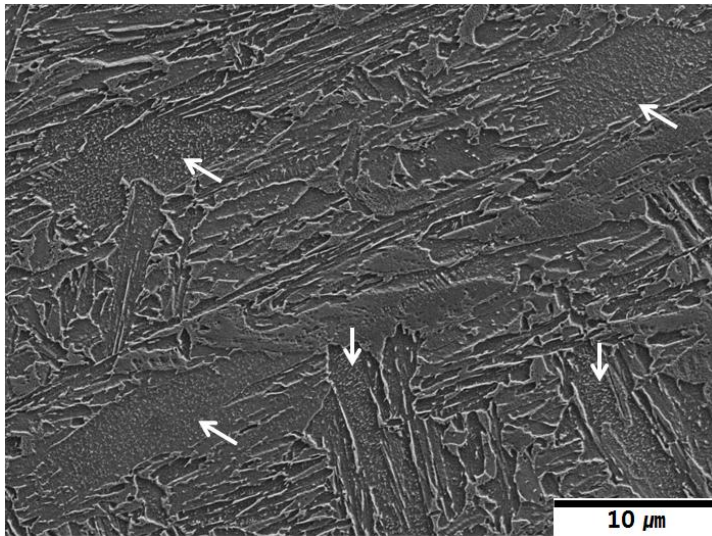


(a)

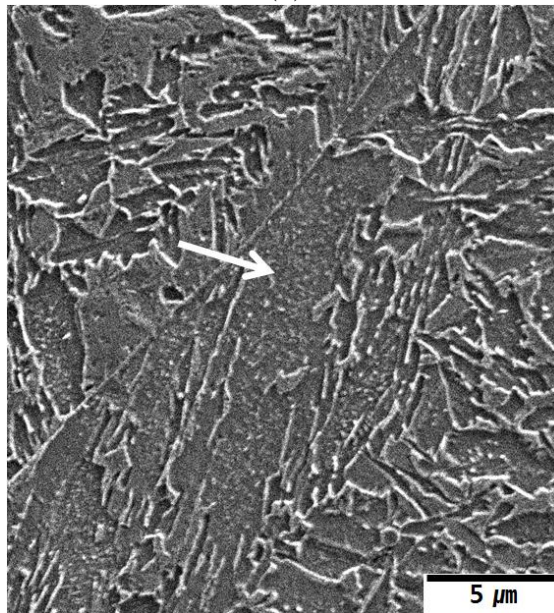


(b)

Figure 2.18: Typical structure of coalesced bainite (indicated by arrow) which formed at 340 °C for alloy A.



(a)



(b)

Figure 2.19: Typical structure of coalesced bainite (indicated by arrow) formed at 335 °C for alloy C.

Table 2.2: The input parameters for the analytic equation of Eq. 2.1 and the corresponding results

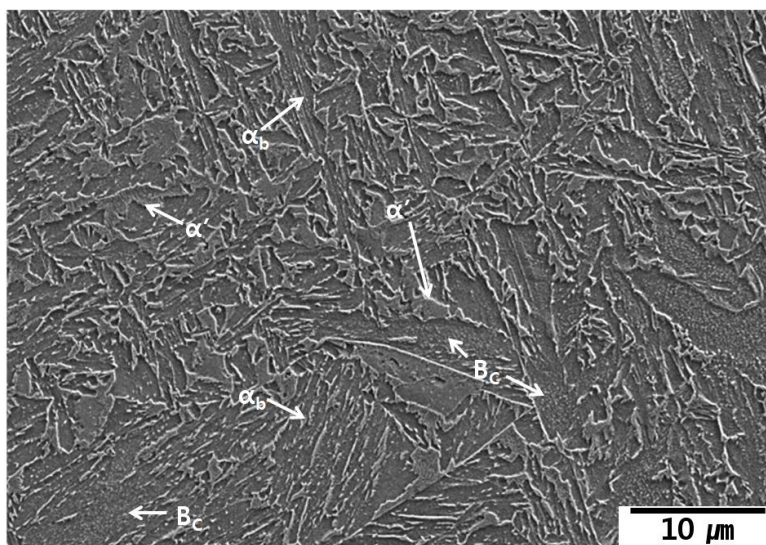
	A	B	C	D
w (μm)	0.2	0.2	0.2	0.2
\bar{D} (m^2s^{-1})	9.37×10^{-17}	5.91×10^{-16}	7.65×10^{-17}	6.97×10^{-15}
$x^{\alpha\gamma}$	2.1×10^{-4}	3.2×10^{-4}	4.7×10^{-4}	8.7×10^{-4}
$x^{\gamma\alpha}$	0.1241	0.1224	0.1524	0.1229
\bar{x}	0.0014	0.0012	0.006	0.0038
t_d (s)	7.88×10^{-3}	7.01×10^{-4}	1.46×10^{-1}	6.82×10^{-4}

in t_d between Alloys C and B, D. This results in two effects; first, given that it is believed that the growth of bainitic ferrite ends before the carbon partitions, a greater partitioning time provides an opportunity for a bainitic ferrite grow to meet an adjacent plate; second, it also intrude the formation of retained austenite film, which plays a role of barrier for the coalescence.

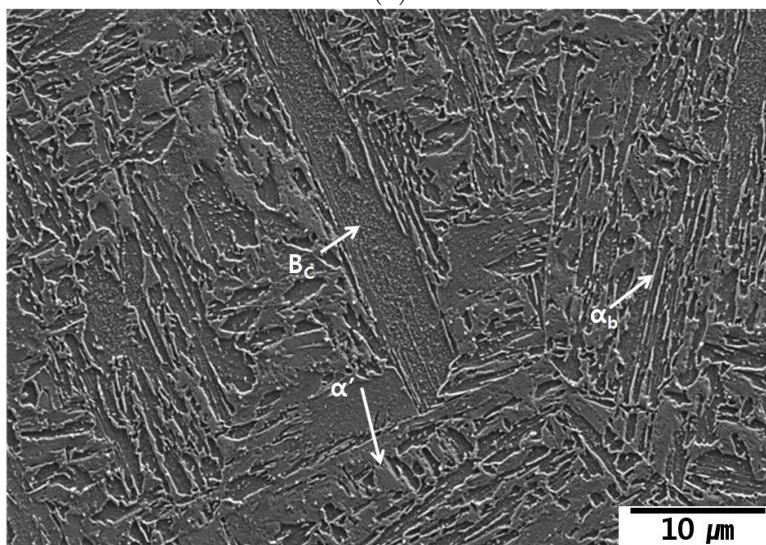
2.4.3 Coalescence of bainite in various temperatures

Due to the relatively large amount of bainite that forms in Alloy C (Fig. 2.2), it was selected to investigate coalescence as a function of temperature. Fig 2.20-2.22 show the evolution of microstructures resulting from isothermal transformation to bainite followed by quenching during which the remaining austenite transforms into martensite. As expected, the fraction of martensite indicated by α' increased following increasing isothermal transformation temperatures since less bainite indicated by α_b then forms. The coalescence of bainite, indicated by 'B_C' on the figures, occurred at the two lowest isothermal transformation temperatures, 335 and 345 °C. The relatively large structures of α_b indicated by dash arrows are considered to result in sectioning effect due to the absence of surrounding lath structures.

Since the carbon partitioning time over the investigated temperature range does not alter much (Fig. 2.23), a critical driving force in the range of 1730 and 1660 J mol⁻¹, which are the free energy change corresponding to 345 and 355 °C, respectively might be assumed to control the coalescence.

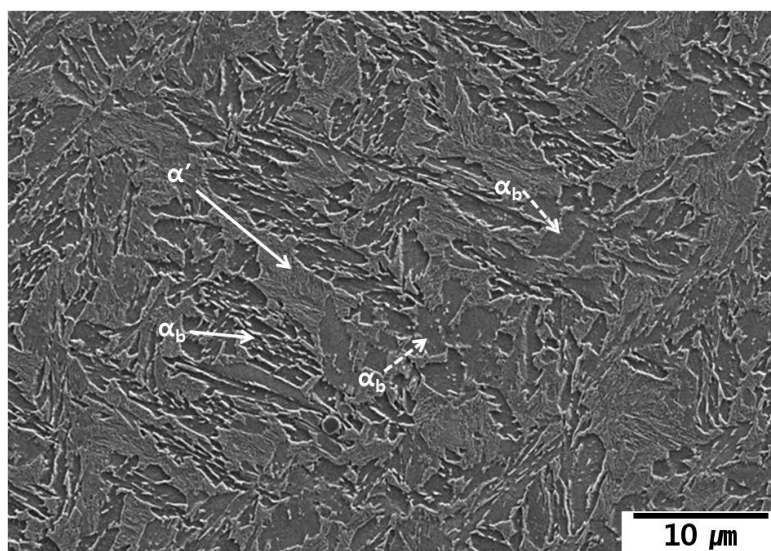


(a)

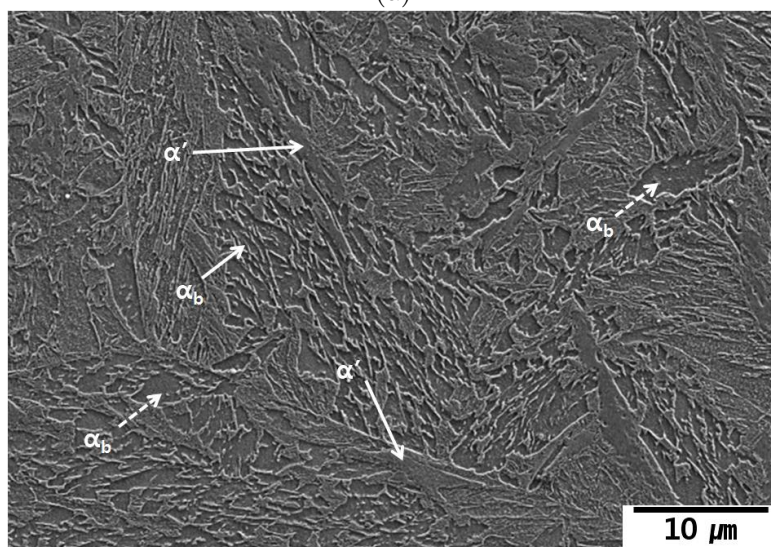


(b)

Figure 2.20: Microstructures resulting from isothermal transformation at (a) 335 °C and (b) 345 °C followed by quenching to ambient temperature.



(a)



(b)

Figure 2.21: Microstructures resulting from isothermal transformation at (a) 355 °C and (b) 365 °C followed by quenching to ambient temperature.

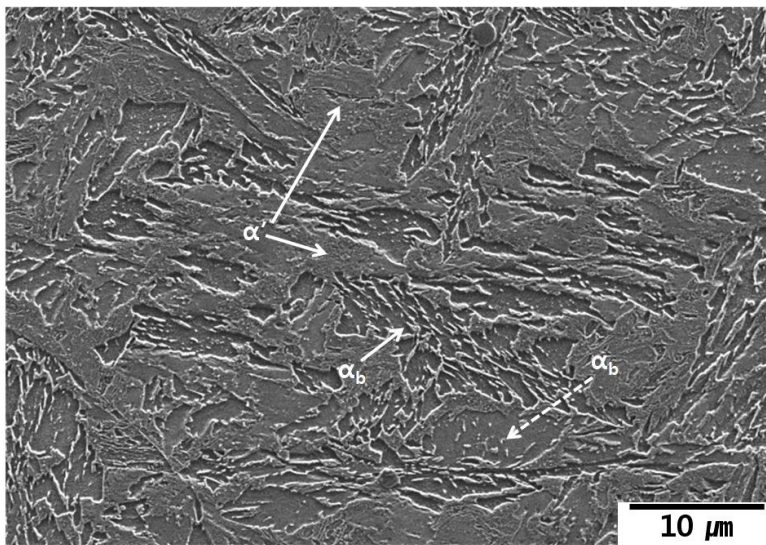


Figure 2.22: Microstructures resulting from isothermal transformation at 375 °C followed by quenching to ambient temperature

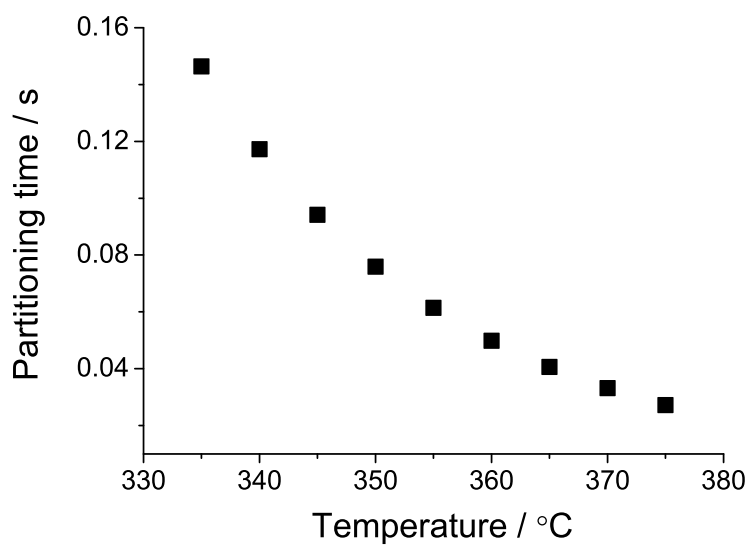


Figure 2.23: Calculated carbon partitioning time at the bainite transformation temperatures for Alloy C.

2.5 Conclusions

Low-carbon martensite have been found to exhibit coalescence in all the alloys examined, resulting in a bimodal distribution of grain size. Such a distribution cannot be rationalized if it is assumed that the observations correspond to sectioning effect. The coalescence of bainite occurred selectively at relatively low transformation temperatures, where carbon partitioning is retarded. The coalescence in bainite of Alloy C was observed at the two lowest transformation temperatures, 335 and 345 °C and it did not occur above 355 °C. Therefore, the related critical driving force in the alloy is likely to be between 1730 and 1660 Jmol⁻¹, which correspond to the free energy changes at 345 and 355 °C, respectively.

Chapter 3

Misorientation within coalesced structure

3.1 Introduction

Coalescence in bainitic structure is recognized by abnormally coarse structures compared to the surroundings (Keehan et al., 2006b; Chang and Bhadeshia, 1996). The mechanism for the formation of this structure involves the coalescence, not coarsening, of identical platelets, as shown by the persistence of retained austenite between individual platelets in the non-coalesced region (Chang and Bhadeshia, 1996). This kind of characterization is limited in the case of martensite where austenite films are difficult to retain due to the absence of carbon partitioning. The associated thermodynamics opposes the coalescence process because it leads to

an increase in strain energy is proportional to the thickness of the plates. In this context, the existence of an orientation gradient within a large unit of coalesced bainitic ferrites provided a new evidence for the merging of fine platelets (Keehan et al., 2008a). The present chapter deals with the further investigation of the orientation gradient within a coalesced structure. It is confirmed that coalesced structure consists of several separate platelets that are slightly misoriented. A simple model for the misorientations is also suggested.

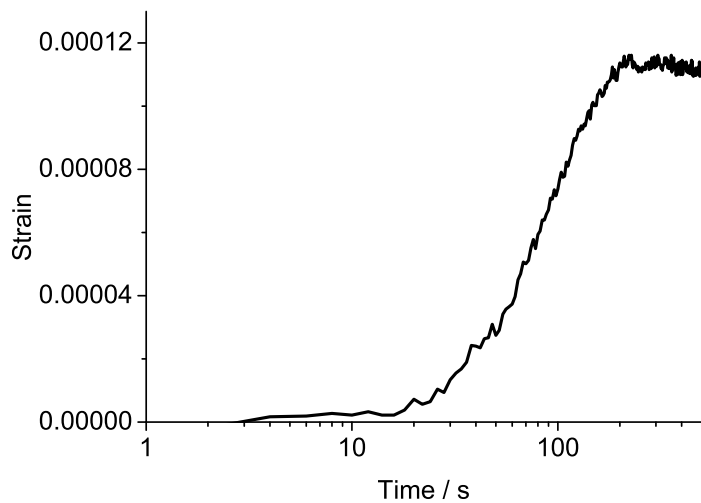
3.2 Experimental method

Alloy A in chapter 2 was used. The isothermal transformation following austenitization at 950 °C for 5 minutes was conducted at 385 °C for 2000 s based on the work of (Pak et al., 2008) and the microstructure produced from the process was examined using field emission gun scanning electron microscopy (FEGSEM). However it turned out to be inappropriate for generating the expected bainite transformation. Therefore, martensite-start (M_S) temperature under the austenitization was carefully measured. Transmission electron microscopy was conducted on a sample prepared specifically from a grain of coalesced structure using the focused ion beam technique, with the ion beam accelerating voltage reduced from 30 kV to 5 kV for the final delicate milling.

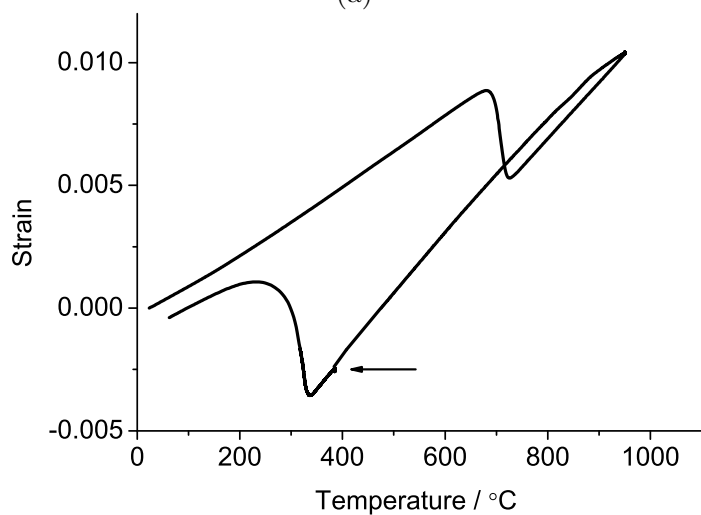
3.3 Results and discussion

3.3.1 Dilatometry

The isothermal transformation (Fig. 3.1a) was conducted in the region of whole dilatometry curve (Fig. 3.1b) indicated by the arrow . It is evident that the bainite hardly formed and the subsequent quenching induced almost fully martensitic transformation. This implies that the assumed M_S temperature was incorrect. Therefore the transformation temperatures as a function of cooling rates were investigated using the offset method (Yang and Bhadeshia, 2007) to estimate a true M_S temperature (Fig. 3.2). Normally the transformation temperature should decrease as the cooling rate increases and become constant at a sufficiently high cooling rate, which is athermal characteristic of martensite transformation. In this context, the behaviour in Fig. 3.2 is too irregular to find the M_S temperature. Fortunately the final transformation following isothermal treatment of Fig. 3.1b commenced at the temperature comparable to the lowest temperature in Fig. 3.2 (Fig. 3.3). Therefore an averaged value $337 \pm 2^\circ\text{C}$ was estimated as the M_S temperature. It should be noted that averaging all values in Fig. 3.2 causes an overestimation of M_s temperature, which resulted in the selection of higher isothermal transformation temperature, where little transformation occurred.



(a)



(b)

Figure 3.1: Dilatometry curve for (a) isothermal transformation at 385 °C and (b) whole temperature range.

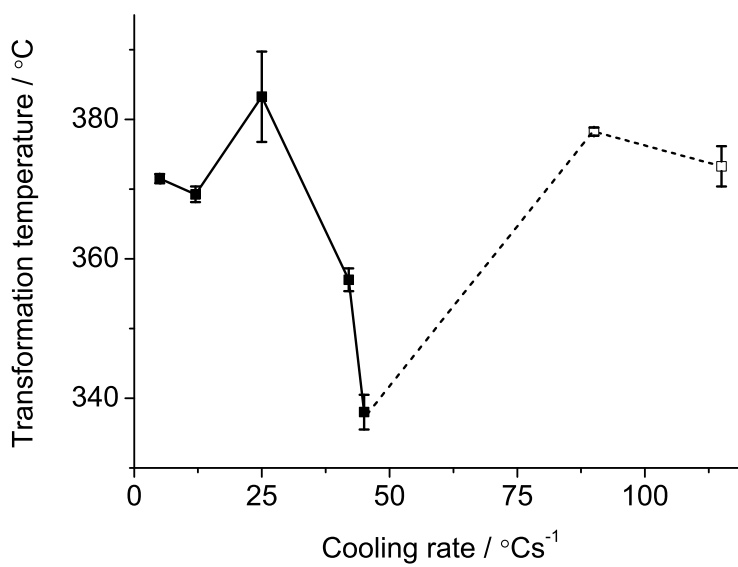


Figure 3.2: The measured transformation temperature as a function of cooling rate. The values on dotted line were excluded from consideration following comparison with Fig. 3.3.

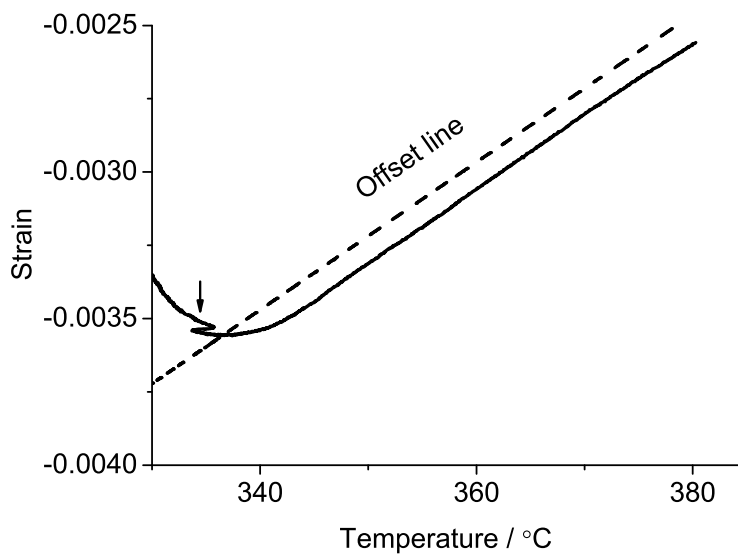


Figure 3.3: Illustration to find the start temperature of martensite transformation following the isothermal process. Dashed line corresponds to the offset line and the irregular curve indicated by the arrow is due to the unstable cooling in the machine.

3.3.2 Microscopy

The overall microstructure produced from the present dilatometric experiments contained a lot of coarse structures (Fig. 3.4a). The morphology investigated with higher magnification is consistent with that of the reported typical coalesced structure ((Fig. 3.4b, c). Therefore, Fig. 3.4a and b are better interpreted to result from the coalescence of martensite.

3.3.3 TEM microscopy and diffraction

Fig. 3.5 shows a large plate of coalesced martensite in the region marked 'A', surrounded by the ordinary fine plates of martensite in the area designated 'B'. Referring to the axes on Fig. 3.5, the plane of observation in the transmission electron microscope was xz to ensure that the features observed correspond only to the coalesced martensite.

The transmission electron micrograph in Fig. 3.6 shows surprising visible boundaries between individual platelets. It proves that the observed structure in Fig. 3.5b was formed by the coalescence of each unit, not the coarsening of single unit. It indicates also that there may have been small misorientations between the platelets before they coalesced.

The electron diffraction patterns from ferrite platelets A , B and C shown in Fig. 3.6 show that they are similarly but never identically oriented since the diffraction intensity varies on the obtained area (Fig. 3.7). However, the pattern from D could not be unambiguously indexed so the sample

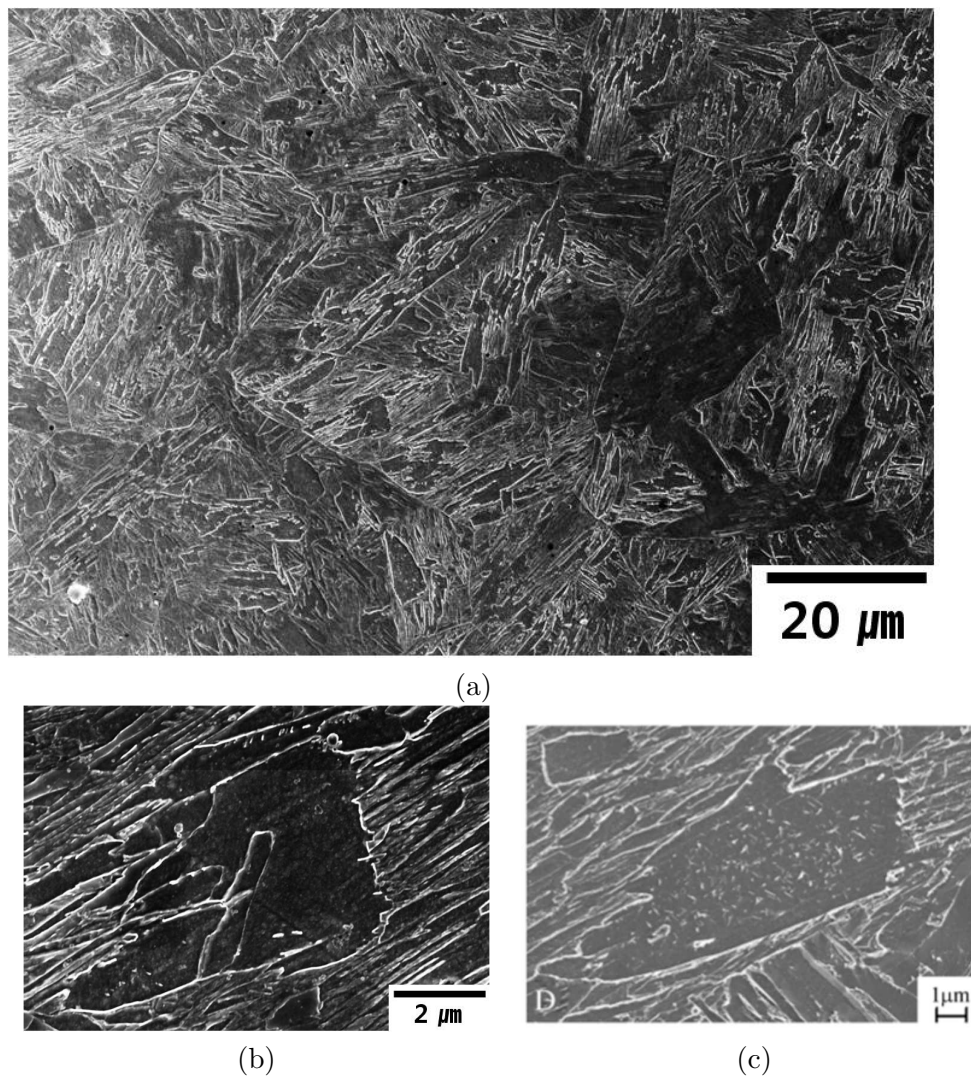


Figure 3.4: Observation using scanning electron microscopy; (a) the overall microstructure; (b) the observed coalesced structure; (c) the reported coalesced bainite (Keehan et al., 2006a).

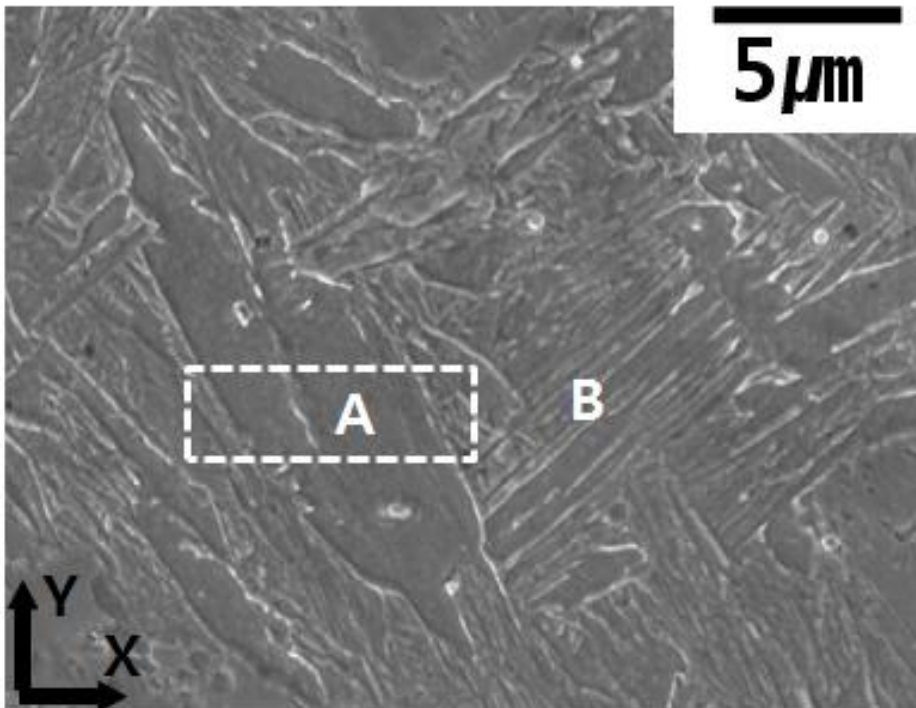


Figure 3.5: Coalesced (A) and fine martensite (B) in focused ion beam micrograph. The rectangle indicates the area from which the transmission electron microscopy sample was extracted.

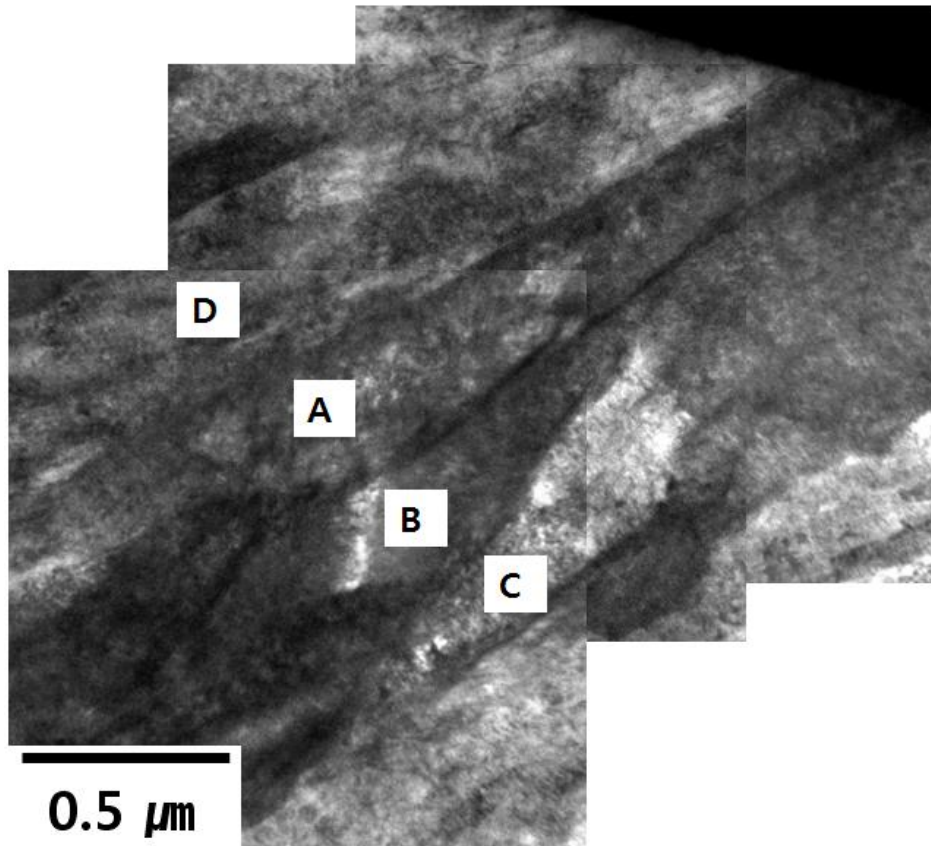


Figure 3.6: Transmission electron micrograph montage representing coalesced martensite illustrated in Fig. 3.5.

was tilted to generate the pattern in Fig. 3.8; this indicated that the relationship between A and D could be described by a rotation of 9.4° about $\langle \bar{1}10 \rangle_\alpha$ which is crystallographically equivalent to 180° about $[0.650\ 0.054\ 0.758]_\alpha$ where this axis is close to a diad. In other words, all the platelets $A - D$ which form the coalesced plate have small relative misorientations.

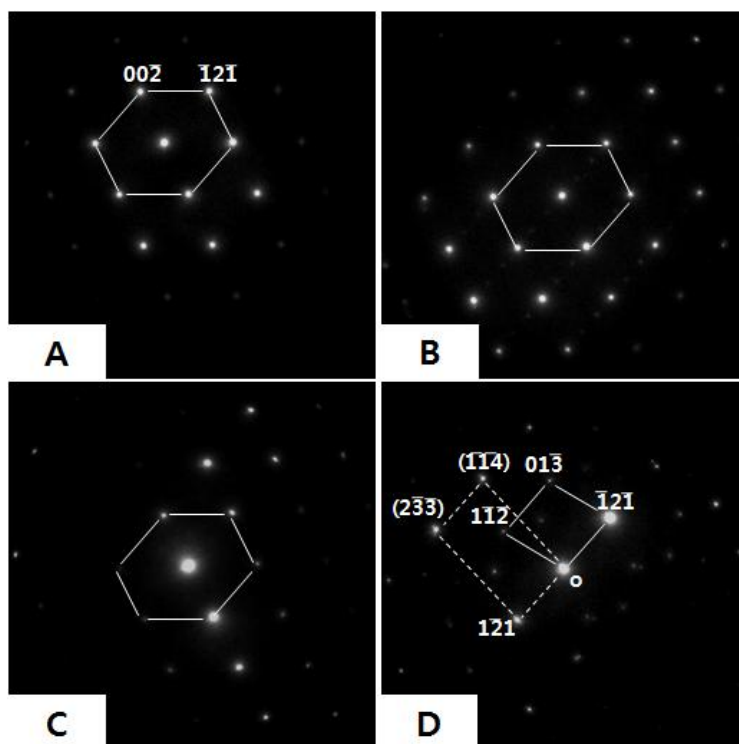


Figure 3.7: Diffraction patterns from each of the platelets marked in Fig. 3.6. A , B and C are similarly oriented but the pattern from D is ambiguous.

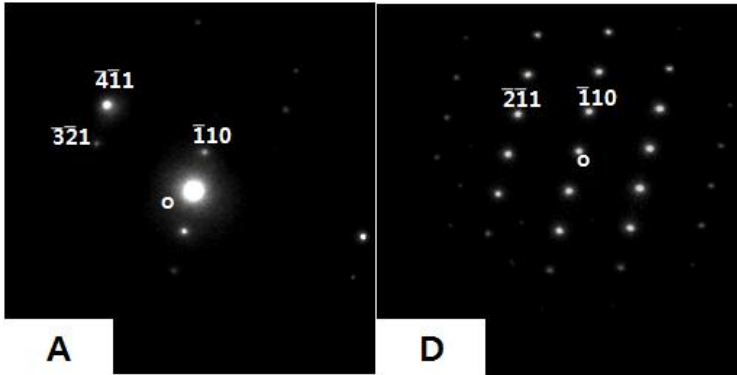


Figure 3.8: Diffraction patterns from platelets *A* and *D* marked in Fig. 3.6 after tilting relative to the patterns shown in Fig. 3.7.

3.4 Mechanism for misorientation

The shape deformation during the formation of bainite or martensite is an invariant plane strain with a large shear component, a shear strain of about 0.26 on the habit plane (Swallow and Bhadeshia, 1996). A deformation like this is difficult to sustain elastically at the high temperatures where bainite forms, because the yield strength of austenite is small at elevated temperatures. Direct observations have shown this accommodation occurs in a manner that compensates for the transformation shear (Swallow and Bhadeshia, 1996). Transmission microscopy of samples in which some austenite is preserved following the growth of bainite has at the same time shown that the plastic accommodation creates a large dislocation density in the austenite adjacent to the bainite (Bhadeshia and

Edmonds, 1979). Two things should be noticed; first, plastic accommodation can also happen even during martensitic transformation when the austenite fails to accommodate the deformation fully elastically; second, systematic plasticity of this kind may change the effective crystallographic orientation in the deformed region (Christian, 1990). In fact, Miyamoto et al. (2009) revealed that austenite adjacent to platelet of martensite as well as bainite has curved planes due to this very effect.

Therefore a mechanism was proposed to induce small misorientations between plates which in a perfect crystal of austenite would be in exactly the same crystallographic disposition in space. Fig. 3.9a illustrates the bending of glide planes caused by the presence of an *excess* density of edge dislocations with the same sign, the tilt being about an axis on the slip plane normal to the Burgers vector of magnitude \mathbf{b} . Suppose that the excess dislocation density localized into a region with width L (Fig. 3.9b); assuming a unit depth, the product ρL gives the number of dislocations per unit length and its inverse the spacing between the dislocations in the array which forms the tilt boundary. It follows that for small misorientations, θ about the line vector is given by

$$\theta = \rho b L. \quad (3.1)$$

The Burgers vector for slip in austenite is $\frac{1}{2}a_\gamma < 110 >$ so that $|\mathbf{b}| = 2.548 \text{ \AA}$ for a lattice parameter of $a_\gamma = 3.604 \text{ \AA}$. The dimension L repre-

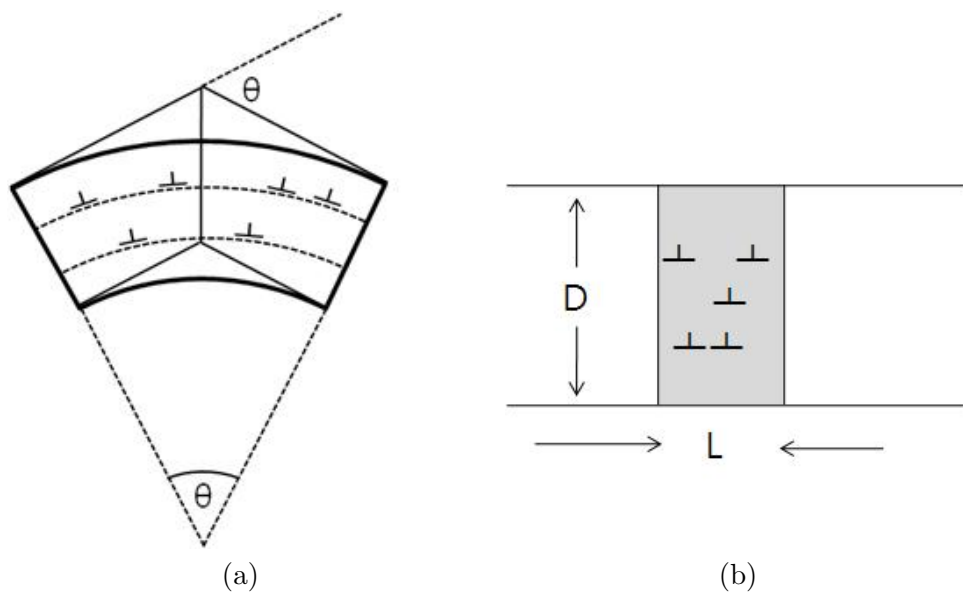


Figure 3.9: (a) Dislocations causing the development of misorientation in a single crystal. (b) Excess dislocations in the grey area, assumed to align into a column to cause a constant misorientation between the adjacent white areas.

senting the deformed austenite adjacent to the martensite plate is taken to be equal to the typical width of the plate, $0.2 \mu\text{m}$ (Swallow and Bhadeshia, 1996). Here ρ is the dislocation density. Dislocations in martensite and bainite formed at high temperatures are inherited from the austenite deformed to be compatible to the transformation strain, so the dislocation density in the product should be the same as that in the parent (Christian, 1979). The density ρ can therefore be estimated using an empirical equation available in the literature:

$$\log\left\{\frac{\rho}{\text{m}^{-2}}\right\} \simeq 9.2848 + \frac{6880}{T} - \frac{1780360}{T^2} \quad \text{for } 570 < T < 920 \text{ K} \quad (3.2)$$

where T is the absolute temperature at which the microstructure is generated. For martensite formed at the measured M_S temperature, 337°C , $\rho = 6.01 \times 10^{15} \text{ m}^{-2}$.

The shape deformation was interpreted as simple shear on $(232)_\gamma$ plane with $\langle \bar{1}01 \rangle_\gamma$ direction neglecting the smaller volume change due to transformation, where the former was obtained from the habit plane of lath bainite and the latter from its growth direction, respectively (Davenport, 1974) (Fig. 3.10). The reason to select the crystallographic orientation of lath bainite rather than that of martensite can be rationalized as follows; there is no intrinsic difference coming from growth mechanism in crystallography between martensite and bainite; the crystallography in the environment where plastic accommodation is allowed might be more

appropriate for this work according to Christian (1990).

Since austenite slips on the system consisting of close-packed planes and directions $\{111\} \langle 110 \rangle$ and the given habit plane of Fig. 3.10 is not a close-packed plane of austenite, it requires a combination of slip systems to accommodate the transformation shear. Using well-established Taylor theory for the operation of multiple slip systems to account for an arbitrary plastic deformation (Lee, 2006), it was found that the simultaneous operation of the slip systems $(111)[\bar{1}01]$ and $(\bar{1}\bar{1}1)[10\bar{1}]$ with the shear strain due to the former being five times that of the latter, can accommodate the corresponding shape deformation. The details are described in Appendix B and C.

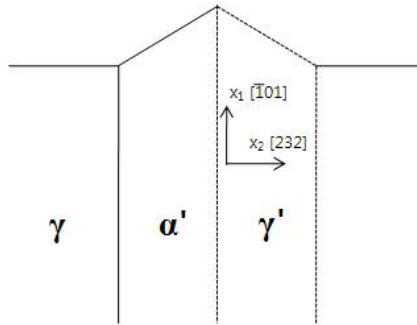


Figure 3.10: Plastic accommodation in the austenite. The region enclosed by the dashed lines represents deformed austenite (γ'), the upheaval being caused by the shape deformation accompanying the growth of martensite (α').

Since Eq. 3.2 gives the total dislocation density (ρ) rather than the *ex-*cess density which is not known, the latter was assumed to be a fraction ϕ

of the former. It has already been explained that the distribution of dislocations activating a slip can cause the lattice rotation (Fig. 3.9a). The rotation can be described mathematically in matrix form, where each component contains the information on the rotation axis and angle (Bhadeshia, 1987). They correspond to the axis perpendicular to both the slip plane normal and slip direction, and the value of Eq. 3.1, respectively. The rotation by the multiple slip is represented by the product of each rotation matrix, where even a single slip can be divided into several steps interrupted by others. Considering that the total rotation depends on the rotation sequence, four combinations of rotations with three ϕ values were calculated as listed in Table 3.1. The results show that the magnitudes of the rotations are proportional to the *excess* density and the rotation axis varies with the rotation sequence as expected. It is interesting that the rotation axes listed are all approximately parallel to $[\bar{1}\bar{1}\bar{1}]_\gamma$, which corresponds to $[101]_\alpha$, given the orientation relationship between martensite and austenite. $[101]_\alpha$ is of course the diad derived previously. Nevertheless, the results of Table 3.1 cannot be directly compared with that calculated from the diffraction data of Fig. 3.8 because of following; first, the selection of slip systems was conducted based on the literature data (Fig. 3.10), not the actual data of habit plane and shear direction which cannot be obtained from Fig. 3.6 to 3.8 of thin foil studies; second, the axis-angle pair calculated from Fig. 3.8 is ambiguous due to the absence of information about the rotation axis; third, the calculated rotation de-

depends on the density of *excess* dislocations, which should be determined by experiments.

Table 3.1: Rotation axis and angle derived from the operation slip systems $a \equiv (111)[\bar{1}01]$ and $b \equiv (1\bar{1}1)[10\bar{1}]$. R represents the rotation operation with the sequence of operation from right to left. All of the stated indices are with respect to austenite.

ϕ	$R_b R_a$	$\frac{1}{2}R_b \frac{1}{2}R_a \frac{1}{2}R_b \frac{1}{2}R_a$	$\frac{1}{2}R_a \frac{1}{2}R_b \frac{1}{2}R_a \frac{1}{2}R_b$	$R_a R_b$
0.25	3.48°	3.48°	3.48°	3.48°
	$[\overline{0.519} \ 0.686 \ \overline{0.510}]$	$[\overline{0.517} \ 0.686 \ \overline{0.512}]$	$[\overline{0.512} \ 0.686 \ \overline{0.517}]$	$[\overline{0.510} \ 0.686 \ \overline{0.519}]$
0.50	6.96°	6.96°	6.96°	6.96°
	$[\overline{0.523} \ 0.686 \ \overline{0.505}]$	$[\overline{0.519} \ 0.686 \ \overline{0.510}]$	$[\overline{0.510} \ 0.686 \ \overline{0.519}]$	$[\overline{0.505} \ 0.686 \ \overline{0.523}]$
0.75	10.44°	10.44°	10.44°	10.44°
	$[\overline{0.528} \ 0.686 \ \overline{0.501}]$	$[\overline{0.521} \ 0.686 \ \overline{0.508}]$	$[\overline{0.508} \ 0.686 \ \overline{0.521}]$	$[\overline{0.501} \ 0.686 \ \overline{0.528}]$

3.5 Conclusions

It has been shown that the large plates of martensite retain vestiges of the origins of individual platelets, which are clear visible boundaries between the individual platelets which participated in the coalescence. This proves that the gross structure was formed by the coalescence of martensite platelets, not the coarsening of a single plate. The coalesced platelets are not precisely identically oriented in space but slightly misoriented. The rotations are explained on the basis that the shape deformation accompanying the formation of a martensite plate causes plastic strain in the

adjacent austenite. This in turn changes the crystallographic orientation of the adjacent austenite, so that a new plate of martensite which grows from this deformed austenite will be slightly rotated relative to the original platelet. An estimate of the degree of resulting rotation gives reasonable numbers although it has not been possible to attain a quantitative comparison with experimental observations because the latter are incomplete due to the fine scale of the structure and because of the absence of austenite. A complete closure with theory would require the three dimensional crystallography (habit plane, shape deformation and orientation relationship) to be characterized.

Chapter 4

Effect of external force on coalescence

4.1 Introduction

Considering that the coalescence of adjacent platelets is a localized incident, its formation mechanism in martensite is imagined not to differ from that in bainite. In chapter 2, it was stated that two factors possibly control the coalescence of platelets; strain energy and carbon partitioning. The first parameter is essential to relate the coalescence with transformation mechanism since it dominates the growth of bainite or martensite based on thermodynamics. Another is, on the other hand, difficult to incorporate into the transformation mechanism itself since it is usually treated as separate phenomenon involved with martensite or bainite transformations.

In this chapter, two specific situations were designed, where the associated strain energy can be affected, to examine the behaviour of coalescence; martensite transformation near to free surface and bainite transformation with applied stress. They will be approached in terms of strain energy relaxation and variant-selection, respectively.

4.2 Experimental method

Two different experiments were conducted using Alloys A and D in the previous chapter; confocal laser scanning microscopy and thermo-mechanical simulation, respectively.

Confocal laser scanning microscopy (CLSM) was used to observe the martensite transformation in the vicinity of the free surface. The austenitization was carried out at 1250 °C for 3 min, which is consistent with the dilatometry reported in chapter 2. The method enables the surface relief effect due to phase transformation to be detected, even at high temperatures where thermal fluctuation can be problematic in other microscopy techniques (Komizo et al., 2008). The specimens for CLSM were machined into ≈ 2 mm cubes. The details about the equipment are described elsewhere (Chikama et al., 1996).

In confocal laser scanning microscopy, the sensed temperature which controls the heat treatment differs from that of the specimen surface due to the heat transfer through the body of the alumina crucible on which

the specimen is located, and the specimen itself. All the temperatures recorded during confocal microscopy as reported here, are consequently corrected by calibration. The calibration was carried out by fixing a thermocouple to the top surface of the specimen and comparing against the sensed-temperature of the confocal microscope furnace (Fig. 4.1).

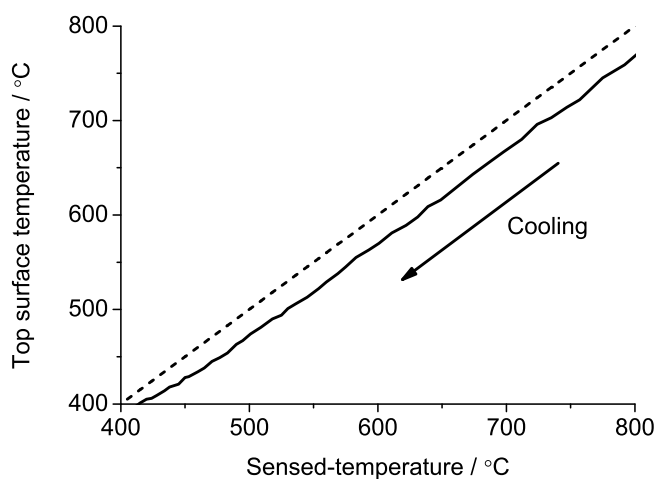


Figure 4.1: Data curve used for calibration of temperature. Notice the dashed line represents sensed-temperatures.

The severe problem of surface oxidation was avoided by maintaining an argon/helium atmosphere in the furnace, containing 2% hydrogen gas; titanium particles were also arranged around the specimen to induce cathodic protection.

The thermo-mechanical simulation was conducted using a Gleeble 3500 system and specimens were manufacture as described in Fig. 4.2. A tensile

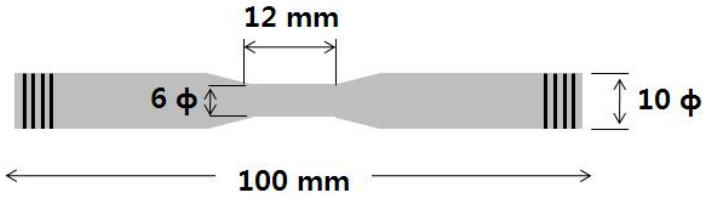


Figure 4.2: Schematic illustration of the specimen used in Gleeble 3500. Both ends of the specimen was screwed.

stress with 50 MPa was imposed on the specimen during isothermal bainite transformation at 455°C for 20 minutes. The stress level was supposed to be lower than the yield stress (64 MPa) of the austenite as predicted by an empirical equation (Young and Bhadeshia, 1994). Electron backscattered diffraction data were analysed to find evidence for variant selection.

Scanning electron microscopy was carried out as described in the previous chapter.

4.3 Results

4.3.1 Martensite near to free surface

Confocal laser scanning microscopy

One example of the surface relief observed during the transformation is illustrated in Fig. 4.3. The arrow indicates the initiation of transformation. This gives a start-temperature as $452 \pm 10^{\circ}\text{C}$, where the error is

estimated from experiments repeated five times.

Electron microscopy

In Fig. 4.4, the microstructure produced by confocal microscopy was compared that of the martensite produced by dilatometry. Notice that the microstructure of the CLSM sample represents the cross section of the top and bottom edges. It is odd that a typical lath-like structure of martensite is not observed near the top surface. On the other hand, the structure near the bottom surface corresponds typically to that of martensite from dilatometry in Chapter 2.

There was a tendency for martensite platelets formed near to the free surface to coalesce and more interestingly their growth directions deviated toward the free surface normal as they approached to the free surface (Fig. 4.5).

4.3.2 Bainite formed under the effect of uniaxial tension

Thermo-mechanical simulation

Fig. 4.6 shows the variation of the imposed stress and temperature during bainite transformation in the Gleeble machine. There were considerable fluctuations for both stress and temperature; the former might be due to the transformation strain, which disturbs the stress state; the latter is unusual. Since the scattered temperatures are covered by the M_S

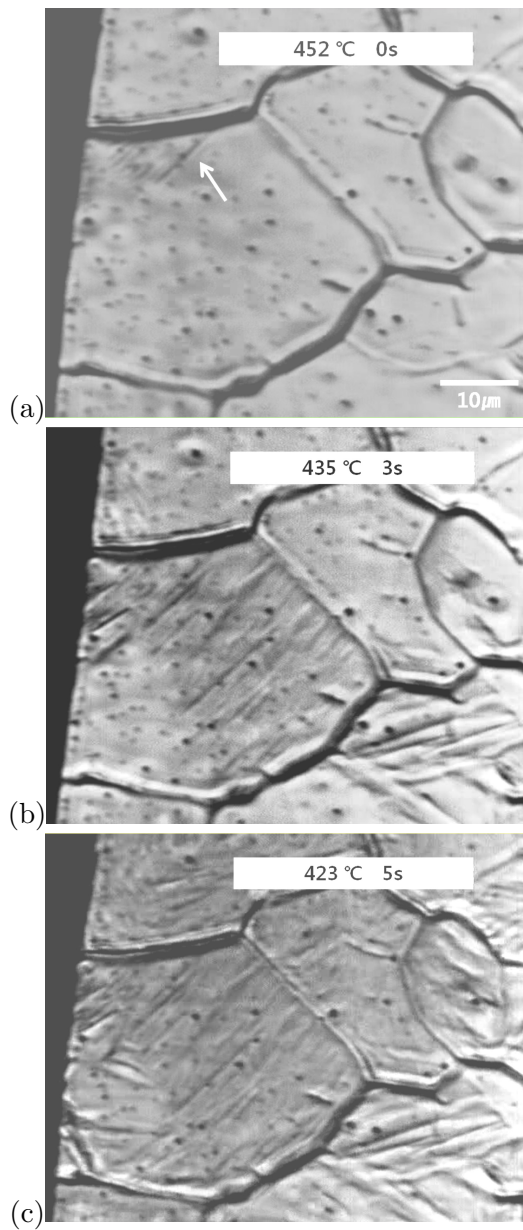


Figure 4.3: The surface relief that indicates phase transformation of austenite, as observed during confocal laser scanning microscopy.

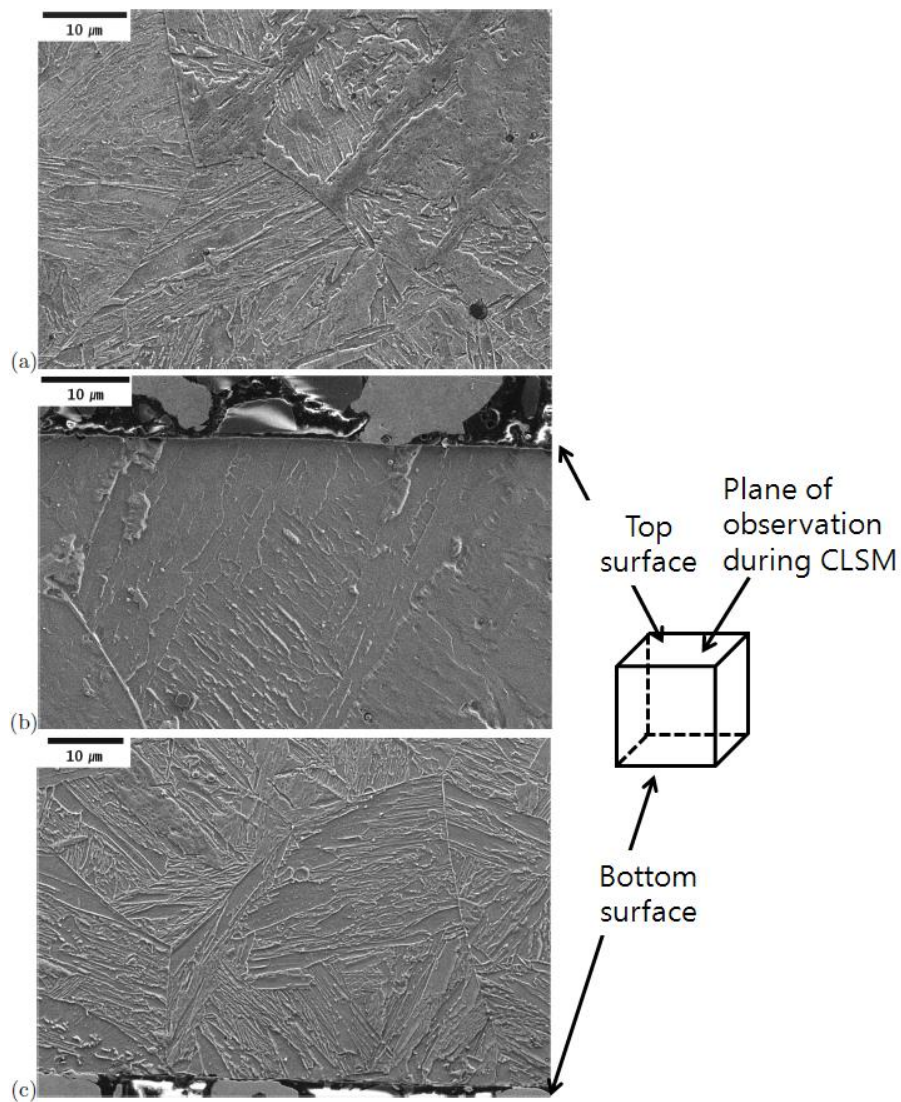
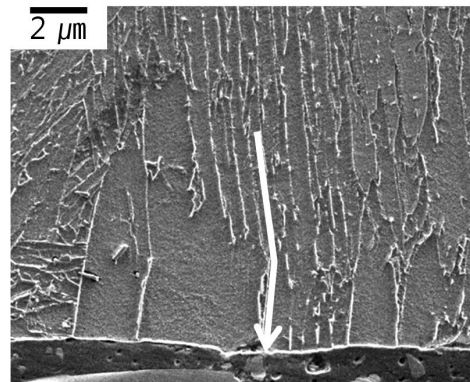
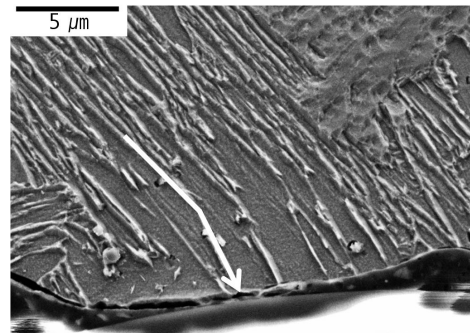


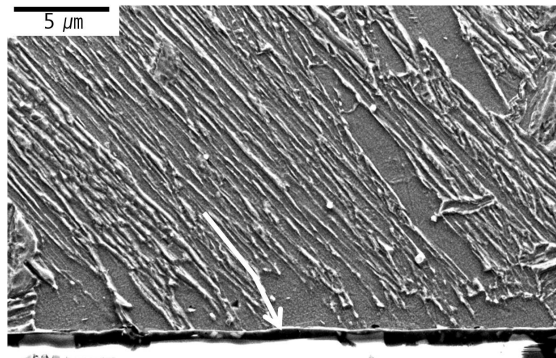
Figure 4.4: Microstructure generated in a sample from (a) dilatometry; (b, c) confocal microscopy.



(a)



(b)



(c)

Figure 4.5: Coalesced martensite formed just below free surface. The arrows represent the deviation of the growth direction.

temperature of the alloy ($452 \pm 9^\circ\text{C}$), it was assumed that the expected bainite transformation was carried out.

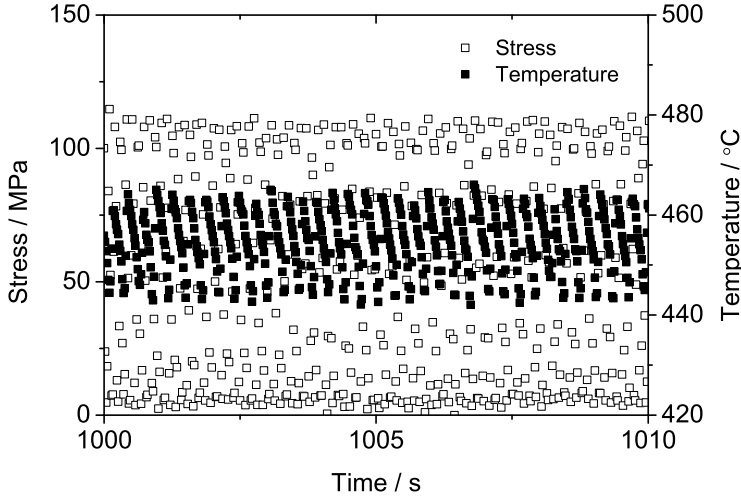
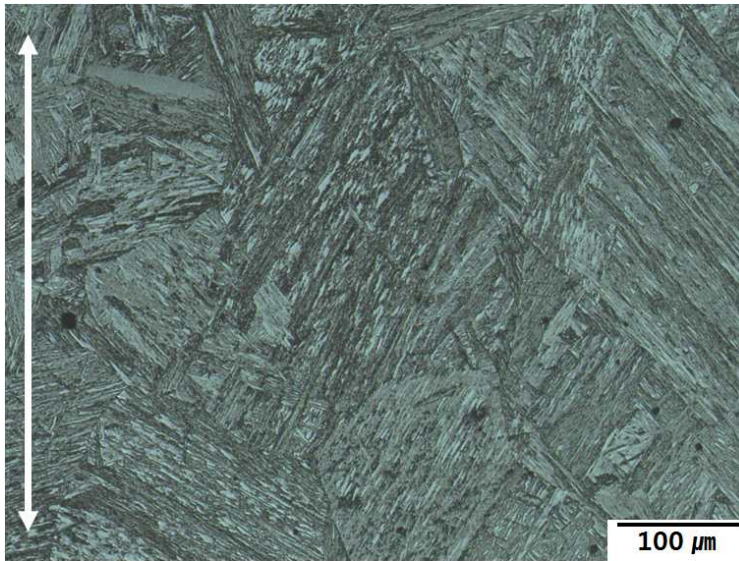


Figure 4.6: Temperature and tensile stress recorded during the thermo-mechanical simulation. The data corresponding to only early 10 seconds are presented.

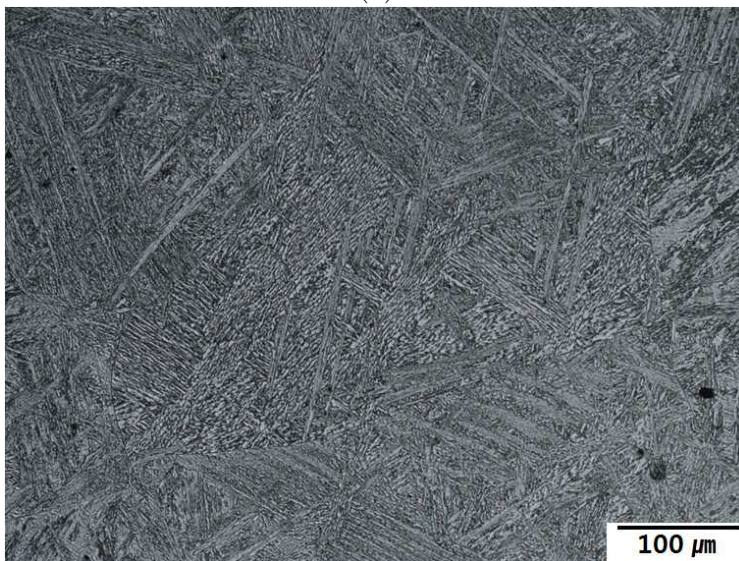
Microscopy

The bainitic structure formed under the effect of the stress was compared with that formed without the influence of stress. In optical microscopy, the overall structure of the former seems to develop as maintaining consistent direction in individual austenite grains compared to that of the latter (Fig. 4.7).

Using scanning electron microscopy, it was found that the stress imposed



(a)



(b)

Figure 4.7: Bainitic structure formed (a) under the influence of stress with direction indicated by an extended arrow and (b) without stress.

during the bainite transformation induced the coalescence in the bainitic structure (Fig. 4.8).

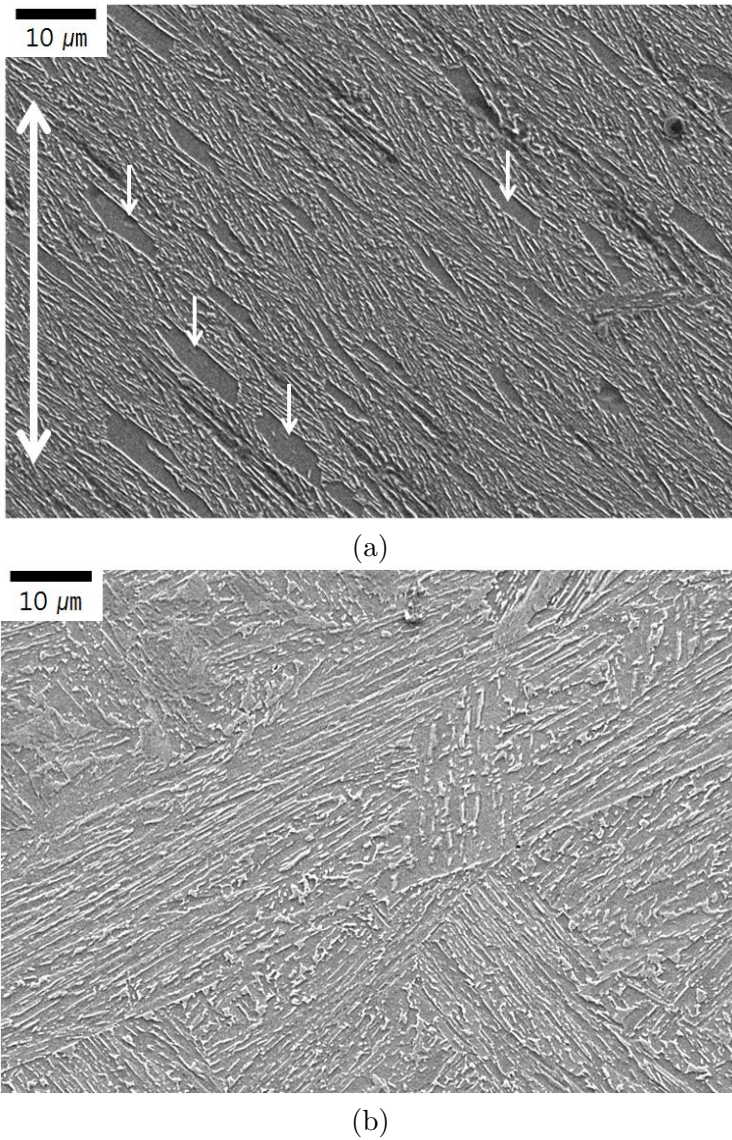


Figure 4.8: Bainitic structure formed (a) under the influence of stress with direction indicated by an extended arrow and (b) without stress. The short arrows indicate coalesced regions of bainite.

4.4 Discussion

4.4.1 Effect of free surface

Fig. 4.9 shows the change of chemical free energy of Alloy A when it transforms from austenite to ferrite during cooling without any change in composition. It is evident that the transformation observed at the top surface commenced at the temperature higher even than the bainite-start temperature of the alloy, therefore, requires less driving force.

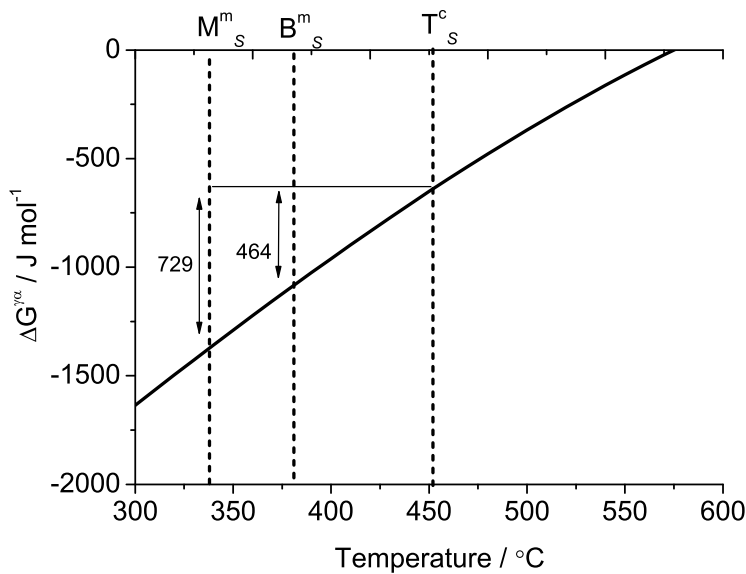


Figure 4.9: The chemical free energy change when austenite transforms into ferrite without any change in chemical composition as a function of temperature for Alloy A. M_s^m and B_s^m represent the martensite and bainite-start temperatures measured using dilatometry and T_s^c the transformation start temperature at the surface using confocal microscopy, respectively.

The origin of the smaller driving force is attributed to the relaxation of the shape deformation near to the free surface. The shape deformation due to martensitic transformation in steel is dominated by a shear on the habit plane and is analogous to the shear caused by an edge dislocation as it glide on its slip plane. This analogy may be used to investigate the relief of the elastic strains as a function of orientation relative to a free surface. The Burgers vector of the dislocation was assumed to be parallel or normal to the free surface in order to examine the most favourable orientation that a martensite plate can adopt relative to the surface.

The stress field caused by the dislocation was obtained from the work of Head (1953). This was substituted in the following equation for the strain energy per unit length of the dislocation (Hirth and Lothe, 1992):

$$\frac{W}{L} = \int_{r_0}^R r dr \int_0^{2\pi} \left[\frac{1}{2\mu} \sigma_{xy}^2 + \frac{1}{2E} (\sigma_{xx}^2 + \sigma_{yy}^2 + 2\nu\sigma_{xx}\sigma_{yy} - \sigma_{zz}^2) \right] d\theta$$

where σ_{ij} is a stress component defined in Hirth and Lothe (1992); E , μ and ν are Young's modulus, shear modulus and Poisson's ratio (taken to be 0.25), respectively. The terms r_0 and R are the length scales over which the energy density was to be integrated; r_0 was taken to be 4.5 times of the magnitude of the Burgers vector for a $\frac{1}{2}[110]$ dislocation on a $\{111\}$ plane in austenite (Hirth and Lothe, 1992) and $R = 5$ nm, which is a small enough value to show the characteristic behaviour. The dislocation core energy was neglected in the calculations due to its negligible contribution

(Hirth and Lothe, 1992). As expected, the calculations indicate that the strain energy of the dislocation decreases significantly as it approaches the surface (Fig. 4.10). It also shows that the effect of the orientation of the Burgers vector becomes negligible when the dislocation lies deep within the material.

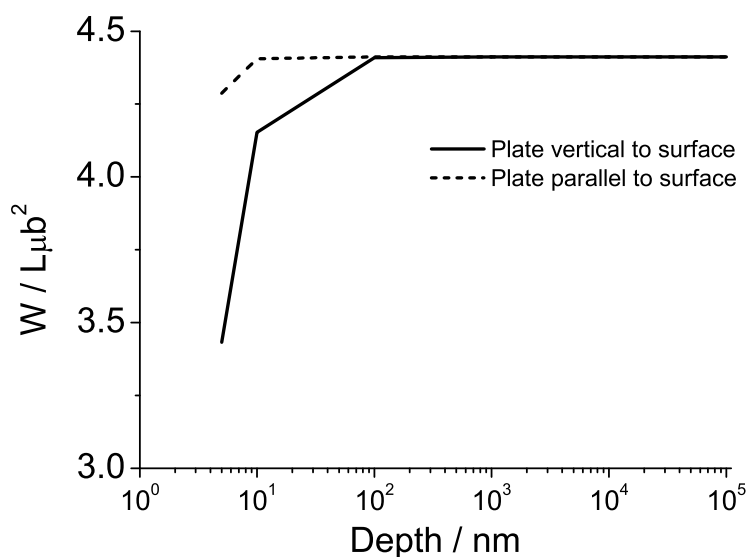


Figure 4.10: The variation of the strain energy due to an edge dislocation as a function of the distance from the surface. Solid and dotted lines correspond to the martensite plate which is vertical or parallel to free surface, respectively.

It is interesting that the degree of strain relaxation is much stronger for the dislocation related to the plate vertical to the free surface, which is consistent with the observation in Figs. 4.5 and 4.11, supporting the idea that the coalescence is governed by strain relaxation.

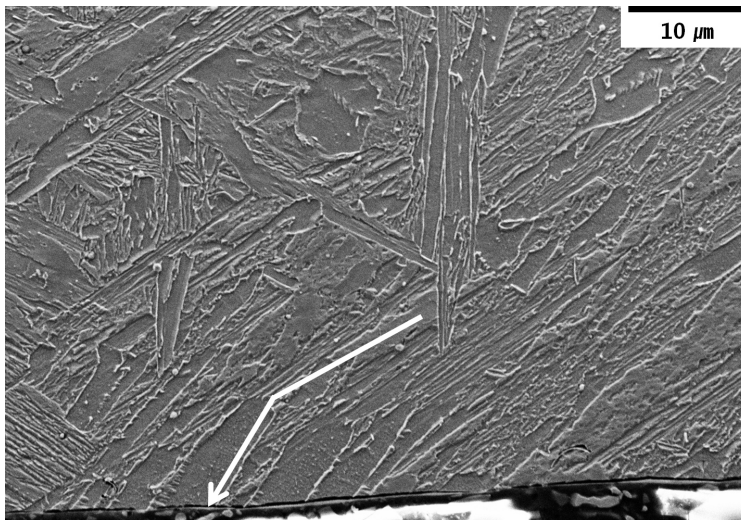
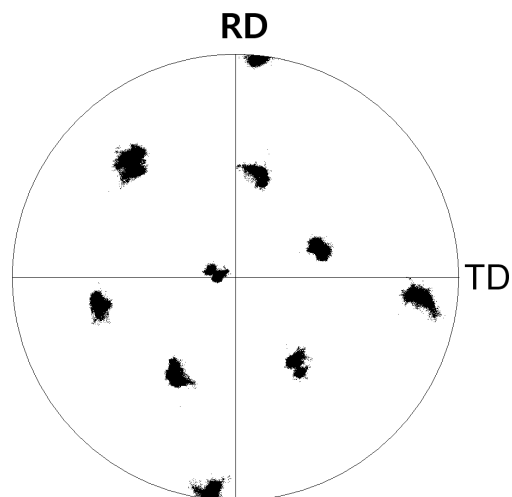


Figure 4.11: Coalesced martensite formed just below free surface. The shape deformation direction of coalesced martensite deviated toward the free surface normal.

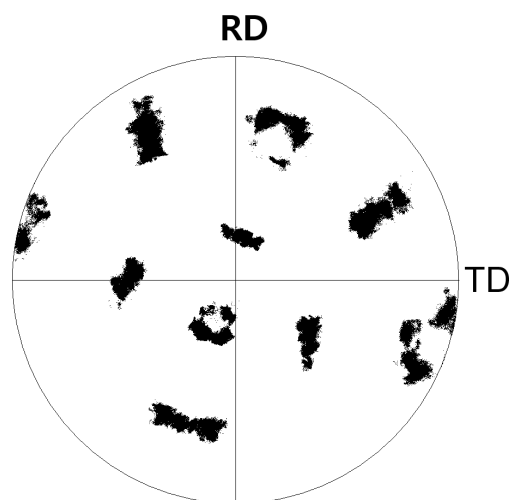
4.4.2 Effects of stress

It was found that the applied stress interrupted the bainite transformation in a way to limit the variety of orientations for bainitic ferrite in Fig. 4.12, where $\{001\}$ pole of bainitic ferrites in a single austenite with the area of $100 \times 100 \mu\text{m}^2$ was examined for bainitic structure formed with applied stress and without stress. Considering that the coalescence can occur only among the bainitic ferrites with the identical orientation, reducing the number of orientations from the 24 possibles on a random basis can promote the coalescence by inducing higher probability of growing parallel plates.

Coalesced bainites in image quality (IQ) mapping are displayed more brightly due to the absence of heterogeneous strains caused by interface structure within them (Fig. 4.13). Therefore the orientations corresponding to the coalesced regions were traced as shown in Fig. 4.14. The result shows that there is a hierarchical selection for coalescence even in the bainitic ferrites survived by the bias. It might reflect that the applied stress is involved in coalescence process with a more direct way.



(a)



(b)

Figure 4.12: $\{001\}$ Pole figure showing the orientations of bainitic ferrite formed (a) with the applied stress and (b) without stress, where RD represents the tensile direction.

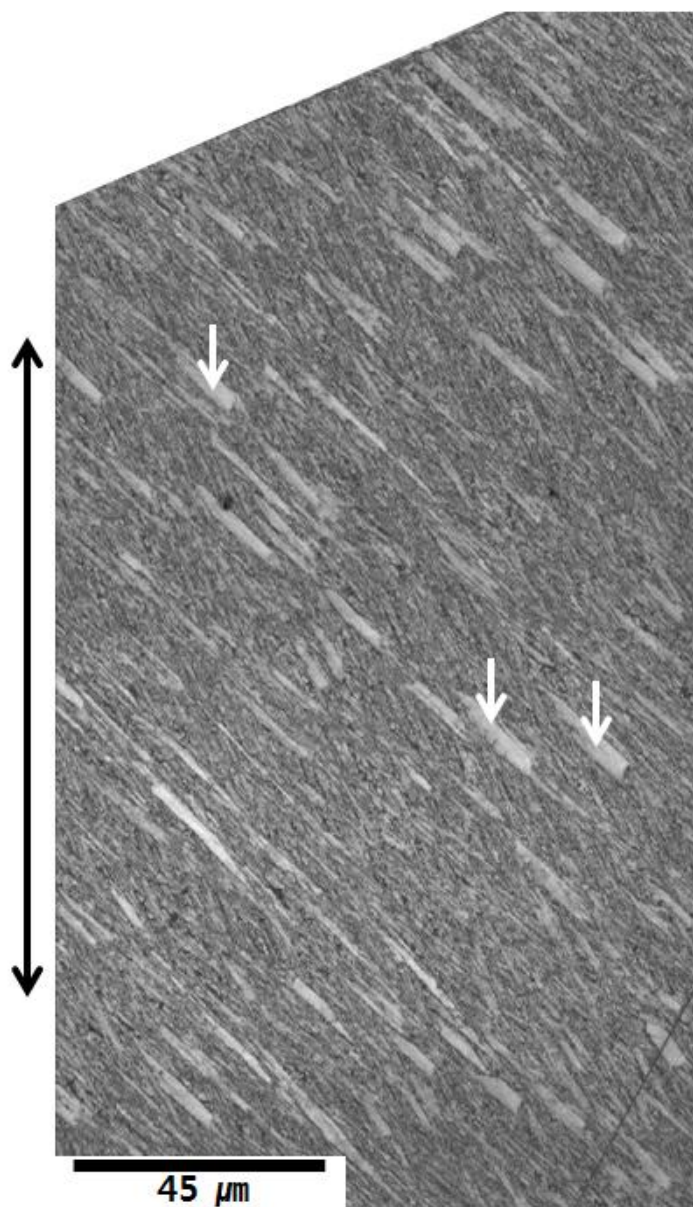


Figure 4.13: Image quality mapping of the bainitic structure formed under the effect of tension stress. Coalesced bainite was indicated by a arrow and the extended arrow represent the tensile axis.

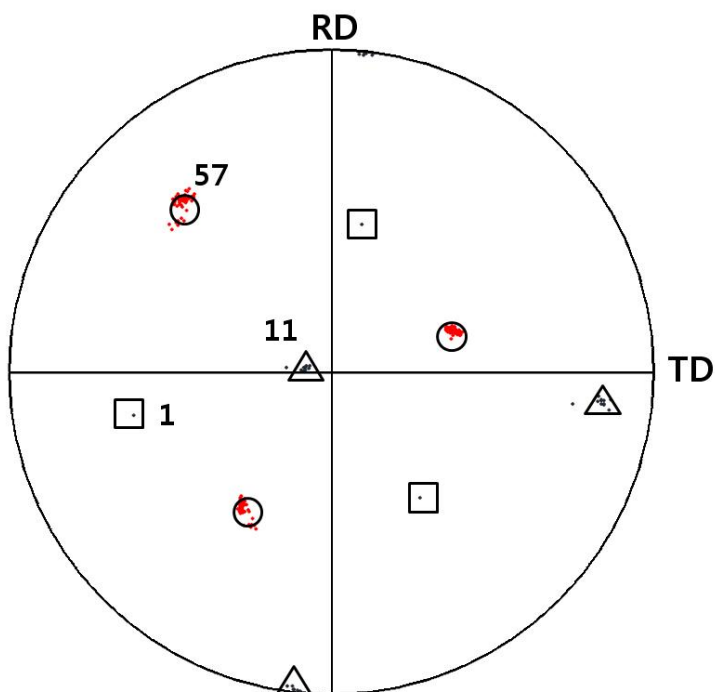


Figure 4.14: $\{001\}$ Pole figure showing the orientations of coalesced bainite regions, where RD represents the tensile direction. The poles represented by circles, triangles and squares are close to the three variations based on a Bain model.

Then the mechanical driving force (ΔG_{MECH}) induced from uniaxial tensile stress (σ) can be estimated by the following equation developed by Patel and Cohen (1953):

$$\Delta G_{MECH} = \frac{1}{2}s\sigma \sin 2\theta + \frac{1}{2}\delta\sigma(1 + \cos 2\theta)$$

where s and δ are shear and dilatation strain for invariant plane strain of bainite transformation; θ is the angle between the tension axis and the normal to habit plane. Here maximum ΔG_{MECH} is obtained when $\tan 2\theta = s/\delta$, which leads to $\theta = 41^\circ$ (Patel and Cohen, 1953) assuming s and δ are 0.22 and 0.03, respectively (Bhadeshia, 2001). A calculation using $\sigma = 50$ MPa estimated $\Delta G_{MECH} \approx 42 \text{ J mol}^{-1}$. Notice that this is comparable to 70 J mol^{-1} , which was critical to induce the coalescence in bainite for Alloy C in chapter 2. This analysis demonstrates that the forced stress caused the coalescence of bainitic ferrites with a specific variant by aiding the mechanical driving force, which corresponds to a variant selection.

4.5 Conclusions

It was found that the coalescence in martensitic and bainitic structures is affected by the proximity of a free surface and by externally applied uniaxial tension.

Martensite forming near to the free surface tended to coalesce and at the same time, the growth direction of platelets deviated toward the normal to the free surface. This is exactly consistent with a maximum relief of strain energy. It also proves that the coalescence is governed by the mode of strain energy relaxation.

Isothermal transformation combined with a uniaxial tension caused a coalescence in bainitic ferrites, which never occurred in a identical simple isothermal process. It was found that the forced stress stimulated the coalescence of bainitic ferrites with a specific variant by aiding the mechanical driving force.

Chapter 5

Prevention of coalescence

5.1 Introduction

The work described in this chapter aims to find a method to block the coalescence process which leads to the formation of coarse aggregated identically oriented plates. The key requirements for coalescence to occur have been listed as follows (Chang and Bhadeshia, 1996):

- (i) there must be sufficient driving force to sustain the larger strain energy associated with thicker plates;
- (ii) there should be nothing to stifle the growth of individual platelets since coalescence evolves gradually as the platelets merge.

There has been little work in general, on how to disrupt the formation of coarse crystallographic domains, and certainly none on the prevention

of the plate coalescence process just described. It is the second of the conditions listed above that the work presented here was set to exploit in order to develop a new method to hinder coalescence. Fine compositional perturbations are introduced into the austenite prior to its transformation, so as to prevent the merging of plates. As will be seen later, this has been achieved by heat-treatment in a two-phase field prior to full austenitisation and subsequent transformation. Although such a technique may not be cost-effective in general, it can in principle be implemented during multipass welding where the deposition of a new layer induces the heat treatment of the underlying material.

5.2 Experimental method

Alloy A listed in Table 5.1 was selected because of its propensity to form coalesced bainite.

Table 5.1: Chemical composition of the alloy (wt%)

C	Si	Mn	Cr	Ni	Mo
0.03	0.23	2.05	0.43	7.1	0.63

The specimens were heat-treated using dilatometry. Microscopy with the consistent way in the previous chapters was conducted on them. For the purposes of electron backscattered diffraction, the final stages of sample preparation involved delicate polishing using colloidal silica. Trans-

mission electron microscopy and its scanning variant were used for energy dispersive spectrometry on specimens detached using the focused ion beam technique.

5.3 Results and discussion

5.3.1 Method

When a steel is annealed within the two-phase austenite (γ) and ferrite (α) field, austenite stabilising substitutional solutes such as manganese and nickel will tend to partition preferentially into γ . The tendency for such redistribution is defined by the equilibrium phase diagram. If a fully martensitic sample is annealed in this way, then small regions of solute-enriched austenite regions will form between the plates. With prolonged annealing, the composition and phase fractions of austenite and ferrite will reach equilibrium. A subsequent, short heat treatment in the single γ phase field can be designed so that the ferrite is eliminated but the non-uniform distribution of solute remains on a fine scale consistent with the original films of austenite generated at the intercritical annealing treatment.

The process is illustrated schematically in Fig. 5.1; chemically heterogeneous austenite is first created by intercritical annealing, to be followed by transformation into bainite. The regions rich in austenite are slow to transform and hence disrupt the growth of bainite originating from

the solute-depleted austenite, thereby preventing coalescence of parallel plates.

5.3.2 Design of Heat Treatment

Calculations were carried out on the equilibrium phase fractions of austenite and ferrite in the steel listed in Table 5.1 as a function of temperature, using *Thermo-Calc* version S, as illustrated in Fig. 5.2; the plot deals with only austenite and ferrite because cementite is not a stable phase above 576 °C. As is evident, the extent to which the partitioning of solutes occurs increases as the temperature is reduced, consistent also with the decrease in the equilibrium fraction of austenite. Hence, the intercritical annealing temperature was chosen as 580 °C (step b in Fig. 5.1).

The program *DICTRA* version 25 was used to assess the time required to achieve sufficient partitioning during intercritical annealing. Two simulations were conducted, the first where the austenite initially has the chemical composition of the alloy, *i.e.*, it originates from the austenite that is retained when the steel is quenched to martensite. The second represents approximately the case where the calculation assumes local equilibrium at the interface between austenite and ferrite at the annealing temperature.

The kinetics of the partitioning of solutes through successive heat treatments was simulated using *DICTRA* version 25 considering only carbon,

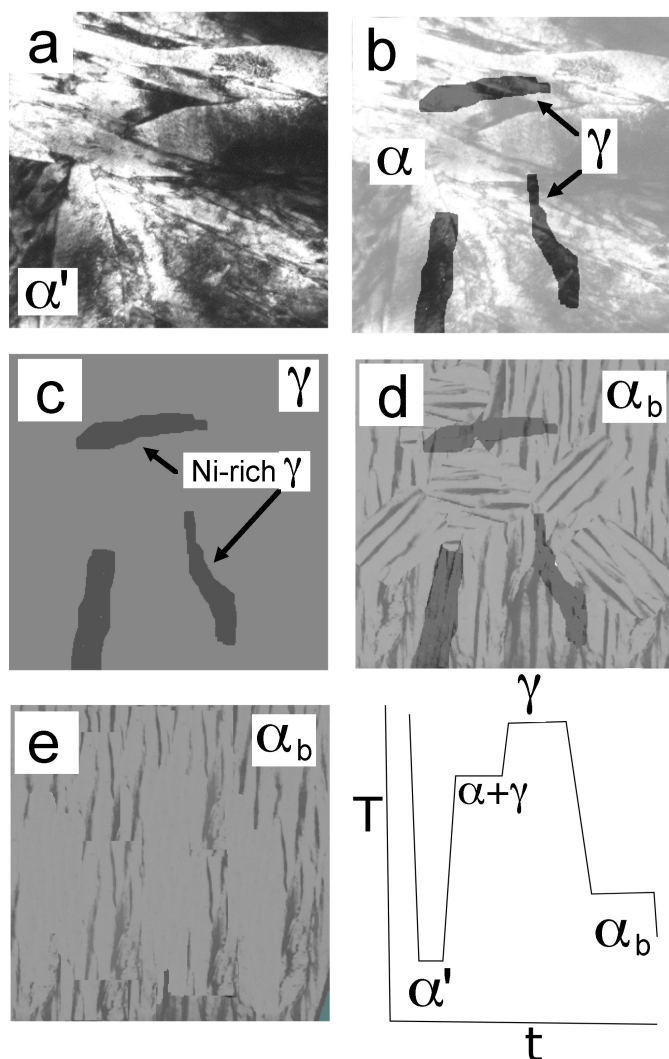
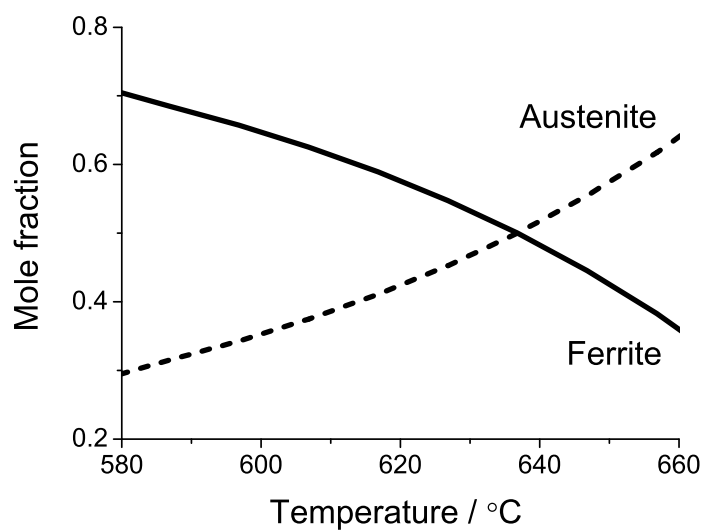
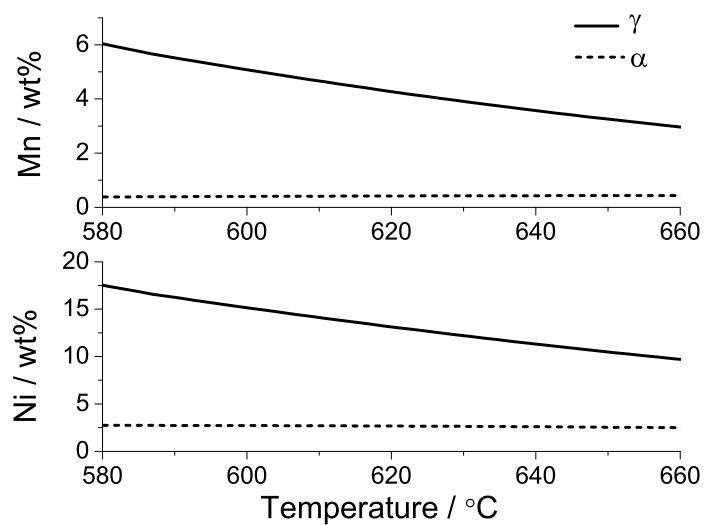


Figure 5.1: **Schematic** illustration of the method used to reduce the crystallographic grain size, beginning with (a) α' martensite; (b) intercritical annealing to produce small regions of enriched-austenite γ and α tempered martensite; (c) short treatment to eliminate α but leave the austenite compositionally modulated; (d) isothermal transformation of heterogeneous γ to many orientations of α_b bainite; (e) bainite from homogeneous austenite, with a bimodal distribution consisting of coalesced and fine plates.



(a)



(b)

Figure 5.2: (a) Equilibrium fractions of austenite and ferrite as a function of the temperature; (b) equilibrium chemical compositions of stable phases.

manganese and nickel as the diffusing species; the latter two were selected because they are present in significant concentrations. The calculations assumed as the starting state, the existence of a thin layer ($0.01\ \mu\text{m}$) of austenite of the appropriate chemical compositions, attached to a $0.1\ \mu\text{m}$ layer of ferrite. The volume fraction of austenite at the beginning is therefore less than equilibrium fraction at the chosen intercritical annealing temperature of $590\ ^\circ\text{C}$ for the purposes of simulation. Notice that this is $10\ ^\circ\text{C}$ greater than the $580\ ^\circ\text{C}$ used in the experiments because a specific numerical issue with *DICTRA* which meant that the amount of nickel had to be adjusted slightly in order to avoid numerical instability for the $580\ ^\circ\text{C}$ calculation (Bratberg, 2011). It turns out that there is not much of a difference in the *DICTRA* output for the accurate calculation for $590\ ^\circ\text{C}$ and approximate analysis for the $580\ ^\circ\text{C}$ case, as illustrated in Fig. 5.3.

The next stage of the heat treatment was to fully austenitise the chemically-heterogeneous structure produced during intercritical annealing, in such a way that the heterogeneity is essentially preserved. The measured A_{c3} temperature of the alloy at a heating rate of $50\ ^\circ\text{C s}^{-1}$ was found to be $742 \pm 0.5\ ^\circ\text{C}$; the heating rate has to be high in order to avoid the substantial diffusion of substitutional solutes during heating. The austenitisation condition was set as $780\ ^\circ\text{C}$ for 10 min because *DICTRA* simulation indicated that although diffusion is inevitable, the solute rich regions persist, as illustrated in Fig. 5.4. The simulation was conducted assuming a region of austenite enriched by intercritical annealing to a thickness of 8 nm and

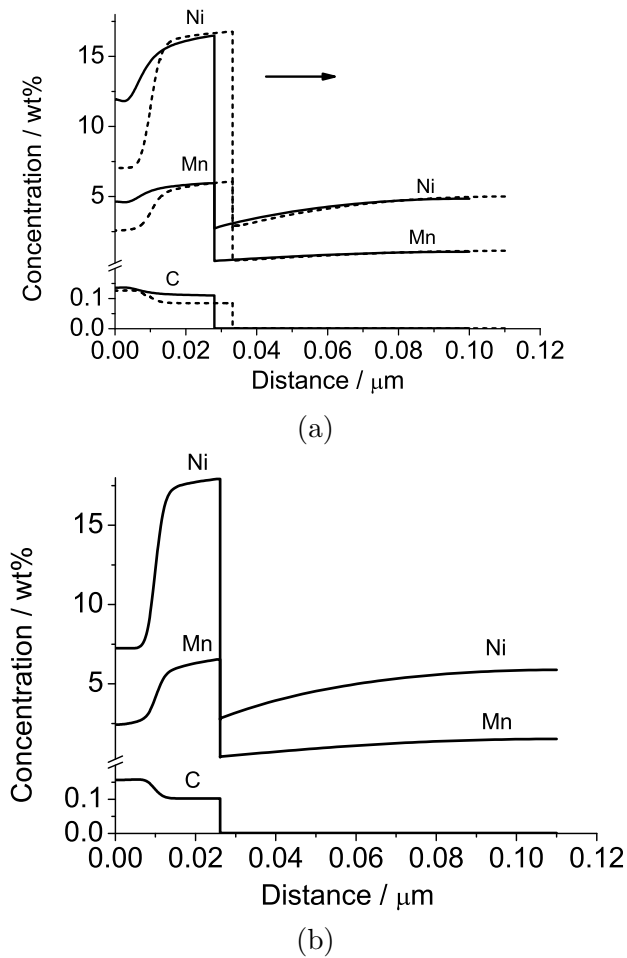


Figure 5.3: *DICTRA* simulations of solute partitioning during austenite growth over a period of 5 h. (a) 590 °C with the dashed line for austenite with a starting composition identical to that of the alloy, and the continuous line assuming that the austenite formed at 590 °C and hence has the equilibrium composition for that temperature. The arrow indicates the growth direction of the austenite. (b) 580 °C assuming that the starting austenite has the average composition of the alloy.

composition 5.8Mn–16.2Ni wt%; the corresponding composition of ferrite was set at 1.1Mn–5.0Ni wt%, consistent with the profile presented in Fig. 5.3; the approximation here is that any gradient within the 8 nm thick austenite is neglected at the point where the simulation begins. There are small variations in the carbon concentration as a function of distance, but this is not because of a lack of atomic mobility, but rather that the chemical potential of carbon is homogenised in the presence of variations in the manganese and nickel concentrations.

5.3.3 Dilatometry

Using the information from the simulations, three different heat treatments were conducted in a dilatometer (Fig. 5.5). Two of these are from homogeneous austenite to obtain martensite or bainite, and the third to obtain bainite from heterogeneous austenite; the latter is for convenience, designated α_b^h in all subsequent discussion. The results are shown in Fig. 5.6, which reveal that some martensite was also obtained after the isothermal heat treatment to generate α_b and α_b^h .

The strain change due to austenite formation during intercritical annealing at 580 °C was found to be 0.0004, which compares with the strain of 0.0056 for full austenitisation at that temperature as judged from the first heat-treatment illustrated in Fig. 5.7. Thus, the fraction of austenite formed during annealing is estimated to be 0.07, although the total may be greater if the sample contained retained austenite prior to heating to

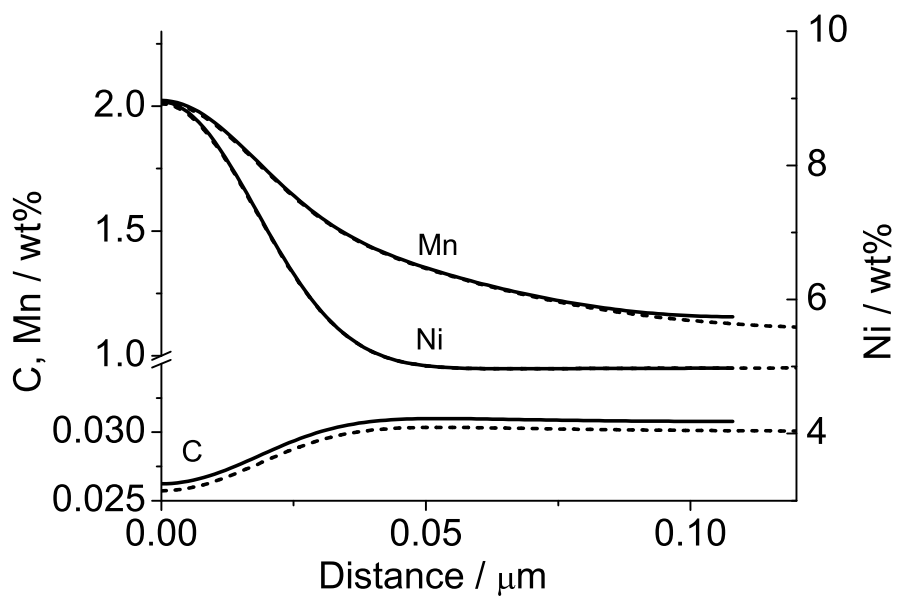


Figure 5.4: Simulation of the spread of alloying elements during austenitization at 780 °C for 10 minutes. Solid lines and dotted lines correspond to the cases where the far-field distance over which diffusion is allowed was set at 0.108 and 1.008 μm , respectively.

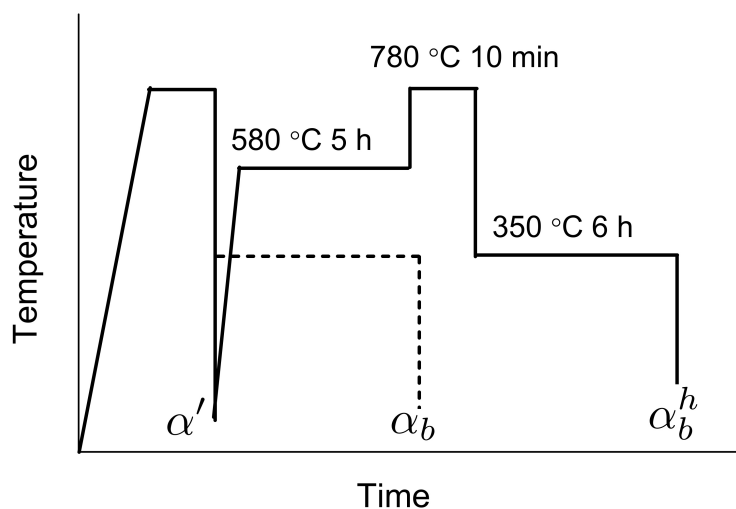


Figure 5.5: Illustration of the heat-treatments used to generate three different microstructures.

580 °C.

It is interesting that the amount of bainite obtained isothermally is greater in the homogeneous when compared with the heterogeneous austenite (Fig. 5.8a); this is consistent with previous observations and is a consequence of the fact that nucleation is generally confined to solute-depleted regions in a segregated steel (Khan and Bhadeshia, 1990; Bhadeshia, 2001). As a consequence, the amount of martensite is greater in the heterogeneous steel (Fig.5.8b).

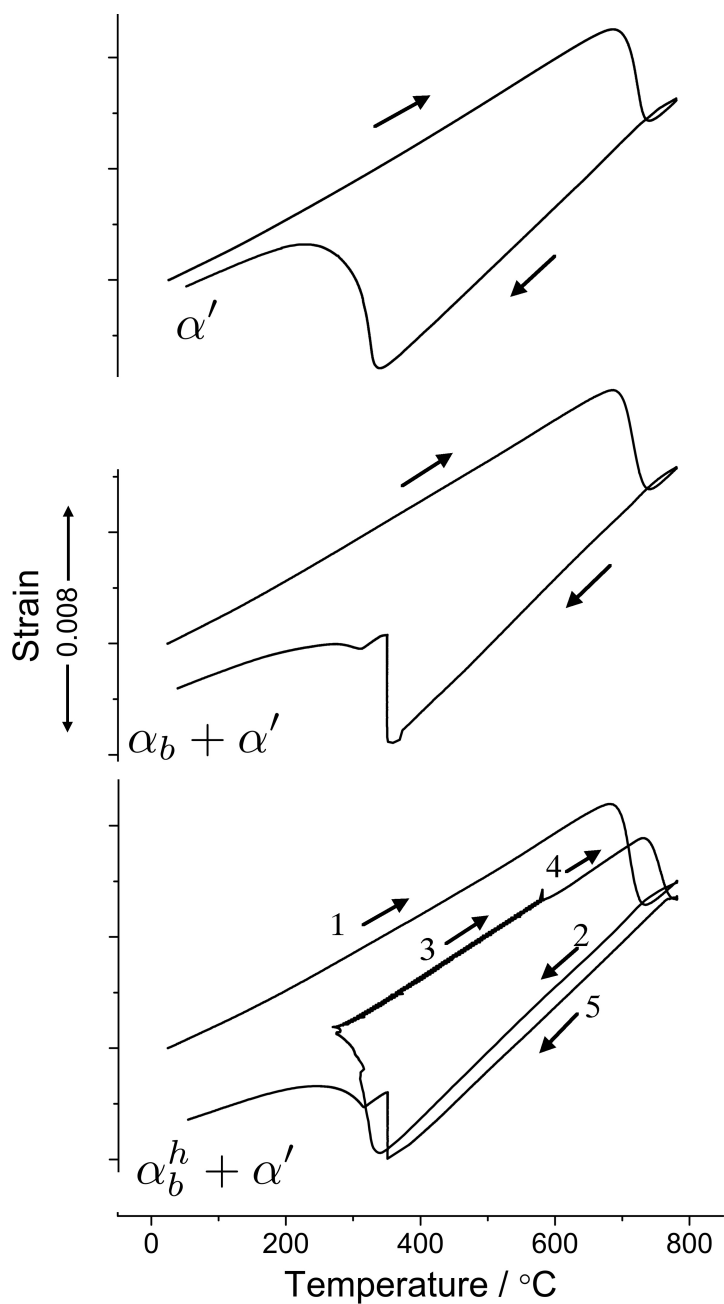


Figure 5.6: Dilatometer curves showing three different heat treatments.

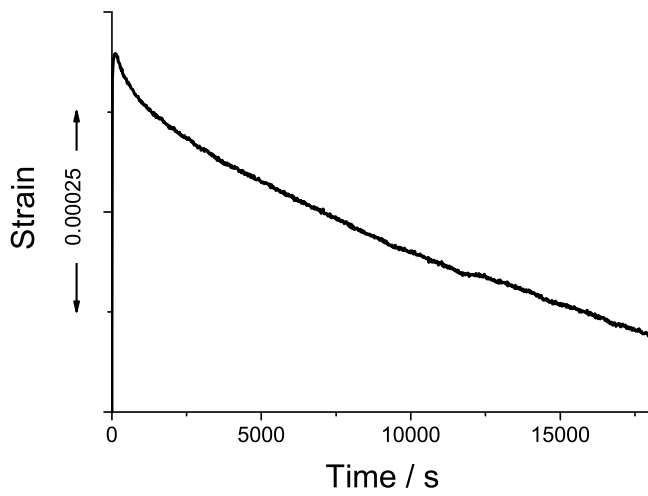
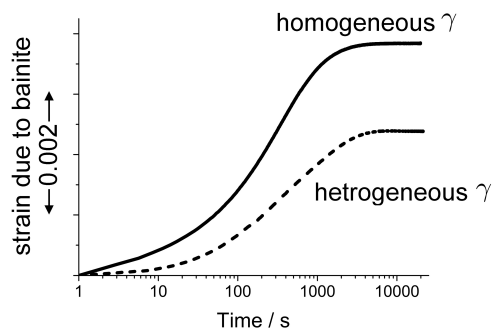
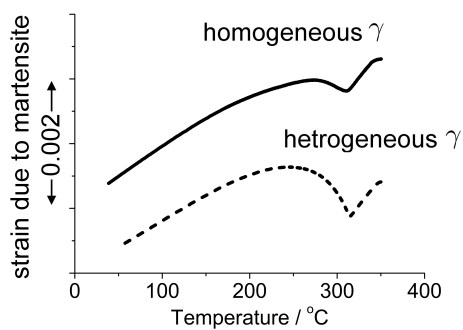


Figure 5.7: Strain due to the intercritical annealing at 580 °C.



(a)



(b)

Figure 5.8: Dilatometric data for the (a) isothermal bainite transformation and (b) the martensite transformation which follows the formation of bainite.

5.3.4 Characterisation

The microstructures are illustrated in Figs 5.9 & 5.10 where an attempt has been made to distinguish between bainite and martensite purely on morphological basis. The heterogeneous sample was subjected to transmission electron microscopy in order to establish the presence of substitutional-solute rich regions. Fig. 5.11 is a region extracted using focused ion beam machining from bainite identified using scanning electron microscopy, in the heterogeneous sample. The circled area was then subjected to microanalysis traversing several boundaries. It is clear from Fig. 5.12, 5.13 that the expected enrichment in manganese and nickel concentrations is indeed present. The agreement between the microanalysis and the calculations using *DICTRA* can be considered to be reasonable given that the spatial resolution will be about the thickness of the foil (not measured, but likely to be around 50 nm), and it is not clear whether the scan direction is normal to the boundary concerned. The experiments establish clearly that the intercritical annealing and short austenitisation treatment succeeded in creating the postulated segregation of substitutional solutes. Some additional scans are shown in Fig.5.14 to show that the enriched regions can be variable, probably because the dimensions of austenite regions formed during intercritical annealing are not likely to be uniform.

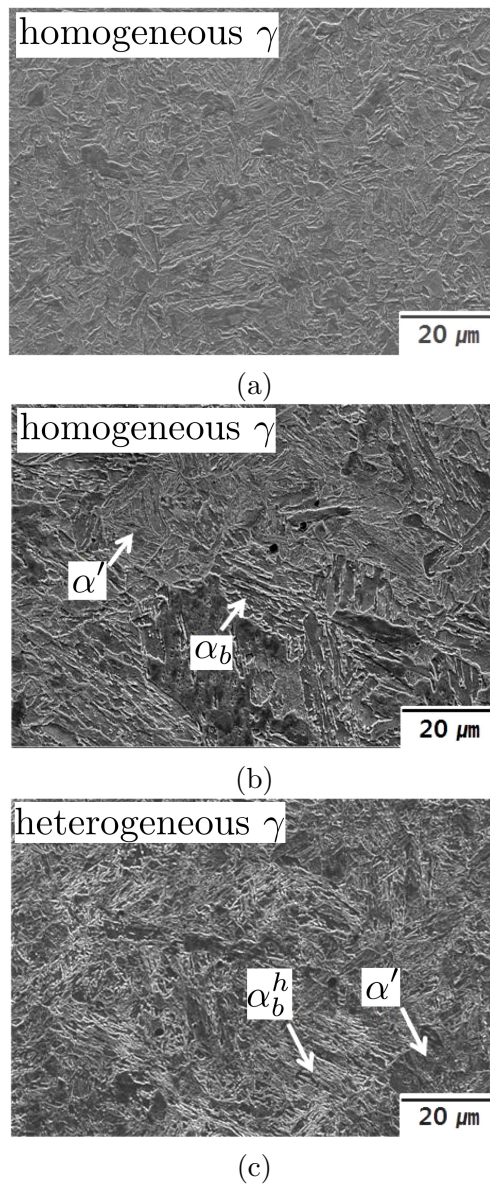
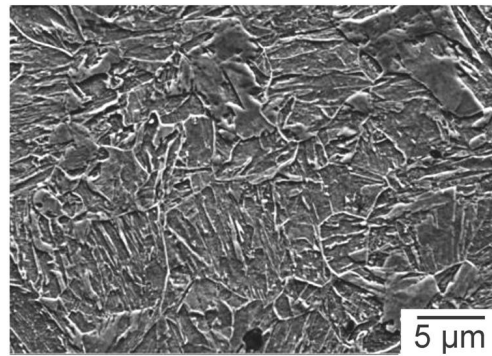
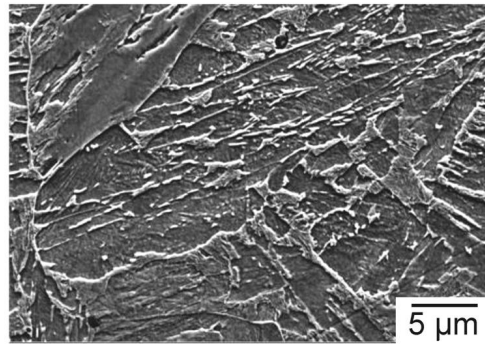


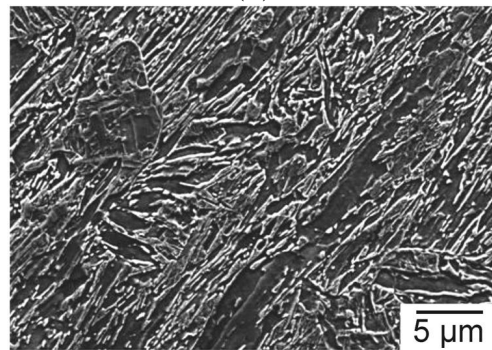
Figure 5.9: Micrographs showing (a) martensite from homogeneous austenite; (b) mixture of bainite and martensite from homogeneous austenite; (c) similar mixture from heterogeneous austenite.



(a)



(b)



(c)

Figure 5.10: Micrographs showing the detailed structure of (a) martensite from homogeneous austenite; (b) bainite in homogeneous austenite; (c) bainite in heterogeneous austenite.



Figure 5.11: Transmission electron micrograph of a region extracted using focused ion beam machining from bainite identified using scanning electron microscopy, in the heterogeneous sample. The circled areas were then subjected to microanalysis.

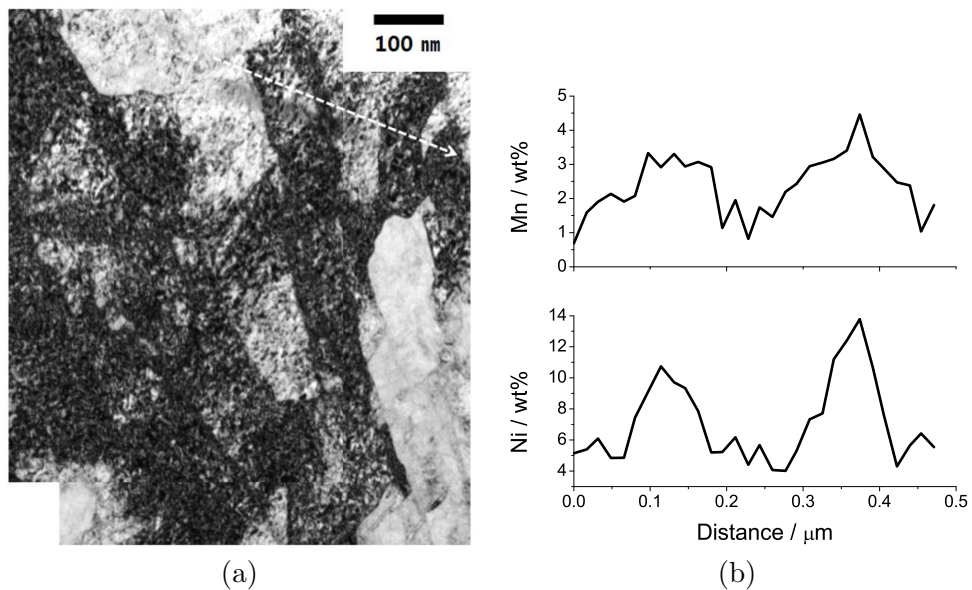


Figure 5.12: (a) The microstructure including the manganese and nickel-enriched area. The arrow corresponds to the direction of the scan in energy dispersive spectroscopy. (b) The concentration of manganese and nickel along the scan.

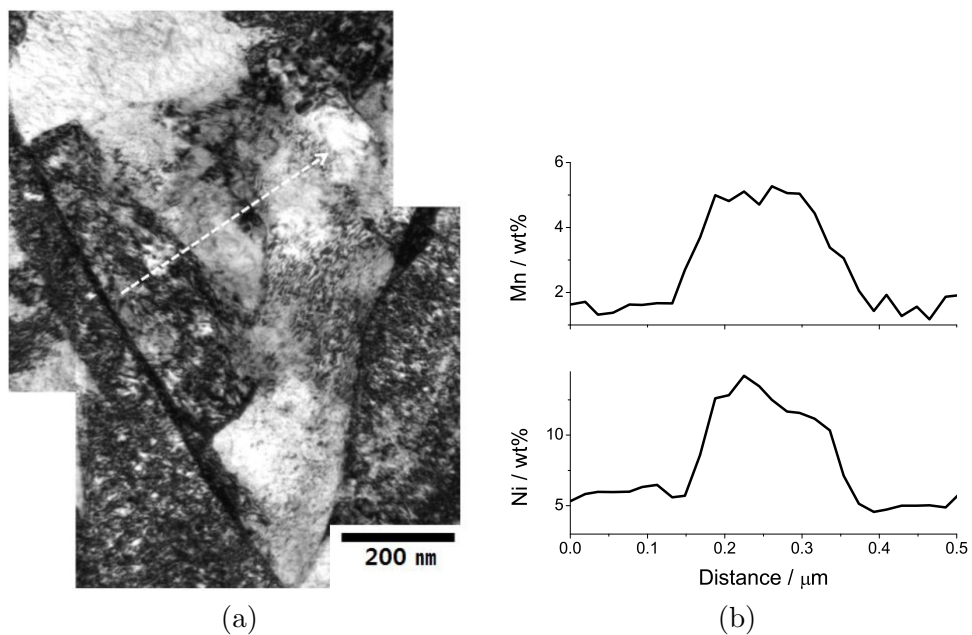


Figure 5.13: (a) The microstructure including the manganese and nickel-enriched area. The arrow corresponds to the direction of the scan in energy dispersive spectroscopy. (b) The concentration of manganese and nickel along the scan.

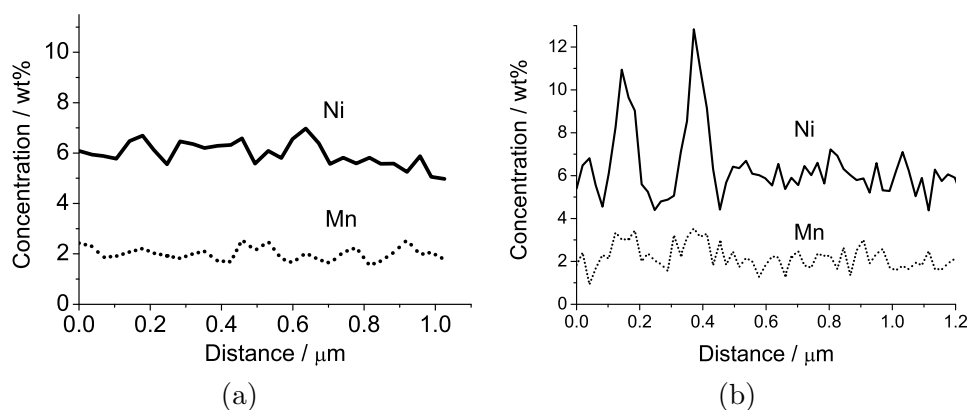


Figure 5.14: Additional microanalysis scanning results for manganese and nickel.

5.3.5 Crystallography

Image quality (IQ) mapping and inverse pole figures were determined on the bainite formed in homogeneous and heterogeneous austenite, as shown in Fig. 5.15. It is clear that the visualised boundaries in quality images are much denser in the bainite from the heterogeneous austenite. Furthermore, the crystallographic grain size is clearly finer with α_b^h , so that the complex heat treatment has succeeded in fragmenting the structure from a crystal orientation point of view.

5.3.6 Effect on coalescence

Even though coalesced structures were not observed in bainite formed in homogeneous austenite due to its low austenitization temperature, where

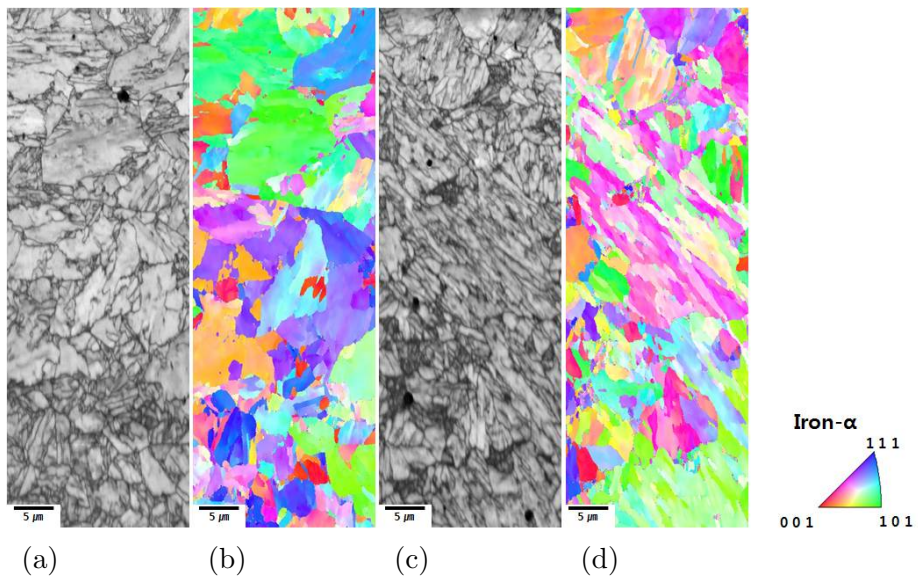


Figure 5.15: Image quality and inverse pole figure images of bainite in (a), (b) homogeneous austenite and (c), (d) heterogeneous austenite.

the austenite grains can not grow large enough to permit coalescence (Bhadeshia et al., 2006), there is no doubt that the designed fragmenting must be efficient to prevent the coalescence. Notice that the fragmenting created not only physical boundaries enriched with substitutional elements on the space where bainite will form but also disturbed there crystallographically, both must block the coalescence.

5.4 Conclusions

It is found that the introduction of chemical heterogeneities can break up the development of microstructure during the bainite transformation, thus resulting in a significantly refined crystallographic grain size. This must be efficient to avoid the coalescence in bainitic structure.

Whereas this was achieved in the present work by introducing segregated regions using heat-treatment, it is possible that solidification-induced segregation, which is inevitably present in commercial steels, could in principle be exploited in the manner described in the paper, although other consequences of such segregation would have to be borne in mind during the investigation of this possibility.

Chapter 6

Summary

Due to the potential risk of the coalesced structure on mechanical properties, its nature in martensitic and bainitic transformation was explored using low-carbon steels.

The existence of coalescence in martensite transformation has been confirmed by the clear bimodal distribution of grain size. The same process in bainite is encouraged at low transformation temperatures due to a sluggish partitioning of carbon and larger driving force available at greater undercoolings below the bainite-start temperature.

The misorientation inside a coalesced region of the martensite was modelled assuming that the plastic relaxation of austenite due to a associated transformation strain affects crystallographic orientation of martensitic

plates which consume the deformed austenite.

The effect of an externally applied stress on the coalescence has been examined, bearing in mind that the strain energy governs it. It is found that martensite, as it approaches a free surface, tends to coalesce because of the relaxation of transformation strains predicted by calculations using dislocation theory. Tensile stress also caused the coalescence of bainitic ferrites selectively depending on their crystallographic orientations.

A novel method to hinder the coalescence of plates has been developed. Solute-enriched regions were created in the austenite prior to bainite formation by intercritical annealing. The appropriate heat treatment was designed by calculation and induced successfully the fragmentation of crystallographically homogeneous domains.

Appendix A

Estimation of the bainite–start temperature

Here, the whole procedure to estimate the bainite–start (B_S) temperatures of each alloy is presented. Fig. A.1 shows the dilatometrically recorded transformation strain due to the bainite at the temperatures indicated for individual alloys. As expected, the maximum strain decreases with the temperature. Since the bainite transformation exhibits the *incomplete reaction phenomenon*, the degree of transformation increases from zero as a function of the undercooling below the bainite–start temperature (Bhadeshia, 2001). However, with Alloy D, reconstructive transformation intervenes at 515 °C during the later stages of reaction (Fig. A.2), so that the maximum strain due to bainite was evaluated as indicated by

the dotted line.

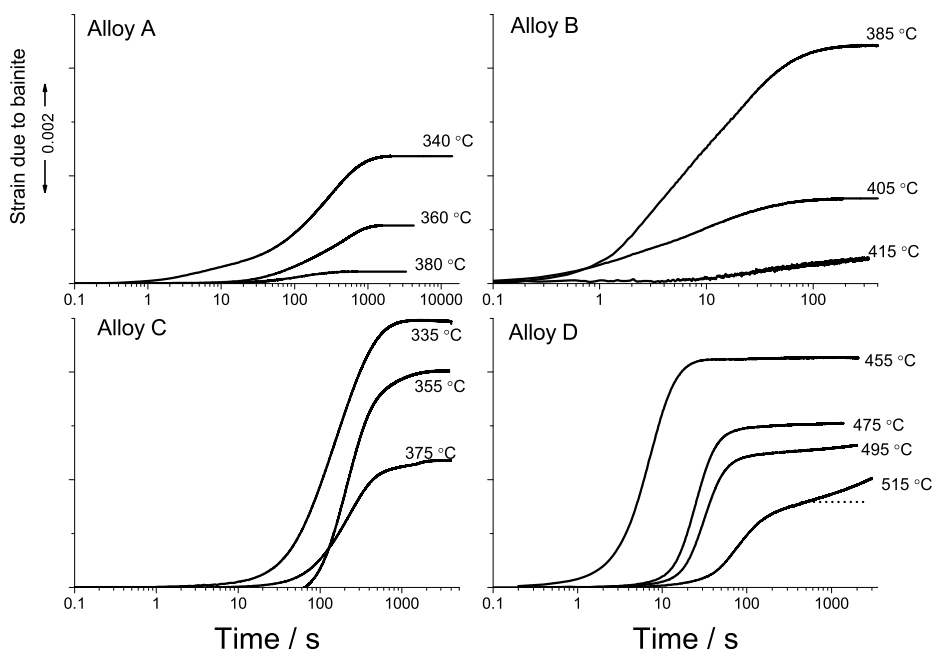


Figure A.1: Strain due to the bainite transformation.

Fig. A.3 shows that the linearity of maximum transformation strain versus transformation temperature was maintained well for the investigated cases, so B_S temperature could be determined by the point where the strain becomes zero, as listed in Table A.1.

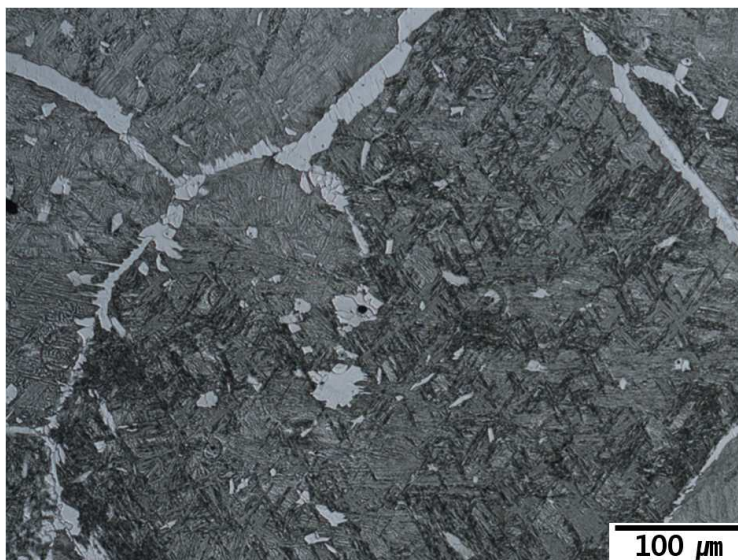


Figure A.2: Polygonal ferrite formed by reconstructive transformation at 515 °C in Alloy D.

Table A.1: The B_S temperatures for each alloy (°C). The error comes from the regression with 95% confidence.

	A	B	C	D
B_S	383 ± 3	418 ± 1	412 ± 9	549 ± 7

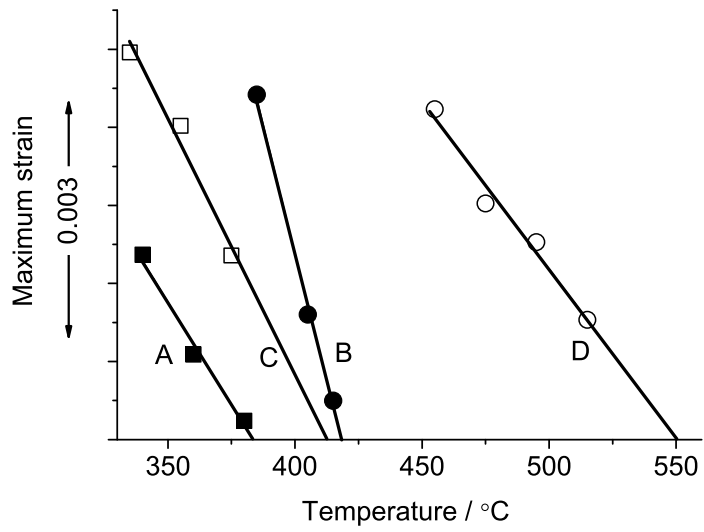


Figure A.3: Estimation of the B_S temperature of each alloy.

Appendix B

Identification of activated slip systems

Given a deformation like that illustrated in Fig. 3.10, the active slip systems can be selected according to *principle of maximum work* (Bishop and Hill, 1951b,a) which equals to Taylor theory. Lee (2006) described the principle that *the state of stress required to cause a given increment of strain is the one that maximizes the work done on the material* and introduced the whole procedure to find the active slip systems using it. Notice any notation from now are consistent with those in (Lee, 2006).

The associated work done on the material can be expressed as shown in Eq. B.1 with respect to arbitrarily oriented orthogonal crystal axes:

$$dW = A d\varepsilon_{22}^c - B d\varepsilon_{11}^c + 2F d\varepsilon_{23}^c + 2G d\varepsilon_{13}^c + 2H d\varepsilon_{12}^c \quad (\text{B.1})$$

where A, B, F, G and H are constants to be determined and superscript c means that the strain is defined with respect to the crystal axis. However, significant geometrical constraints of the deformation are in general given with respect to the deformation axes which contain the slip plane normal and slip direction. For example, in this work, the deformation to be accommodated was assumed to be a simple shear with no dilation (Fig. 3.10), so the related constraints are:

$$d\varepsilon_{12} = d\varepsilon_{21} \neq 0 \quad (\text{B.2a})$$

$$d\varepsilon_{13} = d\varepsilon_{31} = 0 \quad (\text{B.2b})$$

$$d\varepsilon_{23} = d\varepsilon_{32} = 0 \quad (\text{B.2c})$$

$$d\varepsilon_{11} = d\varepsilon_{22} = d\varepsilon_{33} = 0 \quad (\text{B.2d})$$

The incremental strain of Eq. B.1 was newly written as Eq. B.4 using the co-ordinate transformation relation of Eq. B.3, where a_{ij} is a direction cosine value listed in Table B.1, so the incremental work can be written as Eq. B.5.

$$d\varepsilon_{ij}^c = a_{ik}a_{jl}d\varepsilon_{kl} \quad (\text{B.3})$$

Table B.1: Direction cosine values between crystal axes and deformation axes.

		x_1	x_2	x_3
		$\langle \bar{1}01 \rangle$	$\langle 232 \rangle$	$\langle \bar{3}4\bar{3} \rangle$
x_1^c	$\langle 100 \rangle$	$-\frac{1}{\sqrt{2}}$	$\frac{2}{\sqrt{17}}$	$-\frac{3}{\sqrt{34}}$
x_2^c	$\langle 010 \rangle$	0	$\frac{3}{\sqrt{17}}$	$\frac{4}{\sqrt{34}}$
x_3^c	$\langle 001 \rangle$	$\frac{1}{\sqrt{2}}$	$\frac{2}{\sqrt{17}}$	$-\frac{3}{\sqrt{34}}$

$$d\varepsilon_{22}^c = a_{21}a_{22}d\varepsilon_{12} + a_{22}a_{21}d\varepsilon_{21} = 0 \quad (\text{B.4a})$$

$$d\varepsilon_{11}^c = a_{11}a_{12}d\varepsilon_{12} + a_{12}a_{11}d\varepsilon_{21} = -\frac{4}{\sqrt{34}}d\varepsilon_{12} \quad (\text{B.4b})$$

$$d\varepsilon_{23}^c = a_{21}a_{32}d\varepsilon_{12} + a_{22}a_{31}d\varepsilon_{21} = \frac{3}{\sqrt{34}}d\varepsilon_{12} \quad (\text{B.4c})$$

$$d\varepsilon_{13}^c = a_{11}a_{32}d\varepsilon_{12} + a_{12}a_{31}d\varepsilon_{21} = 0 \quad (\text{B.4d})$$

$$d\varepsilon_{12}^c = a_{11}a_{22}d\varepsilon_{12} + a_{12}a_{21}d\varepsilon_{21} = -\frac{3}{\sqrt{34}}d\varepsilon_{12} \quad (\text{B.4e})$$

$$dW = \frac{2}{\sqrt{34}}(2B + 3F - 3H)d\varepsilon_{12} \quad (\text{B.5})$$

Table B.2 shows the constant values which the combinations of twelve

variants of $\{111\} \langle 110 \rangle$ slip system can have, where τ_c is a critical resolved shear stress of the system and minus sign means an opposite slip direction. The slip systems corresponding to the state which maximizes the incremental work of Eq. B.5 will be activated. When several states result in identical maximum values, common slip systems can be selected. Eq. B.5 was maximized when $(2B + 3F - 3H)$ equals to 3 and the corresponding slip systems are $a_2(111) \langle \bar{1}01 \rangle$, $-c_3(\bar{1}11) \langle 110 \rangle$ and $-d_2(1\bar{1}1) \langle 10\bar{1} \rangle$.

Table B.2: the values of constants corresponding to possible combinations of $\{111\} < 110 >$ slip system (Lee, 2006).

		Constants						Slip systems											
A	B	C	F	G	H	a_1	a_2	a_3	b_1	b_2	b_3	c_1	c_2	c_3	d_1	d_2	d_3		
		unit: $\sqrt{6}\tau_c$						(111)			$(\bar{1}\bar{1}\bar{1})$			$(\bar{1}\bar{1}\bar{1})$			$(\bar{1}\bar{1}\bar{1})$		
1	-1	0	0	0	0	+	-	[110]	[011]	[101]	[110]	[011]	[101]	[110]	[011]	[101]	[110]		
0	1	-1	0	0	0	+	+	-	-	+	-	+	+	-	+	+	-	-	
-1	0	1	0	0	0	-	+	+	-	-	+	-	+	+	-	-	+	+	
0	0	0	1	0	0	-	+	-	+	-	+	+	-	-	-	-	+	+	
0	0	0	0	1	0	-	-	+	+	-	-	+	+	-	-	+	+	+	
0	0	0	0	0	1	+	-	+	+	-	-	-	-	-	-	-	+	+	
1/2	-1	1/2	0	1/2	0	+	-	+	+	-	-	+	+	-	+	-	-	+	
1/2	-1	1/2	0	-1/2	0	+	-	+	-	-	+	-	-	+	+	-	-	+	
-1	1/2	1/2	1/2	0	0	-	+	-	-	+	+	-	+	-	-	+	+	+	
-1	1/2	1/2	-1/2	0	0	-	+	+	-	+	-	-	+	+	-	+	+	-	
1/2	1/2	-1	0	0	1/2	+	-	-	+	-	-	-	+	-	-	+	+	-	
1/2	1/2	-1	0	0	-1/2	+	+	-	-	+	-	+	+	-	+	+	-	-	
1/2	0	-1/2	1/2	0	1/2	+	+	-	+	-	-	+	+	-	+	+	-	-	
1/2	0	-1/2	-1/2	0	1/2	+	-	-	+	-	-	+	+	-	+	+	-	-	

continued on next page

Quantitative analysis for each slip requires the other incremental strains, therefore they were also obtained as shown in Eq. B.6. The whole set of strains is listed in Eq. B.7 as matrix notation and in Eq. B.8 as tensor notation defined in (Lee, 2006).

$$d\varepsilon_{21}^c = a_{21}a_{12}d\varepsilon_{12} + a_{22}a_{11}d\varepsilon_{21} = -\frac{3}{\sqrt{34}}d\varepsilon_{12} \quad (\text{B.6a})$$

$$d\varepsilon_{31}^c = a_{31}a_{12}d\varepsilon_{12} + a_{32}a_{11}d\varepsilon_{21} = 0 \quad (\text{B.6b})$$

$$d\varepsilon_{32}^c = a_{31}a_{22}d\varepsilon_{12} + a_{32}a_{21}d\varepsilon_{21} = \frac{3}{\sqrt{34}}d\varepsilon_{12} \quad (\text{B.6c})$$

$$d\varepsilon_{33}^c = a_{31}a_{32}d\varepsilon_{12} + a_{32}a_{31}d\varepsilon_{21} = \frac{4}{\sqrt{34}}d\varepsilon_{12} \quad (\text{B.6d})$$

$$d\varepsilon_{ij}^c = \frac{d\varepsilon_{12}}{\sqrt{34}} \begin{pmatrix} -4 & -3 & 0 \\ -3 & 0 & 3 \\ 0 & 3 & 4 \end{pmatrix} \quad (\text{B.7})$$

$$\begin{pmatrix} d\varepsilon_2^c \\ d\varepsilon_3^c \\ d\varepsilon_4^c \\ d\varepsilon_5^c \\ d\varepsilon_6^c \end{pmatrix} = \frac{2d\varepsilon_{12}}{\sqrt{34}} \begin{pmatrix} 0 \\ 2 \\ 3 \\ 0 \\ -3 \end{pmatrix} \quad (\text{B.8})$$

The displacement by a single slip with shear strain γ can be defined by Eq. B.9, where (n_1, n_2, n_3) and (b_1, b_2, b_3) are components of unit vectors parallel to slip plane normal and slip direction. Using the relation be-

tween displacement and strain (Eq. B.10), the strain expressed as tensor notation can be obtained given a slip system with γ (Eq. B.11). This procedure was conducted for the previously selected slip system considering the corresponding components listed in Table B.3 and Eq. B.12 was obtained. It led to simple equations about shear strains for each slip system (Eq. B.13).

$$e_{ij} = \gamma \begin{pmatrix} b_1 n_1 & b_1 n_2 & b_1 n_3 \\ b_2 n_1 & b_2 n_2 & b_2 n_3 \\ b_3 n_1 & b_3 n_2 & b_3 n_3 \end{pmatrix} \quad (\text{B.9})$$

$$\varepsilon_{ij} = \frac{1}{2}(e_{ij} + e_{ji}) \quad (\text{B.10a})$$

$$\varepsilon_{ij} = \varepsilon_{ji} \quad (\text{B.10b})$$

$$\begin{pmatrix} \varepsilon_2 \\ \varepsilon_3 \\ \varepsilon_4 \\ \varepsilon_5 \\ \varepsilon_6 \end{pmatrix} = \begin{pmatrix} b_2 n_2 \\ b_3 n_3 \\ b_2 n_3 + b_3 n_2 \\ b_1 n_3 + b_3 n_1 \\ b_1 n_2 + b_2 n_1 \end{pmatrix} \gamma \quad (\text{B.11})$$

$$\frac{2d\varepsilon_{12}}{\sqrt{34}} \begin{pmatrix} 0 \\ 2 \\ 3 \\ 0 \\ -3 \end{pmatrix} = \frac{1}{\sqrt{6}} \begin{pmatrix} 0 & 1 & 0 \\ 1 & 0 & -1 \\ 1 & 1 & 1 \\ 0 & 1 & 0 \\ -1 & 0 & -1 \end{pmatrix} \begin{pmatrix} \gamma_{a_2} \\ \gamma_{-c_3} \\ \gamma_{-d_2} \end{pmatrix} \quad (\text{B.12})$$

Table B.3: Components of unit vectors parallel to slip plane normal and slip direction for selected slip systems.

	$a_2(111)[\bar{1}01]$	$-c_3(\bar{1}11)[110]$	$-d_2(1\bar{1}1)[10\bar{1}]$
(b_1, b_2, b_3)	$(-\frac{1}{\sqrt{2}}, 0, \frac{1}{\sqrt{2}})$	$(\frac{1}{\sqrt{2}}, \frac{1}{\sqrt{2}}, 0)$	$(\frac{1}{\sqrt{2}}, 0, -\frac{1}{\sqrt{2}})$
(n_1, n_2, n_3)	$(\frac{1}{\sqrt{3}}, \frac{1}{\sqrt{3}}, \frac{1}{\sqrt{3}})$	$(-\frac{1}{\sqrt{3}}, \frac{1}{\sqrt{3}}, \frac{1}{\sqrt{3}})$	$(\frac{1}{\sqrt{3}}, -\frac{1}{\sqrt{3}}, \frac{1}{\sqrt{3}})$

$$\gamma_{-c_3} = 0 \quad (\text{B.13a})$$

$$\gamma_{a_2} - \gamma_{-d_2} = \frac{4\sqrt{6}}{\sqrt{34}} d\varepsilon_{12} \quad (\text{B.13b})$$

$$\gamma_{a_2} + \gamma_{-d_2} = \frac{6\sqrt{6}}{\sqrt{34}} d\varepsilon_{12} \quad (\text{B.13c})$$

In the end, only two slip systems of $a_2(111)[\bar{1}01]$ and $-d_2(1\bar{1}1)[10\bar{1}]$ can be activated with each shear strain corresponding to the magnitudes of $(5/\sqrt{34})d\varepsilon_{12}$ and $(1/\sqrt{34})d\varepsilon_{12}$, respectively.

Appendix C

Calculation of rotation matrices

The rotation of crystal can be efficiently described by a rotation axis-angle pair, which can be mathematically represented as a matrix form:

$$R = \begin{pmatrix} u_1 u_1 (1 - m) + m & u_1 u_2 (1 - m) + u_3 n & u_1 u_3 (1 - m) - u_2 n \\ u_1 u_2 (1 - m) - u_3 n & u_2 u_2 (1 - m) + m & u_2 u_3 (1 - m) + u_1 n \\ u_1 u_3 (1 - m) + u_2 n & u_2 u_3 (1 - m) - u_1 n & u_3 u_3 (1 - m) + m \end{pmatrix} \quad (\text{C.1})$$

which rotates crystal about the axis of (u_1, u_2, u_3) with the right handed angle of θ , where $\sum u_i^2 = 1$, $m = \cos \theta$ and $n = \sin \theta$ (Bhadeshia, 1987). In the rotation by a single slip as illustrated in Fig. 3.9a, the rotation axis corresponds to the vector perpendicular to both slip plane normal and slip

direction and, therefore the rotation axes of $(111)[\bar{1}01]$ and $(\bar{1}\bar{1}1)[10\bar{1}]$ slips were defined as unit vectors of $[\bar{1}2\bar{1}]$ and $[\bar{1}\bar{2}\bar{1}]$, respectively. The rotation angle can be obtained from Eq. 3.1. The density of the *excess* dislocations was estimated as a fraction (ϕ) of that of existing dislocation of Eq. 3.2. The specific values for parameters in Eq. 3.1 are shown in Table C.1.

Table C.1: Specific values for parameters in Eq. 3.1.

ρ	6.01×10^{15}	(m^{-2})
b	3.604	(\AA)
L	0.2	(μm)

The rotation by multiple slip can be expressed as products of each rotation matrix, where the rotation sequence is reflected in the calculation. Given final rotation matrix, the resultant rotation axis and angle can be obtained by followings:

$$R_{11} + R_{22} + R_{33} = 1 + 2 \cos \theta \quad (\text{C.2a})$$

$$u_1 = (R_{23} - R_{32})/2 \sin \theta \quad (\text{C.2b})$$

$$u_2 = (R_{31} - R_{13})/2 \sin \theta$$

$$u_3 = (R_{12} - R_{21})/2 \sin \theta$$

The notation rules for the rotation matrix R is same with that of Table. 3.1, where subscript a, b mean the activated slip systems, $(111)[\bar{1}01]$ and

$(\bar{1}\bar{1}1)[10\bar{1}]$, respectively. The fractional number in front of R represents the degree by which the slip has progressed, that is proportional to the density of dislocations participated in the reaction. Notice that the ratio of $(111)[\bar{1}01]$ slip dislocations to $(\bar{1}\bar{1}1)[10\bar{1}]$ dislocations was set as 5 by the solution of Eq. B.13. Here only two examples were illustrated but the others also can be obtained by following the same procedure.

C.1 $R_b R_a$ at $\phi = 0.25$

At $\phi = 0.25$, rotation matrix $R_b R_a$ was obtained by followings. First, the *excess* density for each dislocation was estimated in Eq. C.3.

$$\rho_a^{excess} = 6.01 \times 10^{15} \times 0.25 \times \frac{5}{6} = 1.25 \times 10^{15} \text{ (m}^{-2}\text{)} \quad (\text{C.3a})$$

$$\rho_b^{excess} = 6.01 \times 10^{15} \times 0.25 \times \frac{1}{6} = 2.50 \times 10^{14} \text{ (m}^{-2}\text{)} \quad (\text{C.3b})$$

Using Eq. C.1, R_a and R_b can be constructed (Eq. C.4a, b).

$$R_a = \begin{pmatrix} 0.998304 & -0.026714 & -0.051731 \\ 0.025357 & 0.999321 & -0.026714 \\ 0.052410 & 0.025357 & 0.998304 \end{pmatrix} \quad (\text{C.4a})$$

$$R_b = \begin{pmatrix} 0.999932 & -0.005183 & 0.010434 \\ 0.005238 & 0.999973 & -0.005183 \\ -0.010407 & 0.005238 & 0.999932 \end{pmatrix} \quad (\text{C.4b})$$

Then the matrix product $R_b R_a$ representing the multiple slip where the complete b slip follows the complete a slip can be obtained (Eq. C.5).

$$R_b R_a = \begin{pmatrix} 0.998635 & -0.032158 & -0.041173 \\ 0.030868 & 0.999023 & -0.031627 \\ 0.042150 & 0.030314 & 0.998652 \end{pmatrix} \quad (\text{C.5})$$

Finally, the resultant rotation axis and angle implied in $R_b R_a$ can be obtained by Eq. C.2. They were that $(u_1, u_2, u_3) = (-0.519, 0.686, -0.510)$ and $\theta = 3.48^\circ$.

C.2 $\frac{1}{2}R_b\frac{1}{2}R_a\frac{1}{2}R_b\frac{1}{2}R_a$ at $\phi = 0.25$

The half of rotation occurs by half of the dislocation related to the slip. Therefore the dislocation density associated with each rotation step, $\frac{1}{2}R_a$ or $\frac{1}{2}R_b$ equals to that at $\phi = 0.125$

$$\rho_a^{excess} = 6.01 \times 10^{15} \times 0.125 \times \frac{5}{6} = 6.26 \times 10^{14} \text{ (m}^{-2}\text{)} \quad (\text{C.6a})$$

$$\rho_b^{excess} = 6.01 \times 10^{15} \times 0.125 \times \frac{1}{6} = 1.25 \times 10^{14} \text{ (m}^{-2}\text{)} \quad (\text{C.6b})$$

Now, the rotation matrices for $\frac{1}{2}R_a$ and $\frac{1}{2}R_b$ can be constructed as shown in Eq. C.7 using Eq. C.1.

$$\frac{1}{2}R_a = \begin{pmatrix} 0.999576 & -0.013194 & -0.025964 \\ 0.012855 & 0.999830 & -0.013194 \\ 0.026133 & 0.012855 & 0.999576 \end{pmatrix} \quad (\text{C.7a})$$

$$\frac{1}{2}R_b = \begin{pmatrix} 0.999983 & -0.002598 & 0.005214 \\ 0.002612 & 0.999993 & -0.002598 \\ -0.005207 & 0.002612 & 0.999983 \end{pmatrix} \quad (\text{C.7b})$$

Then the matrix product $\frac{1}{2}R_b\frac{1}{2}R_a\frac{1}{2}R_b\frac{1}{2}R_a$ representing the total multiple

slip can be obtained (Eq. C.8).

$$\frac{1}{2}R_b\frac{1}{2}R_a\frac{1}{2}R_b\frac{1}{2}R_a = \begin{pmatrix} 0.998647 & -0.031761 & -0.041172 \\ 0.030454 & 0.999022 & -0.032027 \\ 0.042148 & 0.030731 & 0.998639 \end{pmatrix} \quad (\text{C.8})$$

The resultant rotation axis and angle implied in $\frac{1}{2}R_b\frac{1}{2}R_a\frac{1}{2}R_b\frac{1}{2}R_a$ were obtained from Eq. C.2 as that $(u_1, u_2, u_3) = (-0.517, 0.686, -0.512)$ and $\theta = 3.48^\circ$.

Bibliography

Aaronson, H. I. and Lee, H. J. (1987). Another visit to the three definitions of bainite. *Scripta Metallurgica*, 21(8):1011–1016.

Ali, A. and Bhadeshia, H. K. D. H. (1989). Growth rate data on bainite in alloy steels. *Materials Science and Technology*, 5(4):398–402.

Ali, A. and Bhadeshia, H. K. D. H. (1990). Nucleation of Widmanstätten ferrite. *Materials Science and Technology*, 6(8):781–784.

Bach, P. W., Beyer, J., and Verbraak, C. A. (1980). Atom probe analysis of bainitic phase boundaries in a low alloyed Cr Mo steel. *Scripta Metallurgica*, 14(2):205–210.

Bain, E. and Paxton, H. (1966). *Alloying elements in steel*. American Society for Metals.

Barbacki, A. (1995). The role of bainite in shaping mechanical properties of steels. *Journal of Materials Processing Tech.*, 53(1-2):57–63.

- Bhadeshia, H. K. D. H. (1979). *Theory and significance of retained austenite in steels*. PhD thesis, University of Cambridge.
- Bhadeshia, H. K. D. H. (1981). A rationalisation of shear transformations in steels. *Acta Metallurgica*, 29(6):1117–1130.
- Bhadeshia, H. K. D. H. (1987). *Worked examples in the geometry of crystals*. The Institute of Metals, London.
- Bhadeshia, H. K. D. H. (2001). *Bainite in steels: transformations, microstructure and properties*. IOM Communications Ltd., London.
- Bhadeshia, H. K. D. H. (2004). Developments in martensitic and bainitic steels: Role of the shape deformation. *Materials Science and Engineering A*, 378(1-2 SPEC. ISS.):34–39.
- Bhadeshia, H. K. D. H. and Edmonds, D. V. (1979). The bainite transformation in a silicon steel. *Metallurgical Transactions A*, 10(7):895–907.
- Bhadeshia, H. K. D. H. and Edmonds, D. V. (1980). Mechanism of bainite formation in steels. *Acta Metallurgica*, 28(9):1265–1273.
- Bhadeshia, H. K. D. H., Keehan, E., Karlsson, L., and Andrén, H. O. (2006). Coalesced bainite. *Transactions of the Indian Institute of Metals*, 59(5):689–694.
- Bhadeshia, H. K. D. H. and Mateo, C. (2001). Kinetic calculation program. <http://www.msm.cam.ac.uk/map/steel/programs/partition.html>.

- Bhadeshia, H. K. D. H. and Waugh, A. R. (1982). Bainite: An atom-probe study of the incomplete reaction phenomenon. *Acta Metallurgica*, 30(4):775–784.
- Bishop, J. F. W. and Hill, R. (1951a). A theoretical derivation of the plastic properties of a polycrystalline face centered metal. *Philosophical Magazine*, 42:1298–1307.
- Bishop, J. F. W. and Hill, R. (1951b). A theory of the plastic distortion of a polycrystalline aggregate under combined stresses. *Philosophical Magazine*, 42:414–427.
- Bowles, J. and Barrett, C. (1952). *Progress in Metal Physics III*. Pergamon Press.
- Bowles, J. S. and Mackenzie, J. K. (1954a). The crystallography of martensite transformations I. *Acta Metallurgica*, 2(1):129–137.
- Bowles, J. S. and Mackenzie, J. K. (1954b). The crystallography of martensite transformations III. Face-centred cubic to body-centred tetragonal transformations. *Acta Metallurgica*, 2(2):224–234.
- Bradley, J. R. and Aaronson, H. I. (1981). Growth kinetics of grain boundary ferrite allotriomorphs in Fe-C-X alloys. *Metallurgical transactions. A, Physical metallurgy and materials science*, 12 A(10):1729–1741.
- Bratberg, J. (2011). Private communication from DICTRA staff.

- Bunshah, R. F. and Mehl, R. F. (1953). Rate of propagation of martensite. *AIME Transactions*, 197:1251–1258.
- Chang, L. C. and Bhadeshia, H. K. D. H. (1995a). Austenite films in bainitic microstructures. *Materials Science and Technology*, 11(9):874–881.
- Chang, L. C. and Bhadeshia, H. K. D. H. (1995b). Metallographic observations of bainite transformation mechanism. *Materials Science and Technology*, 11(2):105–108.
- Chang, L. C. and Bhadeshia, H. K. D. H. (1996). Microstructure of lower bainite formed at large undercoolings below bainite start temperature. *Materials Science and Technology*, 12(3):233–236.
- Chikama, H., Shibata, H., Emi, T., and Suzuki, M. (1996). In-situ real time observation of planar to cellular and cellular to dendritic transition of crystals growing in Fe-C alloy metals. *Materials Transactions, JIM*, 37(4):620–626.
- Christian, J. (1965). *The theory of transformations in metals and alloys: an advanced textbook in physical metallurgy*. International series of monographs on metal physics and physical metallurgy. Pergamon Press.
- Christian, J. W. (1958). Accommodation strains in martensite formation, and the use of a dilatation parameter. *Acta Metallurgica*, 6(5):377–379.

- Christian, J. W. (1979). Thermodynamics and kinetics of martensite. In Olson, G. B. and Cohen, M., editors, *Proceedings of the international conference on martensitic transformations-ICOMAT '79*, pages 220–234. Department of Materials Science and Engineering, MIT.
- Christian, J. W. (1990). Simple geometry and crystallography applied to ferrous bainites. *Metallurgical transactions.A, Physical metallurgy and materials science*, 21 A(4):799–803.
- Davenport, A. T. (1974). The crystallography of upper bainite. Technical report, Republic Steel Research Rep. on Project 12051.
- Dunne, D. P. and Wayman, C. M. (1971). The crystallography of ferrous martensites. *Metallurgical Transactions*, 2(9):2327–2341.
- Head, A. K. (1953). Edge dislocations in inhomogeneous media. *Proceedings of the Physical Society. Section B*, 66(9):793–801.
- Hirano, K., Cohen, M., and Averbach, B. L. (1961). Diffusion of nickel into iron. *Acta Metallurgica*, 9(5):440–445.
- Hirth, J. and Lothe, J. (1992). *Theory of dislocations*. Krieger Pub. Co.
- Josefsson, B. and Andrén, H. O. (1991). Atom probe field ion microscopy of bainitic transformation in 2.25Cr-1Mo weld metal. *Materials Science and Technology*, 7(9):849–851.

Jung, Y. C., Kim, S. J., and Ohmori, Y. (1998). Morphology and growth process of bainitic ferrite in steels. *Metals and Materials International*, 4(2):125–134.

Kaufman, L., Leyenaar, A., and Harvey, J. (1960). The effect of hydrostatic pressure on the potency of martensitic embryos. *Acta Metallurgica*, 8(4):270 – 272.

Keehan, E., Karlsson, L., Andrén, H. O., and Bhadeshia, H. K. D. H. (2005). Understanding mechanical properties of novel high strength steel weld metals through high-resolution microstructural investigations. In *ASM Proceedings of the International Conference: Trends in Welding Research*, volume 2005, pages 969–974.

Keehan, E., Karlsson, L., Andrén, H. O., and Bhadeshia, H. K. D. H. (2006a). Influence of carbon, manganese and nickel on microstructure and properties of strong steel weld metals: Part 2 - impact toughness gain resulting from manganese reductions. *Science and Technology of Welding and Joining*, 11(1):9–18.

Keehan, E., Karlsson, L., Andrén, H. O., and Bhadeshia, H. K. D. H. (2006b). New developments with C-Mn-Ni high-strength steel weld metals, part A - Microstructure. *Welding Journal (Miami, Fla)*, 85(9):200–210.

Keehan, E., Karlsson, L., Andrén, H. O., and H., B. H. K. D. (2006c). In-

- fluence of C, Mn and Ni on Strong Steel Weld Metals: Part 3, Increased Strength. *Science and Technology of Welding and Joining*, 11:19–24.
- Keehan, E., Karlsson, L., Andrén, H. O., and Svensson, L. E. (2006d). New developments with C-Mn-Ni in high-strength steel weld metals - part B, mechanical properties. *Welding Journal*, 85(10):218–224.
- Keehan, E., Karlsson, L., Bhadeshia, H. K. D. H., and Thuvander, M. (2008a). Electron backscattering diffraction study of coalesced bainite in high strength steel weld metals. *Materials Science and Technology*, 24(10):1183–1188.
- Keehan, E., Karlsson, L., Bhadeshia, H. K. D. H., and Thuvander, M. (2008b). Three-dimensional analysis of coalesced bainite using focused ion beam tomography. *Materials Characterization*, 59(7):877–882.
- Khan, S. A. and Bhadeshia, H. K. D. H. (1990). Bainite transformation in chemically heterogeneous 300M high-strength steel. *Metallurgical transactions.A, Physical metallurgy and materials science*, 21 A(4):859–875.
- Komizo, Y., Terasaki, H., and Osuki, T. (2008). Development of in-situ microstructure observation technique in welding. *Welding in the world*, 52:56–63.
- Lee, D. N. (2006). *Texture and related phenomena*. Hanrimwon Publishing Company, Seoul.

- Li, C. and Wang, J. L. (1993). Effect of pre-quenching on martensite-bainitic microstructure and mechanical properties of GCr15 bearing steel. *Journal of Materials Science*, 28(8):2112–2118.
- Mackenzie, J. K. and Bowles, J. S. (1954). The crystallography of martensite transformations II. *Acta Metallurgica*, 2(1):138–147.
- Miyamoto, G., Takayama, N., and Furuhashi, T. (2009). Accurate measurement of the orientation relationship of lath martensite and bainite by electron backscatter diffraction analysis. *Scripta Materialia*, 60(12):1113–1116.
- Morito, S., Nishikawa, J., and Maki, T. (2003). Dislocation density within lath martensite in Fe-C and Fe-Ni alloys. *ISIJ International*, 43(9):1475–1477.
- Oblak, J. P. and Hehemann, R. (1967). Transformations and hardenability in steels. *Climax Molybdenum Co.*, pages 15–30.
- Ohmori, Y. and Maki, T. (1991). Bainitic transformation in view of displacive mechanism. *Materials Transactions, JIM*, 32(8):631–641.
- Okumura, T. and Sourmail, T. (2004). Thermodynamic calculation program. <http://www.msm.cam.ac.uk/map/steel/programs/MTTTDATA.html>.
- Olson, G. B. (1981). Fine structure of interphase boundaries. *Acta Metallurgica*, 29(8):1475–1484.

- Olson, G. B. and Cohen, M. (1979). Interphase-boundary dislocations and the concept of coherency. *Acta Metallurgica*, 27(12):1907–1918.
- Olson, G. B. and Cohen, M. (1981). A perspective on martensitic nucleation. *Annual Review of Materials Science*, 11:1–30.
- Padmanabhan, R. and Wood, W. E. (1984). On the occurrence of blocky martensite in 300M steel. *Materials Science and Engineering*, 66(1):1–11.
- Pak, J. H., Bhadeshia, H. K. D. H., Karlsson, L., and Keehan, E. (2008). Coalesced bainite by isothermal transformation of reheated weld metal. *Science and Technology of Welding and Joining*, 13(7):593–597.
- Patel, J. R. and Cohen, M. (1953). Criterion for the action of applied stress in the martensitic transformation. *Acta Metallurgica*, 1(5):531–538.
- Rees, G. I. and Bhadeshia, H. K. D. H. (1992a). Bainite transformation kinetics. Part 1. Modified model. *Materials Science and Technology*, 8(11):985–993.
- Rees, G. I. and Bhadeshia, H. K. D. H. (1992b). Bainite transformation kinetics. Part 2. Non-uniform distribution of carbon. *Materials Science and Technology*, 8(11):994–996.
- Reynolds Jr., W. T., Aaronson, H. I., and Spanos, G. (1991). Summary of

- the present diffusionist views on bainite. *Materials Transactions, JIM*, 32(8):737–746.
- Russell, K. C. (1969). Grain boundary nucleation kinetics. *Acta Metallurgica*, 17(8):1123–1131.
- Sandvik, B. P. J. (1982). The Bainite reaction in Fe-Si-C Alloys: The primary stage. *Metallurgical Transactions A*, 13(5):777–787.
- Saxena, V. K., Malakondaiah, G., Radhakrishnan, V. M., and Rao, P. R. (1993). On the fatigue crack growth resistance of upper bainite-martensite in an AISI 4330 steel. *Scripta Metallurgica et Materiala*, 28(10):1257–1260.
- Self, P. G., Bhadeshia, H. K. D. H., and Stobbs, W. M. (1981). Lattice spacings from lattice fringes. *Ultramicroscopy*, 6(1):29–40.
- Srinivasan, G. R. and Wayman, C. M. (1968). The crystallography of the bainite transformation I. *Acta Metallurgica*, 16(5):621–636.
- Stark, I., Smith, G. D. W., and Bhadeshia, H. K. D. H. (1990). The distribution of substitutional alloying elements during the bainite transformation. *Metallurgical transactions.A, Physical metallurgy and materials science*, 21 A(4):837–844.
- Swallow, E. and Bhadeshia, H. K. D. H. (1996). High resolution obser-

- vations of displacements caused by bainitic transformation. *Materials Science and Technology*, 12:121–125.
- Takahashi, M. and Bhadeshia, H. K. D. H. (1990). Model for Transition from Upper to Lower Bainite. *Materials Science and Technology*, 6:592–603.
- Tomita, Y. and Okabayashi, K. (1983). Improvement in lower temperature mechanical properties of 0.40 pct C-Ni-Cr-Mo ultrahigh strength steel with the second phase lower bainite. *Metallurgical transactions.A, Physical metallurgy and materials science*, 14 A(3):485–492.
- Tsuzaki, K., Kodai, A., and Maki, T. (1994). Formation mechanism of bainitic ferrite in an Fe-2 Pct Si-0.6 Pct C alloy. *Metallurgical and Materials Transactions A*, 25(9):2009–2016.
- Wakasa, K. and Wayman, C. M. (1979). Crystallography and morphology of surface martensite in Fe-20%Ni-5%Mn. *Scripta Metallurgica*, 13(12):1163–1166.
- Wayman, C. M. (1975). Shear transformations and microstructure. *Metallography*, 8(2):105–130.
- Yang, H. S. and Bhadeshia, H. K. D. H. (2007). Uncertainties in dilatometric determination of martensite start temperature. *Materials Science and Technology*, 23(5):556–560.

- Yang, H.-S., Pak, J. H., and Bhadeshia, H. K. D. H. (2009). Possibility of low-carbon, low-temperature bainite. In Olson, G. B., Lieberman, D. S., and Saxena, A., editors, *Proceedings of the international conference on martensitic transformations-ICOMAT 08*, pages 695–702. The Minerals, Metals and Materials Society.
- Yang, Z. G. and Fang, H. S. (2005). An overview on bainite formation in steels. *Current Opinion in Solid State and Materials Science*, 9(6):277–286.
- Yang, Z. G., Fang, H. S., Wang, J. J., Li, C. M., and Zheng, Y. K. (1995). Surface relief accompanying martensitic transitions in an Fe-Ni-C alloy by atomic-force microscopy and phenomenological theory of martensitic crystallography. *Physical Review B*, 52(11):7879–7882.
- Yin, F., Gu, N., Kang, M., and Liu, W. (1990). The fatigue life of a complex microstructure with bainite in a high carbon Cr-Si tool steel. *Metallurgical Transactions A*, 21(8):2282–2286.
- Young, C. H. and Bhadeshia, H. K. D. H. (1994). Strength of mixtures of bainite and martensite. *Materials Science and Technology*, 10(3):209–214.

Acknowledgements

I am an extremely lucky guy.

I still remember the instant in early 2006 when I started to learn ‘steel’ for the very first time in my life. At that time I didn’t know what even ‘austenite’ stands for. But, now I am closing my doctor course in GIFT, which is possible definitely due to many helps and supports from GIFT and people close to me. That’s why I am lucky.

First of all, I am very appreciating that professor Hae-Gun Lee, the former dean of GIFT, gave me chance to study in GIFT. I also deeply thank to POSCO, which supported me during my doctor course.

I can’t find any appropriate words enough to express my deep gratitude and great respect to professor Bhadeshia, my supervisor. He always inspired me, trusted me and waited me so that I could approach to a goal, which I never expected to be there.

I am also deeply appreciating to professor Suh, Dong-Woo, who has practically cared for my GIFT life including my research. I was truly moved when I heard that he is always praying that we can access the truth of academic question. I also thank to professor Kim, In-Gee, who also kindly

cared me.

I also sincerely would like to thank to Dr. Leif Karlsson in ESAB, who provided the material for the research and sometimes gave me advice.

I must not omit to thank to CML member; Hong-Seok, Joo-Hyun, Jae-Yong, Min-Sung, Tae-Ki 'hyung-nym', Geun-Su, Jee-Yong, Jae-Hoon, Young-Joo, You-Young, Seung-Woo, Dr. Yun, Won-Seok, Dr. Zhang, Miss Kwon, Eun-Jeong and Mr. Kim, Young-Bhum and every member who had stayed in CML with me. I hope all of them to achieve their goals in GIFT and their life.

There are several friends whom I should mention now; Hong-seok, Dong-hui, Tae-Jin, Hee-Yong and Il-chul. The discussion I had with them was really helpful for my research. They sometimes spent long time kindly to help my experiments.

I can't miss a promise to mention Seung-Woo's kind help for using Latex.

I also deeply thank to all GIFT students, those who interacted me in terms of research or any activities. I especially thank to GIFT base ball team members, who let me know the pleasure of playing baseball.

I also would like to express my thanks to all GIFT staff, especially, RFC staff including Mr. Park, Keun-Chang, who always considered my experiments.

Now I really thank to my family in Seoul, Ha-yang and Dae-gu. They always support me and encourage me.

Finally I want to express my deep thanks to my wife, Sung Hwa and my son, Go Gyun. I could do my doctor course since they have been with me.

Curriculum Vitae

Name: Pak, Junhak

E-mail: junhark@postech.ac.kr; junhark@posco.co.kr

Date of birth: 2th October, 1980

Place of birth: Seoul, South Korea

Education

Ph. D. 2012, POSTECH (Pohang, Korea), Graduate Institute of Ferrous Technology, Computational Metallurgy Group

M. S. 2008, POSTECH (Pohang, Korea), Graduate Institute of Ferrous Technology, Computational Metallurgy Group

B. S. 2006, Yonsei University (Seoul, Korea), Department of Physics

Publications

Pak, Junhak and Bhadeshia, H. K. D. H. (2008). Coalesced bainite by isothermal transformation of reheated weld metal. *Science and Technology of Welding and Joining*, 13:593-597

Pak, Junhak, Suh, Dong-Woo and Bhadeshia, H. K. D. H. (2011). Bainite: Fragmentation of Crystallographically Homogeneous Domains, Accepted by International Journal of MATERIALS RESEARCH

Pak, Junhak and H. K. D. H. (2011). Mechanism of Misorientation Development within Coalesced Martensite, Submitted

Pak, Junhak, Suh, Dong-Woo and Bhadeshia, H. K. D. H. (2011). Displacive Phase Transformation and Surface Effects associated with Confocal Laser Scanning Microscopy, Submitted